UNIVERSITÉ DU LUXEMBOURG

PhD-FSTM-2025-055
The Faculty of Science, Technology and Medicine

# DISSERTATION

Defence held on 12 May 2025 in Luxembourg

to obtain the degree of

## DOCTEUR DE L'UNIVERSITÉ DU LUXEMBOURG

## EN PHYSIQUE

by

**Muralidhar Nalabothula**
Born on 20 March 1998 in K Perumallapuram, Andhra Pradesh, (India)

# Symmetries of Excitons: Implications for Exciton-Phonon Coupling and Optical Spectroscopy

## Dissertation defence committee

Prof. Dr. Ludger WIRTZ, dissertation supervisor
*Université du Luxembourg*

Prof. Dr. Michael ROHLFING
*University of Münster*

Prof. Dr. Matthieu VERSTRAETE
*Utrecht University*

Prof. Dr. Mael GUENNOU, Chair
*Université du Luxembourg*

Prof. Dr. Xavier GONZE, Vice Chair
*Université catholique de Louvain*

## Affidavit

I hereby confirm that the Ph.D. thesis entitled “Symmetries of Excitons: Implications for Exciton-Phonon Coupling and Optical Spectroscopy” has been written independently and without any other sources than cited.

I also acknowledge the use of ChatGPT and other AI tools, which were strictly limited to improving the language of this thesis.

Luxembourg, _____ _____

Muralidhar Nalabothula

# List of Publications

### Journal Articles

1. **Nalabothula, M.**, Wirtz, L., and Reichardt, S. (2025). Origin of Interlayer Exciton–Phonon Coupling in 2D Heterostructures. Nano Lett. 2025, 25, 15, 6160–6167.

2. Mella, J.D.*, **Nalabothula, M.***, Muñoz, F. et al. Prediction of BiS2-type pnictogen dichalcogenide monolayers for optoelectronics. npj 2D Mater Appl 8, 4 (2024).

3. Wang, H.-C., Huran, A. W., Marques, M. A. L., **Nalabothula, M.**, Wirtz, L., Romestan, Z., Romero, A. H. (2023). Two-Dimensional Noble Metal Chalcogenides in the Frustrated Snub-Square Lattice. J. Phys. Chem. Lett., 14(44), 9969–9977 .

4. P. Milev , B. Mellado-Pinto, **Nalabothula, M.** , A. Esquembre-Kučukalić , F. Alvarruiz , E. Ramos , L. Wirtz , J. E. Roman2, and D. Sangalli, Performances in solving the Bethe-Salpeter equation with the Yambo code, arXiv:2504.10096

5. Paleari, F., Molina-Sánchez, A., **Nalabothula, M.**., Reho, R., Bonacci, M., Castelo, J., ...Pereira Coutada Miranda, H. (2025). Yambopy. Zenodo. doi: 10.5281/zenodo.15012963

6. **Nalabothula, M.**, Davide Sangalli, Fulvio Paleari, Sven Reichardt, and Ludger Wirtz. Selection rules for exciton-phonon coupling in crystals. 2025. In preparation.

7. **Nalabothula, M.**, Davide Sangalli, Fulvio Paleari, Sven Reichardt, and Ludger Wirtz. Symmetries of excitons. 2025. In preparation.

* corresponds to equal contribution.

**Developed tools**

1. **LetzElPhC**: A highly parallelizable C code for computing electron-phonon matrix elements with full crystal symmetries https://github.com/yambo-code/LetzElPhC
2. **Ydiago**: A BSE diagonalization library for the Yambo code https://github.com/yambo-code/Ydiago
3. **PhdScripts**: Python scripts for computing exciton representations, exciton-phonon matrix elements with full crystal symmetries, resonant Raman intensities, and phonon-assisted luminescence. https://github.com/muralidhar-nalabothula/PhdScripts

All these tools were released under the permissive MIT License.

*Dedicated to my family, teachers and friends*

# Acknowledgments

I would like to express my deepest gratitude to my *“Doktorvater"*, Prof. Ludger Wirtz, for his unwavering support throughout my entire time here in Luxembourg. His invaluable insights, highest scientific standards, kindness, joviality, and empathy have profoundly shaped my academic journey. He has always fostered strong scientific criticism in the group and allowed me the academic freedom to explore any direction I wished. This thesis simply does not exist without the freedom that he has given me. I will always be indebted to him for what he has done for me. Once again, thank you Ludger, from the bottom of my heart.

I am also immensely grateful to Dr. Sven Reichardt, who was my very first friend in Luxembourg and later became my mentor. Sven has guided me on an excellent path, patiently taught me numerous things, and significantly influenced how I think, write, and critique. He is one of the most incredibly talented scientists that I have ever met. I sincerely hope that he returns to academia again and that his work gets much more attention than it receives now.

I extend my heartfelt thanks to my office mates, Henry and Aseem. It was a great pleasure to share an office with them. Aseem and I have had numerous discussions throughout my entire PhD, and I would love to collaborate with him in the future. I appreciate Henry’s support as we sailed in similar boats while striving to complete our Ph.D.s, which provided mutual moral support, especially during the final stages of Ph.D.

I am also grateful to Daniel, Max, Sahar, Amir, Thomas Galvani, Sandeep, Aldo, Tomasz, Fulvio, and Davide for their numerous scientific and non-scientific discussions. I also thank Adamantia for her administrative support throughout my PhD.

Special thanks to Prof. Xavier Gonze and Prof. Mael Guennou for serving on my CET committee. I am also thankful to Prof. Michael Rohlfing and Prof. Matthieu Verstraete for kindly agreeing to serve as the external examiners for my Ph.D. defense.

Finally, my deepest gratitude goes to my family and friends, whose unwavering support throughout this journey is beyond words. I am also immensely grateful to all my teachers throughout my life; without them, I would not have reached this stage.

# Abstract

Excitons, bound electron-hole pairs, play a crucial role in governing light-matter interactions in two-dimensional materials and wide-bandgap insulators such as hexagonal boron nitride. To obtain the energies and eigenstates of excitons, the state-of-the-art method is to solve the Bethe-Salpeter equation (BSE). Over the past two decades, many new approaches have been developed to compute exciton dynamics, including their coupling with phonons. These methods have been successful in determining properties such as exciton lifetimes and in understanding the optical spectra associated with them. Despite this progress, the symmetries of excitons and the selection rules associated with them have been largely overlooked.

In this thesis, we demonstrate how excitonic states transform under the action of crystal symmetry operations. In particular, we present a robust method for computing the representations of excitonic states. We apply this framework to analyze the selection rules governing exciton-photon and exciton-phonon interactions, which manifest themselves in spectroscopic techniques such as resonant Raman spectroscopy, absorption, and phonon-assisted luminescence across a wide range of materials.

Furthermore, we explore a particularly intriguing phenomenon in two-dimensional heterostructures: interlayer exciton-phonon coupling. This phenomenon arises from the interaction between excitons and phonons across adjacent layers. Although this phenomenon has been experimentally observed in various heterostructures of layered materials, its microscopic origin and underlying selection rules have remained elusive. Using the $WSe_2$@hBN heterostructure as an example, we investigate the origin of interlayer exciton-phonon coupling and its signatures in resonant Raman scattering through first-principles calculations. With the methods developed in this thesis, we elucidate how crystal symmetries play a cen-

tral role in governing interlayer exciton-phonon scattering processes, which are responsible for the anomalous resonant Raman intensities of the in-plane and out-of-plane $h$BN phonon modes. Moreover, we address the long-standing question regarding the underlying mechanism of this coupling. In particular, we find that the deformation potential induced by the $h$BN phonon interacts with the hybridized hole density of $WSe_2$ excitons near the $h$BN interface, leading to interlayer exciton-phonon coupling.

Finally, we present three computational tools that enhance state-of-the-art exciton-phonon calculations: (i) `LetzElPhC`, (ii) `Ydiago`, and (iii) `PhdScripts`.

`LetzElPhC` is a code for the calculation of electron-phonon and exciton-phonon coupling matrix elements. The code utilizes full crystal symmetries, which now makes it possible to perform exciton-phonon calculations using symmetries, drastically decreasing the computation time for these calculations. It resolves the long-standing phase issues that arise when expanding the electron-phonon coupling matrix elements from the irreducible Brillouin zone to the full Brillouin zone, which stem from the incompatibility between the electron-phonon matrix elements and the excitonic wavefunctions. The code also computes the electronic representation matrices as a byproduct, which enable us to compute the representations of the excitonic states.

`Ydiago` is a diagonalization library for the YAMBO code, which significantly accelerates the diagonalization of full or partial BSE matrices, achieving a tenfold improvement in both speed and memory efficiency compared to existing implementations in the Yambo code.

`PhdScripts` are a set of Python scripts that allow us to compute the irreducible representation labels for the excitonic states, exciton-phonon matrix elements with full crystal symmetries, as well as resonant Raman intensities and phonon-assisted luminescence intensities. Due to the use of symmetries, these scripts enable a more efficient computation of exciton-phonon properties compared to existing implementations.

# Contents

# List of Abbreviations

**BSE** ..... Bethe-Salpeter Equation

**DFT** ..... Density Functional Theory

**TDA** ..... Tamm-Dancoff Approximation

**GGA** ..... Generalized Gradient Approximation

**LDA** ..... Local Density Approximation

**FFT** ..... Fast Fourier Transform

**BZ** ..... Brillouin Zone

**PL** ..... Photoluminescence

**CL** ..... Cathodoluminescence

**DFPT** ..... Density Functional Perturbation Theory

**HPC** ..... High Performance Computing

**IBZ** ..... Irreducible Brillouin Zone

**MBPT** ..... Many-Body Perturbation Theory

**RPA** ..... Random Phase Approximation

**QE** ..... Quantum Espresso

**TMDC** ..... Transition Metal Dichalcogenides

**hBN** ..... Hexagonal Boron Nitride

**SOC** ..... Spin-Orbit Coupling

# Chapter 1

# Introduction

Symmetry is a central concept in physics, offering both a profound theoretical framework and practical tools for understanding complex systems. In essence, symmetry refers to the invariance of a system under specific transformations, such as rotations, translations, or reflections. These symmetries have far-reaching consequences in modern physics, often leading to conservation laws, such as the conservation of momentum and angular momentum [43]. Symmetries also play a crucial role in understanding many fundamental concepts, including the spin of elementary particles [118], Bloch's theorem [4], and more.

A direct consequence of these underlying symmetries is the existence of selection rules that govern the allowed transitions between quantum states [119]. For example, consider the hydrogen atom, which exhibits both full rotational and inversion symmetry. The solutions to the Schrödinger equation for the hydrogen atom are the atomic orbitals $1s, 2s, 2p, 3s, \ldots$. Electrons in the hydrogen atom can be excited or de-excited by absorbing or emitting a photon with compatible energy. However, due to the symmetries of the system, not all transitions are allowed. For example, the inversion symmetry of the hydrogen atom forbids the transition from the $2s$ excited state to the $1s$ ground state via single-photon emission. On the other hand, the transition from $2p \to 1s$ is allowed by photon emission. This selection rule plays a crucial role in the recombination of electrons and hydrogen ions in hot gases [119]. The $2s \to 1s$ transition requires the emission of two photons [49], each with insufficient energy to excite a neighboring hydrogen atom, and thus contributes to recombination. In

contrast, the $2p \rightarrow 1s$ transition, which involves the emission of a single photon, can excite nearby hydrogen atoms, which hardly influences the overall recombination dynamics.

These selection rules are not limited to hydrogen-like systems, but can also be extended to more complex systems such as molecules and crystals [25]. Unlike the hydrogen atom, these systems often lack full rotational symmetry and may or may not possess an inversion symmetry. Additionally, the presence of multiple electrons introduces many-body effects that must be taken into consideration to accurately describe electronic states. As a result, understanding how light interacts with these systems requires a sophisticated framework that accounts for these complexities.

Today, understanding light–matter interactions in crystals and molecules is at the forefront of materials science research. Using these interactions, one can manipulate light emission and absorption at the nanoscale, leading to practical applications in quantum computing [36], light-emitting diodes [77], solar cells [47], nonlinear optics [6], etc. Recent advances in understanding light–matter interactions, particularly in two-dimensional materials, have further expanded the ability to control and tailor optical properties, paving the way for a new generation of optoelectronic devices [112]. Therefore, understanding light–matter interactions in these materials, especially in two-dimensional materials, is crucial and has gained significant interest over the past two decades.

The central entities involved in light-matter interactions in two-dimensional materials are "*excitons*", hydrogen-like bound states that form when an electron is excited from the valence band to the conduction band, leaving behind a positively charged hole [31], as illustrated in Fig. 1.1. In low-dimensional materials [112, 74], molecular systems, and wide-bandgap materials such as hexagonal boron nitride (hBN) [117, 84], excitons play a dominant role in determining optical properties due to reduced dielectric screening. Just as in hydrogen atoms, the symmetries of excitons dictate which states can be excited or de-excited through light absorption and emission. Therefore, a thorough understanding of excitonic symmetries is essential to accurately describe and engineer the optical response of materials where excitonic effects are significant.

An important aspect of excitons is their interaction with other quasiparticles, especially

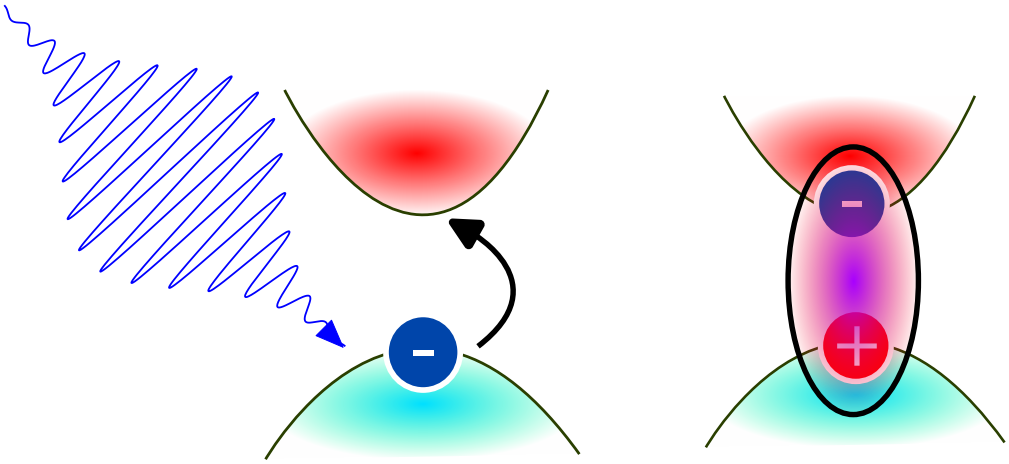

Figure 1.1: A cartoon depicting the formation of an electron-hole bound state, known as an exciton, upon illumination with light.

phonons. Exciton-phonon interactions play a critical role in optical scattering processes such as resonant Raman scattering [41, 95, 70], phonon-assisted luminescence [14, 85], and absorption. For example, in bulk $h$BN, one of the most widely used dielectric substrates or spacers for two-dimensional materials, strong exciton-phonon coupling gives rise to below-gap luminescence peaks [85]. Therefore, understanding excitonic dynamics and their interactions with other quasiparticles, such as phonons [85, 95], is vital for exploring the light-matter interactions in these materials.

Furthermore, exciton-phonon interactions significantly influence the lifetimes of excitonic states, which, in turn, determine the optical properties of materials [15]. More generally, controlling exciton lifetimes provides means to tailor optical emission properties. Since symmetry dictates the allowed scattering pathways in these processes, understanding the symmetries of excitons and their selection rules for scattering with other quasiparticles, such as phonons, is crucial for designing and manipulating the optical properties of materials.

In order to accurately describe and understand the properties of excitons and exciton-phonon interactions, it is essential to compute their energies and eigenstates. The standard approach for obtaining these quantities is to solve the Bethe-Salpeter equation (BSE) for the

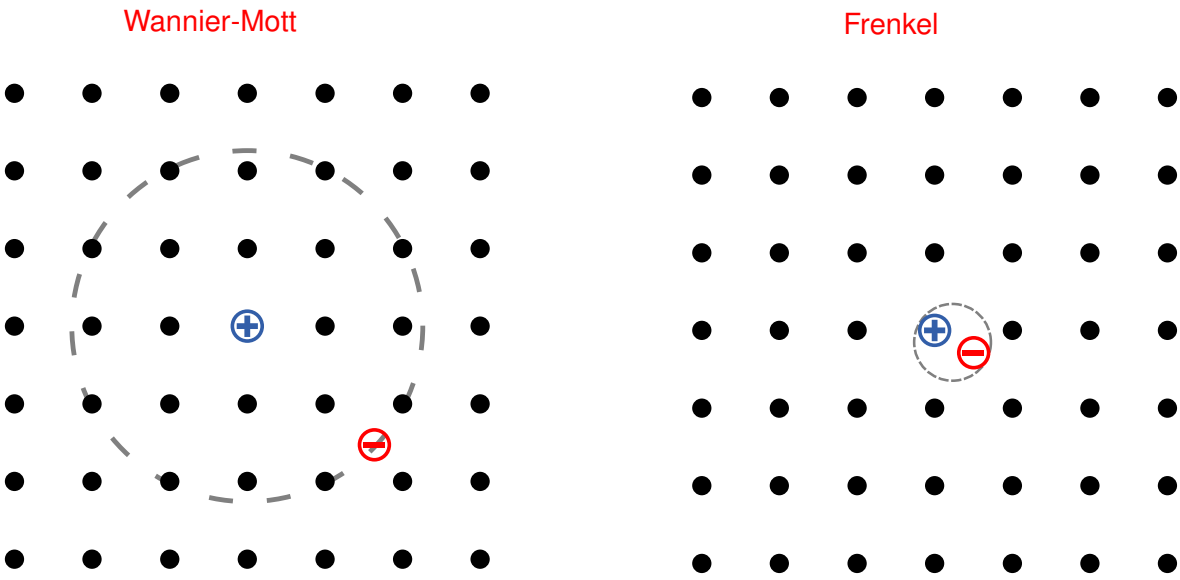


Figure 1.2: Types of excitons: (i) Wannier-Mott exciton, which extends over many unit cells. (ii) Frenkel exciton, where the electron and hole are localized within a unit cell. Adapted from Wikipedia

two-particle electron-hole correlation function [98, 67, 1, 83, 97]. This method is robust and applicable to a wide range of systems, including those that significantly deviate from simple models [84, 32, 123, 74]. Notably, physical observables obtained from BSE calculations have been shown to closely match experimental results across various materials, making it a powerful formalism for studying excitonic properties.

Although the solutions of the BSE describe excitonic states very well, extracting the symmetry information of excitons from them is not trivial. In some cases, hydrogen-like models are employed to describe excitons and understand their symmetry properties [30]. Based on their spatial extent, excitons are classified into two main types: Wannier-Mott excitons and Frenkel excitons as shown in Fig. 1.2. Wannier-Mott excitons are typically found in materials with high dielectric constants, such as conventional semiconductors (e.g., silicon and GaAs). These excitons are spatially extended, with radii much larger than the lattice constant, and can be effectively modeled as hydrogen-like systems within a quasi-continuous dielectric environment. In contrast, Frenkel excitons are highly localized and are typically found in molecular crystals and organic materials, where the exciton binding energy

is significantly larger, making them unsuitable for hydrogen-like modeling.

One key advantage of the hydrogenic model is its ability to offer insights into the symmetries of excitons. A fundamental question in this context is: which excitonic states couple to light, and why? The hydrogenic model provides a reasonable explanation in many cases. In bulk semiconductors, where excitons originate from transitions near the band gap and exhibit nearly circular symmetry, they are typically optically active (bright) [30].

Although the hydrogenic model provides valuable insight and works well for simple bulk semiconductors that host Wannier-type excitons, it is often too simplistic for systems whose excitonic character deviates from the Wannier type. Firstly, it is not applicable to Frenkel-type excitons. Moreover, recent studies have revealed that excitonic spectra can significantly deviate from hydrogen-like solutions, even in conventional semiconductors. For example, excitons in $h$BN exhibit notable deviations from the hydrogenic model [32]. Furthermore, the traditional classification of Wannier-Mott and Frenkel excitons becomes inadequate in materials with strong excitonic effects. For example, excitons near the optical band gap of hexagonal boron nitride ($h$BN) have been shown to fall outside both categories [123, 32].

Understanding the symmetries of excitonic states directly from the solutions of the Bethe-Salpeter equation remains a significant challenge. Currently, there are no rigorous *ab initio* methods for systematically analyzing excitonic symmetries. Although some attempts have been made to manually inspect excitonic wavefunctions in specific systems [85, 32, 84, 12], such as hexagonal boron nitride ($h$BN), these methods do not generalize easily to other materials.

In addition to these challenges, several fundamental questions remain unanswered: Can one assign symmetries to excitonic bands in a similar way to the symmetry assignments in electronic band structures? How do symmetries act on the excitonic Hamiltonian? Can symmetries be utilized to simplify the solution of the Bethe-Salpeter equation? Addressing these questions requires a systematic, symmetry-based approach—an effort that constitutes the central goal of this thesis.

## 1.1 Scope of this work

The primary goal of this thesis is to understand the symmetries of excitons. Over the past two decades, the Bethe-Salpeter equation (BSE) has become the gold standard for computing excitonic energies and eigenstates. Thanks to advances in computational power, it is now possible to perform BSE calculations for systems significantly larger than was feasible 20 years ago. In addition, many new methods have been developed in the last decade to study exciton dynamics, including techniques for computing and understanding exciton-phonon interactions and exciton dispersions. Although these developments have enabled an accurate reproduction of the experimental findings, the underlying symmetry principles were often overlooked.

As mentioned above, currently, one often relies on hydrogenic models or "manual" analysis of excitonic wavefunctions in real space, by fixing the electron or hole position to determine how excitonic states transform under symmetry operations. However, such analyses are nontrivial and can become cumbersome, even for relatively simple systems or when dealing with degenerate states. Therefore, a more robust, *ab initio* approach is needed. One of the main objectives of this thesis is to understand how excitons transform under the action of symmetries. We compute the representations of excitonic states, thereby allowing us to systematically understand their symmetry properties and selection rules. Furthermore, we introduce the concept of total crystal angular momentum for excitons and phonons, which is analogous to crystal momentum for translations and gives rise to the concept of "*chirality*" for excitons and phonons.

Another important aspect of symmetries is their potential to significantly simplify first-principles calculations. In density functional theory (DFT), nearly all well-established *ab initio* codes heavily employ symmetries to reduce computational cost. However, this is largely not the case for BSE calculations, where symmetries are mostly neglected. Even today, BSE is typically solved by explicitly breaking symmetries or by expanding wavefunctions over the full Brillouin zone. Moreover, the use of symmetries in exciton-phonon calculations has been largely avoided due to phase mismatch issues, which can lead to incorrect results

if not handled properly. As a result, exciton-phonon calculations are still performed without symmetries. Given that BSE calculations are computationally expensive, neglecting symmetries severely limits their applicability to larger systems. In this thesis, we discuss how symmetries can be leveraged to bypass the explicit computation of quantities such as exciton wavefunctions at symmetry-rotated $\mathbf{Q}$ points. Furthermore, we show how the full BSE Hamiltonian can be constructed by explicitly computing only a subset of the matrix elements, with the remainder obtained through symmetry operations. We also address phase issues that have plagued the exciton-phonon community over the past several years.

Of course, no theoretical method or implementation is complete without its application to real systems. In the second half of this thesis, we apply the developed formalism to understand the selection rules governing exciton-phonon interactions and their manifestations in optical spectroscopic tools, such as resonant Raman spectroscopy, absorption spectroscopy, and phonon-assisted luminescence. As will be demonstrated, symmetry principles and selection rules manifest beautifully in these experiments, thereby allowing us to understand the underlying exciton-phonon scattering pathways.

Finally, we conclude by showing how symmetries lead (although unintentionally) to the discovery of interlayer exciton-phonon coupling, where excitons in one layer interact with phonons in another. This fascinating phenomenon provides new insights into the coupling mechanisms between excitons and phonons across different layers in van der Waals heterostructures [55]. Although numerous experimental works have demonstrated this phenomenon in various heterostructures, the underlying mechanism has remained elusive. In this thesis, we use the $WSe_2$@hBN heterostructure to uncover the origin of this mechanism. In particular, we apply our developed methods to explain the symmetry selection rules in this heterostructure, which are responsible for the discovery of this effect: the out-of-plane phonon mode of hBN, which is Raman inactive in pristine hBN, couples with the first bright exciton of $WSe_2$, whereas the in-plane Raman-active modes do not. This leads to anomalous resonant Raman intensities for both modes. Furthermore, we systematically analyze the microscopic processes responsible for this phenomenon and unveil the microscopic mechanism for the first time.

## 1.2 Outline

This thesis is organized as follows.

In **Chapter 2**, we very briefly discuss the basic group theory and the Bethe-Salpeter equation, which is the state-of-the-art method for obtaining excitonic energies and eigenstates. This chapter primarily introduces the relevant equations and fundamental concepts that will be used in later parts of the thesis.

In **Chapter 3**, we introduce the group-theoretical treatment of excitons. Specifically, we examine how crystal symmetries act on excitonic states obtained from the Bethe-Salpeter equation. We first demonstrate that the well-known concept of exciton dispersion naturally arises as a consequence of the translational symmetry group. Furthermore, we show how excitonic states and energies at different exciton momenta can be determined by applying symmetry operations. In addition, we illustrate how symmetries can be exploited to reduce computational complexity in exciton calculations.

Next, we rigorously derive explicit expressions for the representation matrices of excitonic states, enabling the assignment of irreducible representation labels of the point group to these states. Finally, we apply this formalism to a simple material, lithium fluoride (LiF), to provide insights into the optical selection rules governing absorption spectroscopy.

In **Chapter 4**, we apply the techniques developed in **Chapter 3** to analyze selection rules in exciton-phonon coupling. A key result of this chapter is the introduction of *total crystal angular momentum*, which provides deeper insight into the selection rules governing these interactions. We then apply these selection rules to two widely used spectroscopic techniques: (1) *resonant Raman spectroscopy* and (2) *phonon-assisted luminescence*. Finally, we demonstrate how these selection rules manifest in experimental observations, providing a direct link between theory and experiment. In the end, we present explicit expressions for rotating electron-phonon and exciton-phonon matrix elements using crystal symmetry operations, ensuring efficient exciton-phonon workflows without any phase issues.

In **Chapter 5**, we extend the methods developed earlier to study the phenomenon of interlayer exciton-phonon interactions, where excitons in one layer couple with phonons in

a different layer. This chapter emphasizes the central role of symmetry and serves as another example of how symmetries can lead to new discoveries, even if unintentionally. We provide a detailed explanation of the microscopic mechanisms underlying this fascinating phenomenon, which has remained an open question for the past decade despite a substantial number of experimental measurements on various systems. In order to demonstrate the mechanism, we use the $WSe_2@h$BN heterostructure, and perform microscopic analysis of interlayer exciton-phonon coupling, which unveils the underlying mechanism for interlayer exciton-phonon coupling.

In the **Appendix**, we provide documentation for two newly developed codes:

- `LetzElPhC`, a program for computing electron-phonon coupling matrix elements with full symmetries.
- `YDiago`, a library designed to facilitate faster diagonalization in the Yambo code.

# Chapter 2

# Methods

In this chapter, we very briefly discuss the methods that will be used in the rest of this thesis.

In the first section, we introduce the basic definitions of group theory that will be used later in this thesis. In this work, we are concerned only with finite groups. This is by no means a complete review of group theory. A more detailed discussion can be found in numerous standard references, such as Refs. [29, 25, 107].

In the second section, we briefly review the current state-of-the-art methods used to compute and understand excitonic states. The purpose of this chapter is mainly to introduce definitions and define some expressions that will be used later in the thesis. The section on excitons is adapted mainly from Ref. [93]. A more detailed description can be found in many standard references [93, 98, 53, 1, 83, 67].

## 2.1 Group Theory

A *group* $G$ is a set of elements with a binary operation $\circ$ (also referred to as the group multiplication) that satisfies four criteria:

- **Closure:** For all elements $a, b \in G$, $a \circ b \in G$.
- **Associativity:** For all elements $a, b, c \in G$, $(a \circ b) \circ c = a \circ (b \circ c)$.

- **Identity:** There exists an identity element $e \in G$ such that for every $a \in G$: $a \circ e = e \circ a = a$
- **Inverse:** For each element $a \in G$, there exists an element $b \in G$ known as inverse of $a$ which is denoted by $a^{-1}$ such that: $a \circ b = b \circ a = e$

A group is said to be an *Abelian group* if its group multiplication is commutative, i.e., for all $a, b \in G$:

$$a \circ b = b \circ a.$$

**Cardinal number:** The number of elements in a set (if finite) is referred to as the cardinal number of a set.

**Order of an Element in a Group:** Suppose $g$ be an element of the group $G$, then the smallest positive integer $n$ for which $g^n = e$, is called the order of $g$ in $G$.

An important theorem in group theory to mention here is the *Rearrangement Theorem* (for proof see Ref. [25]). Consider an element $g \in G$ and let $G \equiv \{g_1, g_2, \dots\}$. The set obtained by multiplying $g$ with each element of $G$ regenerates $G$, i.e.,

$$\{g \circ g_1, g \circ g_2, \dots\} \equiv \{g_1 \circ g, g_2 \circ g, \dots\} \equiv G.$$

This implies that every element in $G$ is obtained only once when multiplying the entire group with $g$.

### 2.1.1 Subgroups

A *subgroup* $H$ of a group $G$ is a subset of $G$ that itself forms a group under the same operation $\circ$. The subgroup $H$ must contain the identity element of $G$ to fulfill the necessary group criteria. For the set of integers ($\mathbb{Z}$), which form a group under addition, the set of even integers forms a subgroup of $\mathbb{Z}$.

### 2.1.2 Cosets

Given a subgroup $H$ of a group $G$, and an element $g \in G$, we can define the left coset of $H$ in $G$ as:

$$gH = \{g \circ h \mid h \in H\}$$

Similarly, the right coset of $H$ in G is defined as:

$$Hg = \{h \circ g \mid h \in H\}$$

It is important to highlight that the cosets do not necessarily form a subgroup of $G$.

If $g$ also belongs to $H$, then the coset (left or right) is the same as $H$ (due to the rearrangement theorem). It can also be shown that two cosets are either the same or do not contain any elements in common (disjoint) [25, 107]. This implies that cosets can be used to partition a group into disjoint sets, i.e.,

$$G \equiv \bigcup_{i=1}^{n} g_i H \equiv \bigcup_{i=1}^{n} H g_i, \tag{2.1}$$

where $n$ is known as the "*index" of the subgroup $H$ in $G$*, which represents the number of cosets, and $g_i$ are known as the "*coset representatives*".

Moreover, the cardinal numbers of cosets are the same (due to the rearrangement theorem), which is equal to the cardinal number of the subgroup $H$. This implies that the cardinal number $n_H$ of a subgroup $H$ divides the cardinal number $n_G$ of the group $G$. The number $\frac{n_G}{n_H}$ is the same as the index of the subgroup $n$.

### 2.1.3 Conjugacy Classes

An element $g \in G$ is said to be conjugate to $a \in G$ if:

$$g = X \circ a \circ X^{-1} \text{ for } X \in G$$

The *conjugacy class* of an element $g \in G$ consists of all elements in $G$ that are conjugate to $g$, i.e.,

$$C(a) = \{g \circ a \circ g^{-1} \mid g \in G\}.$$

Conjugacy classes give rise to the concept of an important class of subgroups called *"normal"*, *"invariant"*, or *"self-conjugate"*.

A subgroup $H$ of $G$ is said to be normal if for any $g \in G$ and $a \in H$:

$$g \circ a \circ g^{-1} \in H$$

An important point to note is that for a normal subgroup, the left and right cosets are the same.

### 2.1.4 Factor group

The normal subgroups lead to the concept of the *factor group* (or quotient group), which is denoted as $G/H$. The set of cosets of a normal subgroup $H$ in $G$ forms a group known as the factor group of $G$ with $H$:

$$G/H = \{g_i H \mid g_i \in G\}.$$

The group multiplication for the factor group is defined as the multiplication of elements of two cosets, which gives rise to another coset. Factor groups are particularly important when studying the representation of space groups, which will be discussed later in this thesis.

### 2.1.5 Group Representations

#### Group Homomorphism

A *group homomorphism* is a function that maps one group to another, i.e., $\phi : G \to H$, while preserving the group operation. That is, for all elements $a, b \in G$,

$$\phi(a \circ b) = \phi(a) \circ \phi(b).$$

### Group Isomorphism

A *group isomorphism* is a group homomorphism that is bijective. A group isomorphism preserves the algebraic structure.

An *automorphism* is an isomorphism from a group to itself i.e $\phi : G \to G$.

### Group Representation

A *representation* or (linear representation) of a group $G$ is a group homomorphism from $G$ to the group of automorphisms $GL(V)$ of a vector space $V$ (an automorphism of a vector space $V$ is a linear operator that is a bijective map from $V$ onto itself), i.e., $\rho : G \to GL(V)$.

If we also consider automorphisms that respect group multiplication up to a constant factor $c(g_1, g_2)$, i.e.,

$$\rho(g_1 \circ g_2) = c(g_1, g_2)\, \rho(g_1) \circ \rho(g_2),$$

then the representation is said to be a *projective* representation of $G$.

### Matrix representation

Every $n$-dimensional vector space over a field $\mathbb{F}$ ($\mathbb{F}$ is $\mathbb{R}$ or $\mathbb{C}$) is isomorphic to $\mathbb{F}^n$ (See Appendix II of Ref. [107] which shows this for a complex field). The linear operations can be chosen to be matrices acting on them. If the group of automorphisms is chosen to be a group of $n \times n$ invertible matrices that act on a complex vector space $\mathbb{C}^n$, then the representation is called a matrix representation. Often, by default, a representation refers to a matrix representation of a group. We use $D$ instead of $\rho$ for matrix representations. For example, consider a cyclic group $C_3 = \{E, a, a^2\}$ with $a^3 = E$. The one dimentional matrix represantion of $C_3$ is given by

$$D(E) = 1 \tag{2.2}$$

$$D(a) = e^{i\frac{2\pi i}{3}} \tag{2.3}$$

$$D(a^2) = e^{\frac{4\pi i}{3}} \tag{2.4}$$

Similarly, a possible $2 \times 2$ matrix representation of the $C_3$ group is given by:

$$D(E) = \begin{pmatrix} 1 & 0 \\ 0 & 1 \end{pmatrix} \tag{2.5}$$

$$D(a) = \begin{pmatrix} -1/2 & -\sqrt{3}/2 \\ \sqrt{3}/2 & -1/2 \end{pmatrix} \tag{2.6}$$

$$D(a^2) = \begin{pmatrix} -1/2 & \sqrt{3}/2 \\ -\sqrt{3}/2 & -1/2 \end{pmatrix} \tag{2.7}$$

**Unitary representation:**

A *unitary representation* is a representation in which the linear operators are unitary, i.e., $UU^\dagger = I$, where $U^\dagger$ is the adjoint of $U$. We almost always work with unitary representations of a group.

If the linear operators are matrices and the basis of the vector space are orthogonal, then $U^\dagger$ is the Hermitian adjoint (conjugate transpose) of $U$, and $I$ is the identity matrix.

Unitary representations are important in quantum mechanics as they preserve the inner product. Since symmetries preserve probabilities or inner products on Hilbert spaces, symmetries are represented by unitary or anti-unitary operators (for time-reversal symmetry) acting on the Hilbert space. This is also known as the Wigner's theorem, which is fundamental and serves as one of the founding theorem of quantum mechanics [120].

**Invariant subspaces**

A subset $W$ of a vector space $V$ that forms a vector space by itself is known as a *subspace*. The set consisting of only the zero vector or the entire space $V$ is known as a trivial subspace of $V$.

If a subspace $W$ is closed under the action of a linear operator $T : V \to V$ (i.e., the action of $T$ on an element of $W$ gives an element in $W$), then it is known as an invariant subspace of $T$.

A subspace $W$ is said to be $G$-invariant if $\forall g \in G$ and $\forall w \in W$, $\rho(g)w \in W$.

### Equivalent Representations

Two representations $\rho_1 : G \to GL(V_1)$ and $\rho_2 : G \to GL(V_2)$ are said to be equivalent if there is an isomorphism $A : V_1 \to V_2$ such that

$$\rho_2(g)A = A\rho_1(g) \quad \forall g \in G.$$

In matrix language, if we consider two matrix representations $\{D_1(g_1), D_1(g_2), \dots\}$ and $\{D_2(g_1), D_2(g_2), \dots\}$, they are said to be equivalent if there is a square matrix $A$ such that

$$A^{-1}D_2(g)A = D_1(g) \quad \forall g \in G.$$

An important point to highlight is that for a representation $D$ of a finite group, there is always a unitary representation that is equivalent to $D$ (known as the Weyl unitary trick). This implies that it is enough to work only with unitary representations.

### Irreducible Representation

A representation $\rho : G \to GL(V)$ is said to be *irreducible* if there is no nontrivial subspace of $V$ that is $G$-invariant. For example, consider the group of distance-preserving transformations of Euclidean space, denoted as $SO(3)$. The set of $3 \times 3$ orthogonal matrices acting on the vector space $\mathbb{R}^3$ forms an irreducible representation of $SO(3)$.

If a representation is not an irreducible representation, then it is said to be a *"reducible"* representation. A reducible representation can be decomposed into a direct sum of irreducible representations. This implies one can work with individual smaller irreducible representations instead of larger representation.

In matrix language, a representation is said to be reducible if there is an equivalent representation that can bring all the group elements to the same block-diagonal form. If not, then it is said to be irreducible. In other words, a reducible representation is of the form (or

can be brought to this form by the same similarity transformation applied to all the elements of the group)

$$D(g) = \begin{pmatrix} D_1(g) & 0 \\ 0 & D_2(g) \end{pmatrix} \quad \forall g \in G.$$

Any reducible representation can be decomposed into a direct sum of irreducible representations (Maschke's Theorem).

### 2.1.6 Characters of Representations

The *character* $\chi$ of a representation $\rho$ is a map $\chi : G \to \mathbb{C}$ which is defined as

$$\chi(g) = \mathsf{Tr}(\rho(g)) \; \forall g \in G,$$

where Tr denotes the trace of the linear operator. Since the trace is invariant under similarity transformations, all the elements in a conjugacy class have the same trace, which implies that the trace is a function of the conjugacy classes of the group. Moreover, the characters for the equivalent representations are the same. This allows us to compactly tabulate the characters of irreducible representations for the conjugacy classes in each group. These tables are referred to as *character tables*. For example, the character table for the cyclic group $C_3$, which contains three elements and three classes, is given below:

| $C_3$ | $E$ | $a$ | $a^2$ |
|---|---|---|---|
| $A$ | 1 | 1 | 1 |
| $E$ | 1 | $\omega$ | $\omega^2$ |
| $E^*$ | 1 | $\omega^2$ | $\omega$ |

where $\omega = e^{2\pi i/3}$, and $A$, $E$, and $E^*$ are the labels of irreducible representations of the group $C_3$.

### 2.1.7 Orthogonality relations

One of the most important applications of group theory in quantum mechanics is the derivation of selection rules for matrix elements of operators. Before discussing these selection rules, we introduce two fundamental lemmas known as *Schur's lemmas*, which are central to the representation theory of finite groups. Using Schur's lemmas, one can prove the *Great Orthogonality Theorem* [21], which forms the foundation for applying group-theoretical techniques to quantum mechanical problems.

From here on, the word representation implies matrix representation.

#### Schur's lemma 1

Let $D_1 : G \to \mathrm{GL}(V)$ and $D_2 : G \to \mathrm{GL}(W)$ be two irreducible representations of a finite group $G$. Suppose that there exists a matrix $X$ such that

$$XD_1(g) = D_2(g)X \quad \forall g \in G.$$

Then either $X = 0$, or $X$ is an invertible square matrix (which implies $W$ and $V$ must be isomorphic). In the latter case, the representations $D_1$ and $D_2$ are equivalent [9].

#### Schur's lemma 2

Let $D : G \to \mathrm{GL}(V)$ be an irreducible representation of a finite group $G$ on a vector space $V$. Suppose that there exists a matrix $X$ such that

$$XD(g) = D(g)X \quad \forall g \in G.$$

Then $X = \lambda I_{n\times n}$ for some scalar $\lambda$, where $I_{n\times n}$ is the identity matrix. [9].

An important consequence of the second lemma is that all irreducible representations of finite abelian groups are one-dimensional. This is because every element of an abelian group commutes with every other element of the group, which implies that all representation matrices commute with each other. By Schur's lemma, this means that every element of the

group can be represented by a scalar.

### The great orthogonality theorem

With the two Schur lemmas, one can derive a very powerful result known as the "great orthogonality theorem" (see Ref. [25] for proof). Let $D_1 : G \to \mathrm{GL}(V)$ and $D_2 : G \to \mathrm{GL}(W)$ be two irreducible unitary representations of a finite group $G$. If they are not equivalent, then

$$\sum_{g \in G} D_1(g)_{ij}\, D_2^{\dagger}(g)_{kl} = 0. \tag{2.8}$$

For each representation,

$$\sum_{g \in G} D_1(g)_{ij}\, D_1^{\dagger}(g)_{kl} = \frac{|G|}{d}\, \delta_{il}\, \delta_{jk}, \tag{2.9}$$

where $|G|$ is the cardinal number of the group, and $d$ is the dimension of the matrices in the $D_1$ representation.

### Orthogonality theorem for characters

From Eqs. (2.8) and (2.9), we can show that

$$\sum_{g \in G} \chi_1(g)\, \chi_2^*(g) = \sum_c n_c\, \chi_1(c)\, \chi_2^*(c) = |G|\, \delta_{12}, \tag{2.10}$$

where the sum over $c$ runs over conjugacy classes, each containing $n_c$ elements, and $\chi_1(c)$, $\chi_2(c)$ are the characters corresponding to the class $c$.

Furthermore, we can rewrite Eq. (2.10) as

$$\sum_c \sqrt{\frac{n_c}{|G|}}\, \chi_1(c) \sqrt{\frac{n_c}{|G|}}\, \chi_2^*(c) = \delta_{12}. \tag{2.11}$$

If we interpret the set of characters of each irreducible representation as a vector of dimension $N_c$, then the number of linearly independent such vectors is $N_c$. This implies that there can be at most $N_c$ sets of characters satisfying Eq. (2.11), and hence the group has at

most $N_c$ irreducible representations.

Another orthogonality relation is given by

$$\sum_{\alpha=1}^{n} \left(\chi^{(\alpha)}(i)\right)^* \chi^{(\alpha)}(j) = \frac{|G|}{n_i}\,\delta_{ij}, \tag{2.12}$$

where the sum runs over irreducible representations. Similar to Eq. (2.10), we can interpret Eq. (2.12) as the dot product of two vectors of dimension equal to the number of irreducible representations. This now implies that the number of conjugacy classes must be at most equal to the number of irreducible representations.

Therefore, the number of conjugacy classes is equal to the number of irreducible representations. More details on orthogonality relations can be found in Ref. [25].

### 2.1.8 Decomposition of Reducible Representations

In this section we show how one can decompose a given representation into a direct sum of irreducible representations using the orthogonality relations discussed previously.

Let $D$ be a representation of a finite group $G$ on $V$. Then $D$ can be decomposed into irreducible representations $D^i$ as

$$D(g) = \bigoplus m_i D^i(g)\ \forall g \in G, \tag{2.13}$$

where $m_i$ are the multiplicities of the irreducible representations, which are given by

$$m_i = \frac{1}{|G|} \sum_c n_c\, \chi_{(D)}(c) \left(\chi^i(c)\right)^*, \tag{2.14}$$

where $\chi_{(D)}(c)$ is the character of the representation $D$ for class $c$, $\chi^i(c)$ is the character of the irreducible representation $D^i$, and $n_c$ is the number of elements in class $c$.

### 2.1.9 Application to Quantum mechanics

We now briefly discuss the applications of group theory to quantum-mechanical problems.

Consider the following eigenvalue problem:

$$H\Psi = E\Psi,$$

where $H$ is the Hamiltonian and $\Psi$ is a wavefunction. The set of eigenvectors of $H$ spans the Hilbert space of the physical system. Moreover, the transformation of $H$ by an operator $R$ is given by

$$H' = RHR^{-1}.$$

If $H$ is invariant under the action of $R$, i.e., $H' = H$, then we say that $R$ is a symmetry of the system. The set of all such symmetry operations $R$ forms a representation of a group $G$ acting on the Hilbert space.

Since $R$ and $H$ commute, we have

$$HR\Psi = RH\Psi = ER\Psi.$$

This shows that $R\Psi$ is also an eigenvector of $H$ with the same eigenvalue as $\Psi$. This implies that the presence of symmetries gives rise to the concept of degeneracies in quantum systems.

Suppose that we collect all the eigenvectors corresponding to the eigenvalue $E$; then this vector space forms a $G$-invariant subspace of the Hilbert space, with dimension equal to the degeneracy of the eigenvalue $E$. This implies that the representation $R$ can be decomposed into subrepresentations:

$$R \equiv \bigoplus_i R^i,$$

where each $R^i$ acts on a $G$-invariant subspace $W$ containing the eigenvectors of $H$ with eigenvalue $E$. If $R^i$ is irreducible, then the corresponding eigenstates can be labeled by the irreducible representation. If $R^i$ is not irreducible, it can be further decomposed into a direct sum of irreducible representations using the procedures briefly described above.

#### Selection Rules

Finally we conclude the section on Group theory by discussing the selection rules for matrix elements.

Consider the following matrix element:

$$\langle \Psi_n | \hat{O} | \Psi_m \rangle ,$$

where $\Psi_{n/m}$ are eigenstates of the Hamiltonian $H$, and $\hat{O}$ is an operator which may not possess the same symmetries as $H$.

Clearly, the matrix element is a linear operator (more precisely, a functional) that takes a vector from a vector space $V$, where each element is composed of a set of three vectors $\{|\Psi_m\rangle, \hat{O}, \langle\Psi_n|\}$, and maps them to a scalar, which must be invariant under the action of any symmetry operation. This implies that the representation of the group $G$ on $V$ must be a trivial representation (or fully symmetric). Since $V$ is a direct product of three vector spaces $\{|\Psi_m\rangle\}, \{\hat{O}\}, \{\langle\Psi_n|\}$, it follows that the direct product representation of $G$ on these three vectors must either be trivial or contain a trivial representation for the matrix element to be finite. In other words,

$$D_A \subset D_n \otimes D_O \otimes D_m,$$

where $D_A$ is the trivial representation of $G$ on $V$, and $D_n$, $D_O$, and $D_m$ are the representations of $G$ on the vector spaces $\{|\Psi_m\rangle\}$, $\{\hat{O}\}$, and $\{\langle\Psi_n|\}$, respectively.

## 2.2 Excitons

Before discussing excitons, we first provide a brief overview of density functional theory (DFT), and the single-particle Green's function along with common approximations. These serve as the foundation for the many-body formalism and play a crucial role in the subsequent discussion of the two-particle Green's function.

### 2.2.1 Density functional theory (DFT)

We start by writing the fully interacting time-independent many-body Hamiltonian of a crystal without relativistic effects and ignoring the spin of the electron, which is given by [66]

$$\hat{H} = \hat{T}_e + \hat{T}_I + \hat{V}_{ee} + \hat{V}_{II} + \hat{V}_{eI}, \tag{2.15}$$

where $\hat{T}_e = -\sum_i \frac{\hbar^2}{2m_e}\nabla_i^2$ is the kinetic energy operator for electrons, with $m_e$ being the mass of an electron; $\hat{T}_I = -\sum_\alpha \frac{\hbar^2}{2M_\alpha}\nabla_\alpha^2$ is the kinetic energy operator for nuclei, with $M_\alpha$ being the mass of the $\alpha$-th nucleus; $\hat{V}_{ee} = \frac{1}{2}\sum_{i\neq j}\frac{e^2}{|\mathbf{r}_i - \mathbf{r}_j|}$ describes the repulsive Coulomb potential energy between electrons; $\hat{V}_{II} = \frac{1}{2}\sum_{\alpha\neq\beta}\frac{Z_\alpha Z_\beta e^2}{|\boldsymbol{\tau}_\alpha - \boldsymbol{\tau}_\beta|}$ accounts for the repulsive Coulomb potential between nuclei; $\hat{V}_{eI} = -\sum_{i,\alpha}\frac{Z_\alpha e^2}{|\mathbf{r}_i - \boldsymbol{\tau}_\alpha|}$ represents the attractive Coulomb potential between electrons and nuclei.

To simplify the problem given in Eq. (2.15), one of the first and most widely used approximations is the Born-Oppenheimer approximation [8]. Since nuclei are much heavier than electrons, their kinetic energy term, $\hat{T}_I$, is initially neglected. This allows the Hamiltonian to be decoupled into electronic and nuclear parts, and we can approximate the total wavefunction as

$$\Psi(\mathbf{r}_1, ...\mathbf{r}_m; \boldsymbol{\tau}_1, ...\boldsymbol{\tau}_n) \approx \psi_e(\mathbf{r}_1, ...\mathbf{r}_m; \boldsymbol{\tau}_1, ...\boldsymbol{\tau}_n)\chi(\boldsymbol{\tau}_1, ...\boldsymbol{\tau}_n), \tag{2.16}$$

where $\psi_e(\mathbf{r}_1, ...\mathbf{r}_m; \boldsymbol{\tau}_1, ...\boldsymbol{\tau}_n)$ is the electronic wavefunction, and $\chi(\boldsymbol{\tau}_1, ...\boldsymbol{\tau}_n)$ is the nuclear wavefunction.

The electronic Hamiltonian is solved for fixed nuclear coordinates, i.e.,

$$\hat{H}_e\psi_e(\mathbf{r}_1, ...\mathbf{r}_m; \boldsymbol{\tau}_1, ...\boldsymbol{\tau}_n) = E_e(\boldsymbol{\tau})\psi_e(\mathbf{r}_1, ...\mathbf{r}_m; \boldsymbol{\tau}_1, ...\boldsymbol{\tau}_n), \tag{2.17}$$

where $\hat{H}_e = \hat{T}_e + \hat{V}_{ee} + \hat{V}_{ne}$ is the electronic Hamiltonian. The nuclear Hamiltonian is then given by

$$\left(\hat{T}_n + \hat{V}_{nn} + E_e(\boldsymbol{\tau})\right)\chi(\boldsymbol{\tau}_1, ...\boldsymbol{\tau}_n) = E\chi(\boldsymbol{\tau}_1, ...\boldsymbol{\tau}_n). \tag{2.18}$$

Although the Born-Oppenheimer approximation greatly simplifies the problem, solving the full many-body Hamiltonian within this approximation still remains impossible. This made it necessary to seek alternative methods to tackle the many-body problem, which led to the development of a revolutionary method by Hohenberg, Kohn, and Sham known as density functional theory (DFT) [52, 56].

Today, DFT is the state-of-the-art method for computing and predicting the ground-state properties of materials. DFT reformulates the many-body problem in terms of an auxiliary non-interacting system that shares the same electron density as the fully interacting system described by Eq. (2.17). The electron density of the interacting system is given by

$$\rho(\mathbf{r}) = m \int d^3\mathbf{r}_2 \dots d^3\mathbf{r}_m |\Psi_i(\mathbf{r}, \mathbf{r}_2, \dots, \mathbf{r}_m)|^2. \tag{2.19}$$

By working with an auxiliary non-interacting system, DFT drastically reduces computational costs while still providing valuable physical insights.

DFT is founded on two theorems (referred to as the Hohenberg-Kohn theorems) [52], which are stated as follows:

1. The ground-state electron density $\rho(\mathbf{r})$ uniquely determines the external potential $V_{ext}(\mathbf{r})$ and, consequently, all ground-state properties. The external potential in this case corresponds to the electron-ion interaction term, $\hat{V}_{eI}$, in Eq. (2.15).

2. The total energy functional $E[\rho]$ satisfies the variational principle:

$$E_0 = \min_{\rho} E[\rho], \tag{2.20}$$

   where $E_0$ is the ground-state energy.

The total energy functional $E[\rho]$ is given by [52]:

$$E[\rho] = T_s[\rho] + E_H[\rho] + E_{xc}[\rho] + E_{ext}[\rho], \tag{2.21}$$

where $T_s[\rho]$ is the kinetic energy of a system of non-interacting electrons, $E_H[\rho]$ is the classical electrostatic (Hartree) energy, $E_{xc}[\rho]$ is the exchange-correlation energy, and $E_{ext}[\rho]$ is

the interaction with the external potential. These terms are explicitly given as follows:

The Hartree energy is given by

$$E_H[\rho] = \frac{1}{2}\int d\mathbf{r}d\mathbf{r}' \frac{\rho(\mathbf{r})\rho(\mathbf{r}')}{|\mathbf{r}-\mathbf{r}'|}. \tag{2.22}$$

The exchange-correlation energy is written as:

$$E_{xc}[\rho] = \int d\mathbf{r}\, \rho(\mathbf{r})\epsilon_{xc}(\rho(\mathbf{r})), \tag{2.23}$$

where $\epsilon_{xc}(\rho)$ is the exchange-correlation energy per electron.

and the external potential energy is written as

$$E_{ext}[\rho] = \int d\mathbf{r}\, \rho(\mathbf{r})V_{ext}(\mathbf{r}). \tag{2.24}$$

To construct $E[\rho]$, Kohn and Sham introduced an auxiliary system of non-interacting electrons whose density is expressed as

$$\rho(\mathbf{r}) = \sum_i |\phi_i(\mathbf{r})|^2, \tag{2.25}$$

where $\phi_i(\mathbf{r})$ are the single-particle states, also referred to as Kohn-Sham states (or basis).

Applying the minimization procedure with the constraint that the single-particle states $\phi_i(\mathbf{r})$ are normalized leads to an independent set of equations known as the Kohn-Sham equations, which are given by

$$\left[-\frac{\hbar^2}{2m}\nabla^2 + V_{ext}(\mathbf{r}) + V_H(\mathbf{r}) + V_{xc}(\mathbf{r})\right]\phi_i(\mathbf{r}) = \epsilon_i\phi_i(\mathbf{r}), \tag{2.26}$$

where $\epsilon_i$ are the Kohn-Sham eigenvalues, the Hartree potential is $V_H(\mathbf{r}) = \int d\mathbf{r}' \frac{\rho(\mathbf{r}')}{|\mathbf{r}-\mathbf{r}'|}$, the exchange-correlation potential is $V_{xc}(\mathbf{r}) = \frac{\delta E_{xc}[\rho]}{\delta\rho(\mathbf{r})}$, and the external potential is $V_{ext}(\mathbf{r}) = \frac{\delta E_{ext}[\rho]}{\delta\rho(\mathbf{r})} = V_{ion}(\mathbf{r})$. In practice, one solves Eq. (2.26) self-consistently within the Local Density Approximation [56] (LDA) or the Generalized Gradient Approximation [86] (GGA) for the exchange-correlation functional to obtain the ground-state density. A more detailed descrip-

tion can be found in Ref. [66].

Although Kohn-Sham DFT accurately describes ground state properties in most cases, it fails to adequately capture excited-state phenomena such as band gaps [88] and excitons [67]. Therefore, the Green function approach, which is discussed in the remainder of this chapter, is employed to address these limitations.

### 2.2.2 Single particle Green's function

The single-particle Green's function describes the probability that an electron propagates from the space-time position $(\mathbf{r}_1, t_1)$ to $(\mathbf{r}_2, t_2)$. It enables us to calculate the ground-state expectation values for any one-particle operators. The single-particle Green's function is defined as

$$G(2,1) = -i\langle 0|\hat{T}\{\hat{\psi}(2)\hat{\psi}^{\dagger}(1)\}|0\rangle, \tag{2.27}$$

where $\hat{T}$ is the time-ordering operator, the numbers represent the space-time coordinates (for example, $1 \rightarrow (\mathbf{r}_1, t_1)$), and the operator $\hat{\psi}(1)$ denotes the electron field operator in the Heisenberg picture, which is given by

$$\hat{\psi}^{(\dagger)}(\mathbf{r}, t) = e^{+i\hat{H}t}\hat{\psi}^{(\dagger)}(\mathbf{r})e^{-i\hat{H}t}. \tag{2.28}$$

where $\hat{H}$ is the electronic Hamiltonian for the equilibrium structure with $|0\rangle$ representing its ground state. The field operator $\hat{\psi}(\mathbf{r})$ can be expressed in terms of a complete set of single-particle states and is given as

$$\hat{\psi}(\mathbf{r}) \equiv \sum_n \phi_n(\mathbf{r})\hat{c}_n, \tag{2.29}$$

where the set $\{\phi_n(\mathbf{r})\}$ are the one-particle wave functions and the operator $\hat{c}_n$ is the fermionic annihilation operator of state $n$, which obeys the fermionic anti-commutation relations, i.e.,

$$\{\hat{c}_n, \hat{c}^{\dagger}_{n'}\} = \delta_{n,n'}, \quad \{\hat{c}_n, \hat{c}_{n'}\} = \{\hat{c}^{\dagger}_n, \hat{c}^{\dagger}_{n'}\} = 0. \tag{2.30}$$

Within time-dependent perturbation theory [101, 118], the electronic Hamiltonian $\hat{H}$ can be divided into two components:

$$\hat{H} = \hat{H}_0 + V(t), \tag{2.31}$$

where $|\emptyset\rangle$ is a non-degenerate ground state of $\hat{H}_0$, and $V(t)$ is treated as a perturbation. In many cases, a reasonable approximation for $\hat{H}_0$ is the Kohn-Sham DFT Hamiltonian, which is given by

$$\hat{H}_0 \equiv \hat{H}_{\mathsf{KS}}(\{\boldsymbol{\tau}_i^{(0)}\}) \equiv \int d^3r\, \hat{\psi}^\dagger(\mathbf{r}) \left( -\frac{\nabla^2}{2m} + V_{\mathsf{scf}}(\mathbf{r}; \{\boldsymbol{\tau}_i^{(0)}\}) \right) \hat{\psi}(\mathbf{r}), \tag{2.32}$$

where $V_{\mathsf{scf}}(\mathbf{r}; \{\boldsymbol{\tau}_i^{(0)}\})$ is the self-consistent potential, which is the sum of the external potential, Hartree potential, and exchange-correlation potential as given in Eq. (2.26) and $\boldsymbol{\tau}_i^{(0)}$ are equilibrium positions of the atoms.

In the interaction picture, the field operators are then defined as [101, 118]

$$\hat{\psi}_I^{(\dagger)}(1) = e^{+i\hat{H}_0 t_1} \hat{\psi}^{(\dagger)}(\mathbf{r}_1) e^{-i\hat{H}_0 t_1}. \tag{2.33}$$

The corresponding non-interacting Green's function is expressed as

$$G_0(2,1) = -i\langle\emptyset|\hat{T}\{\hat{\psi}_I(2)\hat{\psi}_I^\dagger(1)\}|\emptyset\rangle. \tag{2.34}$$

This allows us to write the Green's functions involving two Heisenberg picture field operators given in Eq. (2.27) as [101, 118]

$$\langle 0|T\{\hat{\psi}(2)\hat{\psi}^\dagger(1)\}|0\rangle = \frac{\langle\emptyset|\hat{T}\left\{\hat{\psi}_I(2)\hat{\psi}_I^\dagger(1)\exp\left(-i\int_{-\infty}^{\infty} dt\, \hat{H}_I(t)\right)\right\}|\emptyset\rangle}{\langle\emptyset|\hat{T}\left\{\exp\left(-i\int_{-\infty}^{\infty} dt\, \hat{H}_I(t)\right)\right\}|\emptyset\rangle}, \tag{2.35}$$

where the perturbative Hamiltonian in the interaction picture is given by

$$\hat{H}_I(t) = e^{+i\hat{H}_0 t} V(t) e^{-i\hat{H}_0 t}. \tag{2.36}$$

Substituting Eq. (2.29) into Eq. (2.34) (here $\phi_{\mathbf{k},n}(\mathbf{r})$ are the one-particle Kohn-Sham basis

functions), the non-interacting Green's function, which is diagonal is written as

$$G_0(2,1) = \sum_{\mathbf{k},n} \phi_{\mathbf{k},n}(\mathbf{r}_2)\phi^*_{\mathbf{k},n}(\mathbf{r}_1)(-i)\langle\emptyset|\hat{T}\{\hat{c}_{\mathbf{k},n,I}(t_2)\hat{c}^\dagger_{\mathbf{k},n,I}(t_1)\}|\emptyset\rangle, \tag{2.37}$$

where $\hat{c}_{\mathbf{k},n,I}$ are $\hat{c}_{\mathbf{k},n}$ operators in interacting picture.

The Fourier transform $G_0(2,1)$ can be defined as

$$G_0(2,1) = \sum_{\mathbf{k},n} \phi_{\mathbf{k},n}(\mathbf{r}_2)\phi^*_{\mathbf{k},n}(\mathbf{r}_1) \int \frac{d\omega}{2\pi} e^{-i\omega(t_2-t_1)}\tilde{G}_{0;\mathbf{k},n}(\omega). \tag{2.38}$$

where we employed time-translational invariance to reduce the two frequency coordinates to one. The Fourier-transform of the Green's function $\tilde{G}_{0;\mathbf{k},n}(\omega)$ is given by

$$\begin{aligned}\tilde{G}_{0;\mathbf{k},n}(\omega) &= (-i)\int_{-\infty}^{\infty} dt' \,\langle\emptyset|\hat{T}\{\hat{c}_{\mathbf{k},n,I}(t')\hat{c}^\dagger_{\mathbf{k},n,I}(0)\}e^{i\omega t'}|\emptyset\rangle \\ &= \frac{f_{\mathbf{k},n}}{\omega - i\eta - \epsilon_{\mathbf{k},n}} + \frac{1-f_{\mathbf{k},n}}{\omega + i\eta - \epsilon_{\mathbf{k},n}},\end{aligned} \tag{2.39}$$

where $f_{\mathbf{k},n}$ denotes the occupation of the state $|\mathbf{k},n\rangle$ in the KS ground state $|\emptyset\rangle$, and $\eta \to 0^+$.

On the other hand, the exact one-particle Green's function defined in Eq. (2.27) is, in general, off-diagonal in the KS basis, and is written as

$$G(2,1) = \sum_{\mathbf{k},m,n} \phi_{\mathbf{k},m}(\mathbf{r}_2)\phi^*_{\mathbf{k},n}(\mathbf{r}_1)(-i)\langle 0|\hat{T}\{\hat{c}_{\mathbf{k},m}(t_2)\hat{c}^\dagger_{\mathbf{k},n}(t_1)\}|0\rangle, \tag{2.40}$$

The Fourier transform of the exact Green's function is defined as

$$G(2,1) = \sum_{\mathbf{k},m,n} \phi_{\mathbf{k},m}(\mathbf{r}_2)\phi^*_{\mathbf{k},n}(\mathbf{r}_1) \int \frac{d\omega}{2\pi} e^{-i\omega(t_2-t_1)}\tilde{G}_{\mathbf{k},m,n}(\omega), \tag{2.41}$$

where

$$\tilde{G}_{\mathbf{k},m,n}(\omega) = \int_{-\infty}^{\infty} dt\, e^{i\omega t}(-i)\langle 0|\hat{T}\{\hat{c}_{\mathbf{k},m}(t)\hat{c}^\dagger_{\mathbf{k},n}(0)\}|0\rangle. \tag{2.42}$$

It should be noted that due to the translational invariance, Eq. (2.42) and (2.41), we only have one $\mathbf{k}$.

Finally, the interaction Hamiltonian $V(t)$ is given as

$$\begin{aligned} V(t) \equiv \hat{H} - \hat{H}_0 = \frac{1}{2} \int d^3\mathbf{r} \int d^3\mathbf{r}' \, \hat{\psi}^\dagger(\mathbf{r}) \hat{\psi}^\dagger(\mathbf{r}') \frac{e^2}{|\mathbf{r} - \mathbf{r}'|} \hat{\psi}(\mathbf{r}') \hat{\psi}(\mathbf{r}) \\ - \int d^3\mathbf{r} \, \hat{\psi}^\dagger(\mathbf{r}) \left( V_{\mathsf{xc}}(\rho_{\mathsf{KS}}, \mathbf{r}) + V_{\mathsf{H}}(\rho_{\mathsf{KS}}, \mathbf{r}) \right) \hat{\psi}(\mathbf{r}), \end{aligned} \tag{2.43}$$

where $\rho_{\mathsf{KS}}$ is the ground-state charge density of the KS Hamiltonian.

Substituting Eq. (2.43) into the right-hand side of Eq. (2.35) and performing a diagrammatic expansion as done in Ref. [93], one can show that it leads to the Dyson equation.

$$G(2,1) = G_0(2,1) + G_0(2,\bar{3}) \Sigma(\bar{3},\bar{4}) G(\bar{4},1), \tag{2.44}$$

where a bar above a variable denotes that integration is performed over that specific variable. The irreducible self-energy, $\Sigma(2,1)$, is given by $i$ times the sum of all connected Feynman diagrams that remain intact when a single electron line is cut [93, 105].

Similar to the single-particle Green's function, the irreducible self-energy can also be expressed in the single-particle KS basis, and its Fourier transform $\tilde{\Sigma}_{\mathbf{k},m,n}(\omega)$ is defined as:

$$\Sigma(2,1) = \sum_{\mathbf{k},m,n} \phi_{\mathbf{k},m}(\mathbf{r}_2) \phi^*_{\mathbf{k},n}(\mathbf{r}_1) \int \frac{d\omega}{2\pi} e^{-i\omega(t_2 - t_1)} \tilde{\Sigma}_{\mathbf{k},m,n}(\omega), \tag{2.45}$$

where, similar to the Green's function, we only have one $\mathbf{k}$ variable dependence due to translational symmetry and one frequency dependence due to time-translational invariance.

The Dyson equation in Fourier domain, in the single-particle KS basis, takes the form of a matrix equation given by

$$\tilde{G}_{\mathbf{k},a,b}(\omega) = \Big\{ \sum_c \tilde{G}_{0;\mathbf{k},a}(\omega) \tilde{\Sigma}_{\mathbf{k},a,c}(\omega) \tilde{G}_{\mathbf{k},c,b}(\omega) \Big\} + \delta_{a,b} \tilde{G}_{0;\mathbf{k},a}(\omega). \tag{2.46}$$

Substituting Eq. (2.39) into Eq. (2.46) and setting $\eta = 0$, we obtain

$$-\tilde{G}^{-1}_{\mathbf{k},a,b}(\omega) = (\epsilon_{\mathbf{k},a} - \omega)\delta_{a,b} + \tilde{\Sigma}_{\mathbf{k},a,b}(\omega). \tag{2.47}$$

From Eq. (2.47), we see that to obtain the exact single-particle Green's function in the KS basis, we need to know the irreducible self-energy in the KS basis. Since the irreducible self-energy is a function of the exact single-particle Green's function [105], we need to solve Eq. (2.47) self-consistently. However, computing the irreducible self-energy self-consistently is highly non-trivial, and therefore one makes a popular approximation known as the "*GW*" approximation [105, 53]. Within the GW approximation, the irreducible self-energy is given by [105, 93]

$$\Sigma(2,1) \approx -\delta(2,1)v^{(Hxc)}(2) - i\delta(2,1)v(2,\bar{3})G(3,\bar{3}^{+}) + iG(2,1)W(2,1), \tag{2.48}$$

where $v^{(Hxc)}(2)$ represents the sum of the Hartree potential and the exchange-correlation potential, i.e., $V_H(\rho_{\text{KS}},\mathbf{r})+V_{\text{xc}}(\rho_{\text{KS}},\mathbf{r})$, and $v(2,\bar{3})$ and $W(2,1)$ denote the bare and screened Coulomb interactions, respectively. Additionally, $\bar{3}^{+} \equiv (\mathbf{r}_3, t_3^{+})$ with $t_3^{+}$ infinitesimally greater than $t_3$ to ensure correct ordering of operators in time-ordered correlation functions.

The screened Coulomb interaction $W(2,1) = W(1,2)$ within the random phase approximation (RPA) [105] obeys a Dyson-like equation given by:

$$W(2,1) = v(2,1) + v(2,\bar{3})P(\bar{3},\bar{4})W(\bar{4},1). \tag{2.49}$$

Here, the irreducible polarizability $P(2,1)$, which is analogous to the irreducible self-energy, is written within the RPA as [93]

$$P(2,1) \approx P_0(2,1) \equiv -iG(2,1)G(1,2). \tag{2.50}$$

Even within the $GW$ and RPA approximations, one must solve Eqs. (2.46), (2.48), (2.49), and (2.50) self-consistently. However, in this thesis, we always used the implementations (we used the `YAMBO` code to perform the calculations) where it is solved non-self-consistently, referred to as the $G_0W_0$ approximation, which is given by [53, 65]

$$P(2,1) \approx P_0(2,1) \equiv -iG_0(2,1)G_0(1,2), \tag{2.51}$$

$$W(2,1) \approx W_0(2,1) \equiv v(2,1) + v(2,\bar{3})P_0(\bar{3},\bar{4})W_0(\bar{4},1), \tag{2.52}$$

$$\Sigma(2,1) \approx \Sigma_0(2,1) \equiv -\delta(2,1)v^{(xc)}(r_2) + iG_0(2,1)W_0(2,1), \tag{2.53}$$

$$G(2,1) \approx G_0(2,1) + G_0(2,\bar{3})\Sigma_0(\bar{3},\bar{4})G(\bar{4},1), \tag{2.54}$$

Moreover, we also employ the quasi-particle approximation (QPA) for the exact Green's function, which is approximated as [53, 65, 93]

$$\tilde{G}_{\mathbf{k},m,n}(\omega) \approx \delta_{m,n}\frac{Z^{(QP)}_{\mathbf{k},n}}{\omega - \epsilon^{(QP)}_{\mathbf{k},n} + i\frac{\gamma^{(QP)}_{\mathbf{k},n}}{2}}. \tag{2.55}$$

Here, the quasi-particle weight $Z^{(QP)}_{\mathbf{k},n}$, energy $\epsilon^{(QP)}_{\mathbf{k},n}$, and decay width $\gamma^{(QP)}_{\mathbf{k},n}$ are given by [93]

$$Z^{(QP)}_{\mathbf{k},n} \equiv \left[1 - \frac{\partial\tilde{\Sigma}_{\mathbf{k},n,n}(\omega)}{\partial\omega}\Big|_{\omega=\epsilon_{\mathbf{k},n}}\right]^{-1}, \tag{2.56}$$

$$\epsilon^{(QP)}_{\mathbf{k},n} \equiv \epsilon_{\mathbf{k},n} + \mathsf{Re}\left[Z^{(QP)}_{\mathbf{k},n}\tilde{\Sigma}_{\mathbf{k},n,n}(\omega)\Big|_{\omega=\epsilon_{\mathbf{k},n}}\right], \tag{2.57}$$

$$\gamma^{(QP)}_{\mathbf{k},n} \equiv -2\mathsf{Im}\left[Z^{(QP)}_{\mathbf{k},n}\tilde{\Sigma}_{\mathbf{k},n,n}(\omega)\Big|_{\omega=\epsilon_{\mathbf{k},n}}\right] \tag{2.58}$$

In the QPA, the exact Green's function can be written as

$$G(2,1)_{\mathsf{QPA}} \approx \sum_{\mathbf{k},n}\phi_{\mathbf{k},n}(\mathbf{r}_2)\phi^*_{\mathbf{k},n}(\mathbf{r}_1)\int\frac{d\omega}{2\pi}e^{-i\omega(t_2-t_1)}\frac{Z^{(QP)}_{\mathbf{k},n}}{\omega - \epsilon^{(QP)}_{\mathbf{k},n} + i\frac{\gamma^{(QP)}_{\mathbf{k},n}}{2}}. \tag{2.59}$$

The QPA is commonly employed when solving the Bethe-Salpeter equation, which will be discussed in the next section.

In practice, to obtain the quasiparticle energies given in Eq. (2.57), we first compute the polarizability $P(2,1)$ within the Random Phase Approximation (RPA), as defined in Eq. (2.51). The explicit expression is written as

$$P_0(\mathbf{r},\mathbf{r}';\omega) = \sum_{n,m}\frac{(f_n - f_m)\psi^*_n(\mathbf{r})\psi_m(\mathbf{r})\psi^*_m(\mathbf{r}')\psi_n(\mathbf{r}')}{\omega - (\varepsilon_m - \varepsilon_n) + i\eta}. \tag{2.60}$$

Once $P_0$ is obtained, we compute the inverse dielectric function, which is given by

$$\varepsilon^{-1}(\mathbf{r},\mathbf{r}';\omega) = \delta(\mathbf{r}-\mathbf{r}') + \int d\mathbf{r}''\, v(\mathbf{r},\mathbf{r}'')P_0(\mathbf{r}'',\mathbf{r}';\omega), \tag{2.61}$$

where $v(\mathbf{r},\mathbf{r}') = \frac{1}{|\mathbf{r}-\mathbf{r}'|}$ is the bare Coulomb interaction.

Using the inverse dielectric function, we can then construct the screened Coulomb interaction, which is given by [53]

$$W_0(\mathbf{r},\mathbf{r}';\omega) = \int d\mathbf{r}''\, \varepsilon^{-1}(\mathbf{r},\mathbf{r}'';\omega)v(\mathbf{r}'',\mathbf{r}'). \tag{2.62}$$

With the screening coloub interaction, the self-energy can be computed as [53]

$$\Sigma(\mathbf{r},\mathbf{r}';\omega) = \frac{i}{2\pi}\int d\omega'\, G_0(\mathbf{r},\mathbf{r}';\omega+\omega')W_0(\mathbf{r},\mathbf{r}';\omega')e^{i0^+\omega'}. \tag{2.63}$$

It should be noted that in Eq. (2.63), we need to evaluate $W_0$ over a range of frequencies, which makes the computation very expensive. To mitigate this, an analytical approximation for $\varepsilon^{-1}(\mathbf{r},\mathbf{r}';\omega)$ in Eq. (2.61) is used, known as the plasmon-pole model [40]. Once the self energy is obtained, we can then compute the quasi-particle corrections to the DFT quasi-particle energies.

With this discussion on the single-particle Green's function, we will now look into the two-particle correlation function in the next section. A more detailed discussion on GW approximation can be found in Refs. [53, 67, 83].

### 2.2.3 Two-particle correlation function

In order to describe excitons, we need to consider the two-particle Green's function, which describes the correlated movement of two charges. The two-particle Green's function is defined as

$$G^{(2)}(1,2;3,4) \equiv (-i)^2\langle 0|\hat{T}\{\psi(1)\psi(4)\psi^\dagger(2)\psi^\dagger(3)\}|0\rangle. \tag{2.64}$$

Similar to Eq. (2.35), one can expand the two-particle Green's function given in Eq. (2.64)

in terms of four Heisenberg time evolution operators. The exact two-particle Green's function in the interaction picture is given by

$$\langle 0|T\{\hat{\psi}(1)\hat{\psi}(4)\hat{\psi}^{\dagger}(2)\hat{\psi}^{\dagger}(3)\}|0\rangle = \frac{\langle\emptyset|\hat{T}\Big\{\hat{\psi}_I(1)\hat{\psi}_I(4)\hat{\psi}_I^{\dagger}(2)\hat{\psi}_I^{\dagger}(3)\exp\Big(-i\int_{-\infty}^{+\infty}dt\,\hat{H}_I(t)\Big)\Big\}|\emptyset\rangle}{\langle\emptyset|\hat{T}\Big\{\exp\Big(-i\int_{-\infty}^{+\infty}dt\,\hat{H}_I(t)\Big)\Big\}|\emptyset\rangle}, \tag{2.65}$$

where we use the same definitions as in Eq. (2.35). Similar to Eq. (2.34), one can define the independent two-particle Green's function as [93, 105]

$$G_0^{(2)}(1,2;3,4) = G(1,3)G(4,2) - G(1,2)G(4,3), \tag{2.66}$$

where $G(1,2)$ and others are single-particle Green's functions (the exact one's). We then define two-particle correlation function $L(1,2;3,4)$ as

$$L(1,2;3,4) \equiv G^{(2)}(1,2;3,4) + G(1,2)G(4,3). \tag{2.67}$$

From Eq. (2.67) and (2.66), the independent two-particle correlation function $L_0(1,2;3,4)$ is given by

$$L_0(1,2;3,4) = G(1,3)G(4,2). \tag{2.68}$$

Combining Eq. (2.65) and (2.67) and performing a diagrammatic expansion as done in Ref. [93], one arrives at a Dyson-like equation for the two-particle correlation function $L(1,2;3,4)$, very similar to the one-particle Green's function case:

$$L(1,2;3,4) = L_0(1,2;3,4) + L_0(1,2;\bar{5},\bar{6})K(\bar{5},\bar{6};\bar{7},\bar{8})L(\bar{7},\bar{8};3,4), \tag{2.69}$$

where $K(\bar{5},\bar{6};\bar{7},\bar{8})$ is known as the two-particle interaction kernel, which is analogous to the irreducible self-energy in the single-particle Green's function case.

Equation (2.69) is widely referred to as the "Bethe-Salpeter Equation" (BSE), and one typically solves this under certain approximations to obtain the excitonic energies and eigen-

states. The BSE is currently the state-of-the-art method for computing the properties of excitons.

The interaction kernel appearing in Eq. (2.69) can be written as a functional derivative of the self-energy $\{\Sigma(5,6) + \delta(5,6)v_{(Hxc)}(5)\}$ with respect to the Green's function $G(7,8)$ and is written as [105]

$$K(5,6;7,8) = \frac{\delta\{\Sigma(5,6) + \delta(5,6)v_{Hxc}(5)\}}{\delta G(7,8)}, \tag{2.70}$$

where $\Sigma(5,6)$ and $v_{Hxc}(5)$ are the self-energy and the Hartree potential, respectively, and $G(7,8)$ is the single-particle Green's function.

Within the GW approximation for the one-particle self-energy as given in Eq. (2.48), along with the assumption that $\frac{\delta W(5,6)}{\delta G(7,8)} \approx 0$, the interaction kernel $K(5,6;7,8)$ can be expressed as the sum of the attractive screened Coulomb interaction and the repulsive bare exchange interaction. It is then given by [53]:

$$\begin{aligned} K(5,6;7,8) = {} & iW(5,6)\delta(5,7)\delta(6,8) \\ & - iv(5,7)\delta(5,6)\delta(7,8), \end{aligned} \tag{2.71}$$

where $v(5,7)$ and $W(5,6)$ are the bare and screened Coulomb potentials as shown in previous section, respectively.

The BSE given in Eq. (2.69) is solved in the Fourier domain, similar to the Green's function or self-energy as shown in Eq. (2.45). The Fourier transform $\tilde{F}$ of the four-point function $F(1,2;3,4)$, where $F$ is either $K$ or $L$ in the single-particle KS basis, is defined as

$$\begin{aligned} F(1,2;3,4) \equiv \sum_{\substack{\mathbf{k}_1,\mathbf{k}_2,\mathbf{k}_3,\mathbf{k}_4 \\ a,b,c,d}} & \phi_{\mathbf{k}_1,a}(\mathbf{r}_1)\phi_{\mathbf{k}_4,d}(\mathbf{r}_4)\phi^*_{\mathbf{k}_2,b}(\mathbf{r}_2)\phi^*_{\mathbf{k}_3,c}(\mathbf{r}_3) \int \frac{d\omega}{2\pi} \int \frac{d\omega'}{2\pi} \int \frac{d\omega''}{2\pi} \\ & \times e^{-i\omega''(t_1-t_2)} e^{-i\omega(t_1-t_3)} e^{-i\omega'(t_4-t_2)} \tilde{F}_{\substack{\mathbf{k}_1 a,\mathbf{k}_2 b \\ \mathbf{k}_3 c,\mathbf{k}_4 d}}(\omega,\omega',\omega'') \,. \end{aligned} \tag{2.72}$$

In Eq. (2.72), we used time translational symmetry to reduce the dependence of $\tilde{F}$ from four to three variables. Moreover, due to translational symmetry, which will be demonstrated in the next chapter, the number of wavevectors can be reduced from four to three. The

wavevectors in Eq. (2.72) should satisfy the following relation (Eq. (3.19)):

$$\mathbf{k}_3 - \mathbf{k}_4 = \mathbf{k}_1 - \mathbf{k}_2 + \mathbf{G} = \mathbf{Q}. \tag{2.73}$$

Where $\mathbf{Q}$ is the wavevector corresponding to the transfer momentum. Using Eq. (3.19), we can write Eq. (2.72) as

$$\begin{aligned} F(1,2;3,4) \equiv & \sum_{\substack{\mathbf{k}_1,\mathbf{k}_3,\mathbf{Q} \\ a,b,c,d}} \phi_{\mathbf{k}_1,a}(\mathbf{r}_1)\phi_{\mathbf{k}_3-\mathbf{Q},d}(\mathbf{r}_4)\phi^*_{\mathbf{k}_1-\mathbf{Q},b}(\mathbf{r}_2)\phi^*_{\mathbf{k}_3,c}(\mathbf{r}_3) \int \frac{d\omega}{2\pi} \int \frac{d\omega'}{2\pi} \int \frac{d\omega''}{2\pi} \\ & \times e^{-i\omega'(t_4-t_2)} e^{-i\omega(t_1-t_3)} \tilde{F}_{\substack{\mathbf{k}_1 a,\mathbf{k}_1-\mathbf{Q}b \\ \mathbf{k}_3 c,\mathbf{k}_3-\mathbf{Q}d}}(\omega,\omega',\omega'') e^{-i\omega''(t_1-t_2)} \end{aligned} \tag{2.74}$$

The Fourier transform of the independent-particle correlation function $L_0$ has only two-frequencies and is defined as:

$$\begin{aligned} L_0(1,2;3,4) \equiv & \sum_{\substack{\mathbf{k}_1,\mathbf{Q} \\ a,b,c,d}} \phi_{\mathbf{k}_1,a}(\mathbf{r}_1)\ \phi_{\mathbf{k}_1-\mathbf{Q},d}(\mathbf{r}_4)\ \phi^*_{\mathbf{k}_1-\mathbf{Q},b}(\mathbf{r}_2)\ \phi^*_{\mathbf{k}_1,c}(\mathbf{r}_3) \\ & \times \int \frac{d\omega}{2\pi} \int \frac{d\omega_0}{2\pi} e^{-i\omega(t_1-t_3)} \tilde{L}_{\substack{\mathbf{k}_1 a,\mathbf{k}_1-\mathbf{Q}b \\ \mathbf{k}_1 c,\mathbf{k}_1-\mathbf{Q}d}}(\omega,\omega') e^{-i\omega'(t_4-t_2)} \end{aligned} \tag{2.75}$$

In Eq. (2.75), we used the fact that the independent two-particle correlation function is the product of two one-particle Green's functions. This implies that we can write the Fourier transform of $L_0$ as

$$\tilde{L}_{0,\substack{\mathbf{k}_1 a,\mathbf{k}_1-\mathbf{Q}b \\ \mathbf{k}_1 c,\mathbf{k}_1-\mathbf{Q}d}}(\omega,\omega') = \tilde{G}_{\mathbf{k}_1,ac}(\omega)\tilde{G}_{\mathbf{k}_1-\mathbf{Q},db}(\omega') \tag{2.76}$$

Furthermore, from Eq. (2.71), we can express the BSE kernel in Fourier space in the KS basis as

$$\tilde{K}_{\substack{\mathbf{k}_1 a,\mathbf{k}_1-\mathbf{Q}b \\ \mathbf{k}_3 c,\mathbf{k}_3-\mathbf{Q}d}}(\omega,\omega',\omega'') \approx i\tilde{W}_{\substack{\mathbf{k}_1 a,\mathbf{k}_1-\mathbf{Q}b \\ \mathbf{k}_3 c,\mathbf{k}_3-\mathbf{Q}d}}(\omega'') - i\tilde{v}_{\substack{\mathbf{k}_1 a,\mathbf{k}_1-\mathbf{Q}b \\ \mathbf{k}_3 c,\mathbf{k}_3-\mathbf{Q}d}} = \tilde{K}_{\substack{\mathbf{k}_1 a,\mathbf{k}_1-\mathbf{Q}b \\ \mathbf{k}_3 c,\mathbf{k}_3-\mathbf{Q}d}}(\omega''). \tag{2.77}$$

In practice, it is common to assume that the BSE kernel is static [93], which implies that we can neglect its frequency dependence. Under this approximation, the kernel can be

written as

$$\tilde{K}_{\substack{\mathbf{k}_1 a,\mathbf{k}_1-\mathbf{Q}b \\ \mathbf{k}_3 c,\mathbf{k}_3-\mathbf{Q}d}}(\omega'') \approx i\tilde{W}_{\substack{\mathbf{k}_1 a,\mathbf{k}_1-\mathbf{Q}b \\ \mathbf{k}_3 c,\mathbf{k}_3-\mathbf{Q}d}}(\omega''=0) - i\tilde{v}_{\substack{\mathbf{k}_1 a,\mathbf{k}_1-\mathbf{Q}b \\ \mathbf{k}_3 c,\mathbf{k}_3-\mathbf{Q}d}} \,. \tag{2.78}$$

The matrix elements $\tilde{W}_{\substack{\mathbf{k}_1 a,\mathbf{k}_1-\mathbf{Q}b \\ \mathbf{k}_3 c,\mathbf{k}_3-\mathbf{Q}d}}(\omega''=0)$ are commonly referred to as the direct term, and $\tilde{v}_{\substack{\mathbf{k}_1 a,\mathbf{k}_1-\mathbf{Q}b \\ \mathbf{k}_3 c,\mathbf{k}_3-\mathbf{Q}d}}$, known as the exchange term.

With these approximations and additional simplifications as shown in Ref. [93], the BSE given in Eq. (2.69) in the Fourier domain can be written as (see Ref. [93] for a detailed derivation)

$$\tilde{L}^{-1}_{\substack{\mathbf{k}_1 a,\mathbf{k}_1-\mathbf{Q}b \\ \mathbf{k}_3 c,\mathbf{k}_3-\mathbf{Q}d}}(\omega) = \delta_{\mathbf{k}_1,\mathbf{k}_3}\tilde{L}^{-1}_{0,\substack{\mathbf{k}_3 a,\mathbf{k}_3-\mathbf{Q}b \\ \mathbf{k}_3 c,\mathbf{k}_3-\mathbf{Q}d}}(\omega) - \tilde{K}_{\substack{\mathbf{k}_1 a,\mathbf{k}_1-\mathbf{Q}b \\ \mathbf{k}_3 c,\mathbf{k}_3-\mathbf{Q}d}} \,. \tag{2.79}$$

One further employs the QPA given in Eq. (2.59), neglecting the quasiparticle decay rate by setting $\gamma^{QP}_{\mathbf{k},a} \approx 0$ and assuming the quasiparticle weight factors are $Z^{QP}_{\mathbf{k},a} \approx 1$. Under these approximations, we obtain

$$\tilde{L}^{-1}_{0,\substack{\mathbf{k}_3 a,\mathbf{k}_3-\mathbf{Q}b \\ \mathbf{k}_3 c,\mathbf{k}_3-\mathbf{Q}d}}(\omega) \approx i\delta_{a,c}\delta_{b,d}\frac{f_{\mathbf{k_3},c} - f_{\mathbf{k_3}-\mathbf{Q},d}}{\omega - (\varepsilon_{\mathbf{k_3},c} - \varepsilon_{\mathbf{k_3}-\mathbf{Q},d})}, \tag{2.80}$$

where $f_{\mathbf{k_3},c}$ and $f_{\mathbf{k_3}-\mathbf{Q},d}$ are the occupation factors, while $\varepsilon_{\mathbf{k_3},c}$ and $\varepsilon_{\mathbf{k_3}-\mathbf{Q},d}$ denote the single-particle energies for states $(\mathbf{k_3}, c)$ and $(\mathbf{k_3}-\mathbf{Q}, d)$, respectively.

This implies that Eq. (2.79) can be written as

$$\tilde{L}_{\substack{\mathbf{k}_1 a,\mathbf{k}_1-\mathbf{Q}b \\ \mathbf{k}_3 c,\mathbf{k}_3-\mathbf{Q}d}}(\omega) = \frac{i(f_{\mathbf{k_3},c} - f_{\mathbf{k_3}-\mathbf{Q},d})}{\omega - \tilde{H}_{\substack{\mathbf{k}_1 a,\mathbf{k}_1-\mathbf{Q}b \\ \mathbf{k}_3 c,\mathbf{k}_3-\mathbf{Q}d}}}, \tag{2.81}$$

with

$$\tilde{H}_{\substack{\mathbf{k}_1 a,\mathbf{k}_1-\mathbf{Q}b \\ \mathbf{k}_3 c,\mathbf{k}_3-\mathbf{Q}d}} = \delta_{a,c}\delta_{b,d}\delta_{\mathbf{k_1},\mathbf{k_3}}(\varepsilon_{\mathbf{k_3},c} - \varepsilon_{\mathbf{k_3}-\mathbf{Q},d}) + i(f_{\mathbf{k_3},c} - f_{\mathbf{k_3}-\mathbf{Q},d})\tilde{K}_{\substack{\mathbf{k}_1 a,\mathbf{k}_1-\mathbf{Q}b \\ \mathbf{k}_3 c,\mathbf{k}_3-\mathbf{Q}d}} \,. \tag{2.82}$$

Here, $\tilde{H}^{(\mathbf{Q})}_{\substack{\mathbf{k}_1 a,\mathbf{k}_1-\mathbf{Q}b \\ \mathbf{k}_3 c,\mathbf{k}_3-\mathbf{Q}d}}$ represents the excitonic Hamiltonian for the transferred momentum $\mathbf{Q}$. In general, $\tilde{H}^{(\mathbf{Q})}_{\substack{\mathbf{k}_1 a,\mathbf{k}_1-\mathbf{Q}b \\ \mathbf{k}_3 c,\mathbf{k}_3-\mathbf{Q}d}}$ is not Hermitian. From the eigenvalues and the left and right eigenvectors of the excitonic Hamiltonian, one can obtain the two-particle correlation function given

in Eq. (2.81).

The occupation factors $f_{\mathbf{k},a}$ in Eq. (2.82) are given by $f_{\mathbf{k},a} = 1$ if $a$ belongs to the valence band and $f_{\mathbf{k},a} = 0$ if $a$ belongs to the conduction band. This implies that we can write the BSE Hamiltonian given in Eq. (2.82) as a $2 \times 2$ block matrix, given by

$$H_{2p} = \begin{pmatrix} R & C \\ -C^{\dagger} & -D \end{pmatrix} \tag{2.83}$$

where $R$ and $D$ are known as the resonant and anti-resonant blocks, respectively, while $C$ is referred to as the coupling block. Let $\tilde{c}, \tilde{c}'$ belong to conduction bands and $\tilde{v}, \tilde{v}'$ belong to valence bands. Then, the resonant block is Hermitian and is given by

$$R_{\substack{\mathbf{k}_1\tilde{c}',\mathbf{k}_1-\mathbf{Q}\tilde{v}' \\ \mathbf{k}_3\tilde{c},\mathbf{k}_3-\mathbf{Q}\tilde{v}}} = \delta_{\tilde{c}',\tilde{c}}\delta_{\tilde{v}',\tilde{v}}\delta_{\mathbf{k_1},\mathbf{k_3}}(\varepsilon_{\mathbf{k_3},\tilde{c}} - \varepsilon_{\mathbf{k_3}-\mathbf{Q},\tilde{v}}) - i\tilde{K}_{\substack{\mathbf{k}_1\tilde{c}',\mathbf{k}_1-\mathbf{Q}\tilde{v}' \\ \mathbf{k}_3\tilde{c},\mathbf{k}_3-\mathbf{Q}\tilde{v}}}. \tag{2.84}$$

The anti-resonant block is Hermitian and is given by

$$D_{\substack{\mathbf{k}_1\tilde{v}',\mathbf{k}_1-\mathbf{Q}\tilde{c}' \\ \mathbf{k}_3\tilde{v},\mathbf{k}_3-\mathbf{Q}\tilde{c}}} = \delta_{\tilde{c}',\tilde{c}}\delta_{\tilde{v}',\tilde{v}}\delta_{\mathbf{k_1},\mathbf{k_3}}(-\varepsilon_{\mathbf{k_3},\tilde{v}} + \varepsilon_{\mathbf{k_3}-\mathbf{Q},\tilde{c}}) - i\tilde{K}_{\substack{\mathbf{k}_1\tilde{v}',\mathbf{k}_1-\mathbf{Q}\tilde{c}' \\ \mathbf{k}_3\tilde{v},\mathbf{k}_3-\mathbf{Q}\tilde{c}}}. \tag{2.85}$$

The coupling block $C$ is given by

$$C_{\substack{\mathbf{k}_1\tilde{c}',\mathbf{k}_1-\mathbf{Q}\tilde{v}' \\ \mathbf{k}_3\tilde{v},\mathbf{k}_3-\mathbf{Q}\tilde{c}}} = i\tilde{K}_{\substack{\mathbf{k}_1\tilde{c}',\mathbf{k}_1-\mathbf{Q}\tilde{v}' \\ \mathbf{k}_3\tilde{v},\mathbf{k}_3-\mathbf{Q}\tilde{c}}}. \tag{2.86}$$

One often sets the coupling block $C = 0$, which is commonly referred to as the Tamm-Dancoff Approximation. Throughout this thesis, we employ this approximation, as it makes the excitonic Hamiltonian Hermitian and greatly simplifies the expressions when computing observables.

By diagonalizing the matrix given in Eq. (2.83), we obtain the excitonic energies and eigenstates and is written as

$$\begin{pmatrix} R^{(\mathbf{Q})} & C^{(\mathbf{Q})} \\ -\left(C^{(\mathbf{Q})}\right)^{\dagger} & -D^{(\mathbf{Q})} \end{pmatrix} \begin{pmatrix} A^{(\mathbf{Q})} \\ B^{(\mathbf{Q})} \end{pmatrix} = \varepsilon_S^{(\mathbf{Q})} \begin{pmatrix} A^{(\mathbf{Q})} \\ B^{(\mathbf{Q})} \end{pmatrix}, \tag{2.87}$$

where $X = \begin{pmatrix} A^{(\mathbf{Q})} \\ B^{(\mathbf{Q})} \end{pmatrix}$ is the right excitonic wavefunction in the electron-hole basis, often referred to as the envelope wavefunction. Eq. (2.87) is explicitly written as

$$\begin{aligned}
\sum_{\mathbf{k_3},\tilde{c}\tilde{v}} \Big\{ \delta_{\tilde{c}',\tilde{c}}\delta_{\tilde{v}',\tilde{v}}\delta_{\mathbf{k_1},\mathbf{k_3}}(\varepsilon_{\mathbf{k_3},\tilde{c}} - \varepsilon_{\mathbf{k_3}-\mathbf{Q},\tilde{v}}) - i\tilde{K}_{\substack{\mathbf{k}_1\tilde{c}',\mathbf{k}_1-\mathbf{Q}\tilde{v}' \\ \mathbf{k}_3\tilde{c},\mathbf{k}_3-\mathbf{Q}\tilde{v}}} \Big\} A^{S,(\mathbf{Q})}_{\mathbf{k_3},\tilde{c}\tilde{v}} + \\
i \sum_{\mathbf{k_3},\tilde{c}\tilde{v}} \Big\{ \tilde{K}_{\substack{\mathbf{k}_1\tilde{c}',\mathbf{k}_1-\mathbf{Q}\tilde{v}'\cdot \\ \mathbf{k}_3\tilde{v},\mathbf{k}_3-\mathbf{Q}\tilde{c}}} \Big\} B^{S,(\mathbf{Q})}_{\mathbf{k_3},\tilde{c}\tilde{v}} = \varepsilon^{S,(\mathbf{Q})} A^{S,(\mathbf{Q})}_{\mathbf{k_1},\tilde{c}'\tilde{v}'} \\
\sum_{\mathbf{k_3},\tilde{c}\tilde{v}} \Big\{ \delta_{\tilde{c}',\tilde{c}}\delta_{\tilde{v}',\tilde{v}}\delta_{\mathbf{k_1},\mathbf{k_3}}(-\varepsilon_{\mathbf{k_3},\tilde{v}} + \varepsilon_{\mathbf{k_3}-\mathbf{Q},\tilde{c}}) - i\tilde{K}_{\substack{\mathbf{k}_1\tilde{v}',\mathbf{k}_1-\mathbf{Q}\tilde{c}' \\ \mathbf{k}_3\tilde{v},\mathbf{k}_3-\mathbf{Q}\tilde{c}}} \Big\} B^{S,(\mathbf{Q})}_{\mathbf{k_3},\tilde{c}\tilde{v}} + \\
- i \sum_{\mathbf{k_3},\tilde{c}\tilde{v}} \Big\{ \tilde{K}^{*}_{\substack{\mathbf{k}_3\tilde{v},\mathbf{k}_3-\mathbf{Q}\tilde{c}\,\cdot \\ \mathbf{k}_1\tilde{c}',\mathbf{k}_1-\mathbf{Q}\tilde{v}'}} \Big\} A^{S,(\mathbf{Q})}_{\mathbf{k_3},\tilde{c}\tilde{v}} = -\varepsilon^{S,(\mathbf{Q})} B^{S,(\mathbf{Q})}_{\mathbf{k_1},\tilde{c}'\tilde{v}'}.
\end{aligned} \tag{2.88}$$

In order to compute the kernel matrix elements in Eq. (2.88), we need to evaluate the bare-exchange term and the screened Coulomb term, which are explicitly written as:

$$\begin{aligned}
V^{n_1,n_2}_{n_5,n_6} &= \int d\mathbf{r}\, d\mathbf{r}'\, \phi_{n_1}(\mathbf{r})\phi^*_{n_2}(\mathbf{r}) \frac{1}{|\mathbf{r}-\mathbf{r}'|} \phi^*_{n_5}(\mathbf{r}')\psi_{n_6}(\mathbf{r}'), \\
W^{n_1,n_2}_{n_5,n_6}(\omega) &= \int d\mathbf{r}\, d\mathbf{r}'\, d\mathbf{r}''\, \phi_{n_1}(\mathbf{r})\phi^*_{n_2}(\mathbf{r}') \frac{\epsilon^{-1}(\mathbf{r},\mathbf{r}'';\omega)}{|\mathbf{r}''-\mathbf{r}'|} \phi^*_{n_5}(\mathbf{r})\phi_{n_6}(\mathbf{r}'),
\end{aligned}$$

where $n_i = (\mathbf{k}_i, m_i)$, with $m_i$ being the band index.

Once we obtain the exciton wavefunctions in electron-hole basis, the exciton wavefunction in the position basis is then given by

$$\Psi^{\mathbf{Q}}_S(\mathbf{r}_e,\mathbf{r}_h) = \sum_{\mathbf{k}cv} A^{S,(\mathbf{Q})}_{\mathbf{k},cv}\, \phi_{\mathbf{k}c}(\mathbf{r}_e)\, \phi^*_{\mathbf{k}-\mathbf{Q},v}(\mathbf{r}_h) + \sum_{\mathbf{k}cv} B^{S,(\mathbf{Q})}_{\mathbf{k},cv}\, \phi_{\mathbf{k}v}(\mathbf{r}_e)\, \phi^*_{\mathbf{k}-\mathbf{Q},c}(\mathbf{r}_h). \tag{2.89}$$

When the Tamm-Dancoff Approximation (TDA) is employed, the diagonalization is restricted to the resonant block to obtain the positive eigenspectrum, i.e.,

$$R^{(\mathbf{Q})} A^{(\mathbf{Q})} = \varepsilon^{(\mathbf{Q})}_S A^{(\mathbf{Q})}. \tag{2.90}$$

After the diagonalization, one can obtain the two-particle coorealtion given in Eq. (2.81)

as

$$\tilde{L}_{\substack{\mathbf{k}_1 a, \mathbf{k}_1 - \mathbf{Q} b \\ \mathbf{k}_3 c, \mathbf{k}_3 - \mathbf{Q} d}}(\omega) = \sum_S \frac{i(f_{\mathbf{k_3}, c} - f_{\mathbf{k_3} - \mathbf{Q}, d})}{\omega - \varepsilon_S^{\mathbf{Q}}} X^{S,\mathbf{Q}}_{\mathbf{k}_3 c, \mathbf{k}_3 - \mathbf{Q} d} (Y^{S,\mathbf{Q}}_{\mathbf{k}_1 a, \mathbf{k}_1 - \mathbf{Q} b})^*, \tag{2.91}$$

where $Y^S$ are the left eigenvectors, chosen such that the overlap matrix with the right eigenvectors is the identity matrix.

Once we have obtained the exciton energies and eigenstates, we can then compute properties including excitonic effects. For example, within TDA, we can obtain the imaginary part of the 2D polarizability tensor, which represents the absorption spectrum of a 2S material and is given by tensor [98]:

$$\text{Im}\{\alpha^{\mu}_{2D}(\omega)\} = \frac{2\pi e^2}{A_{uc}\omega^2} \sum_S \Big| \sum_{vc\mathbf{k}} A^S_{vc\mathbf{k}} \langle v\mathbf{k}|v^{\mu}|c\mathbf{k}\rangle \Big|^2 \delta(\omega - \varepsilon_S), \tag{2.92}$$

where $A_{uc}$ is the unit cell area, $v^{\mu}$ is the velocity operator component along $\mu$, $A^S_{vc\mathbf{k}}$ are exciton expansion coefficients, and $\varepsilon_S$ is the exciton energy.

Before concluding this brief review of the BSE formalism, we present an application of the GW-BSE method to compute the absorption spectrum of a new class of 2D materials with an indirect gap. These materials have the general formula $MX_2$, where M represents a pnictogen and X represents a chalcogen, as shown in Fig. 2.1. This work is adapted from Ref. [71].

### 2.2.4 Optical Properties and Many-Body Effects of $MX_2$ monolayer

Fig 2.2 shows the electronic band structures of all r-$MX_2$ monolayers calculated using the $G_0W_0$ [7, 99, 65] (solid lines) and PBE [87] (dashed lines) methods, including spin-orbit coupling (SOC) effects. We observe that the overall band dispersion does not change significantly with the choice of the exchange-correlation (XC) functional. However, the bandgap varies considerably depending on the XC functional employed (see Table 2.1).

While SOC effects are negligible for lighter elements, they become substantial for heavier constituent elements, particularly in the $BiX_2$ series. Notably, there is no SOC-induced spin splitting of bands due to the centrosymmetric structure of r-$MX_2$ monolayers.

| r-$MX_2$ mono-layer | PBE | PBE +SOC | HSE06 | HSE06 +SOC | $G_0W_0$ +SOC |
|---|---|---|---|---|---|
| $AsS_2$ | 1.25 | 1.17 | 1.92 | 1.91 | 2.01 |
| $AsSe_2$ | 0.96 | 0.88 | 1.54 | 1.51 | 2.06 |
| $AsTe_2$ | 0.52 | 0.48 | 0.98 | 0.83 | 1.38 |
| $SbS_2$ | 1.42 | 1.35 | 2.12 | 2.08 | 2.24 |
| $SbSe_2$ | 1.09 | 1.03 | 1.69 | 1.62 | 2.23 |
| $SbTe_2$ | 0.65 | 0.63 | 1.10 | 1.00 | 1.57 |
| $BiS_2$ | 1.47 | 1.04 | 2.20 | 1.87 | 1.84 |
| $BiSe_2$ | 1.17 | 0.76 | 1.81 | 1.45 | 1.82 |
| $BiTe_2$ | 0.70 | 0.26 | 1.19 | 0.73 | 0.83 |

Table 2.1: Bandgaps (in eV) of r-$MX_2$ monolayers calculated using PBE, PBE+SOC, HSE06, HSE06+SOC, and $G_0W_0$+SOC.

To obtain the absorption spectrum, including electron-hole interactions, we solve the Bethe-Salpeter equation (BSE) [98] on top of the $G_0W_0$ calculations within the Tamm-Dancoff approximation [7], using the YAMBO code [99].

The optical spectra reveal strongly bound excitons dominating absorption for all r-$MX_2$ monolayers. A significant shift in the absorption onset upon including excitonic effects indicates large exciton binding energies, similar to $MoS_2$ and other transition metal dichalcogenides [75, 113].

| First bright exciton energies of $MX_2$ monolayers (in eV) | | | |
|---|---|---|---|
| $MX_2$ | S | Se | Te |
| As | 1.97 | 1.91 | 1.07 |
| Sb | 2.00 | 2.01 | 1.34 |
| Bi | 1.20 | 1.26 | 0.45 |

Table 2.2: First bright exciton energies of $MX_2$ monolayers calculated using BSE+$G_0W_0$+SOC.

The dielectric screening increases with heavier chalcogens, resulting in a redshift of the absorption onset. However, no clear trend is observed with pnictogen elements, with Sb-based compounds exhibiting the highest bandgaps and exciton energies.

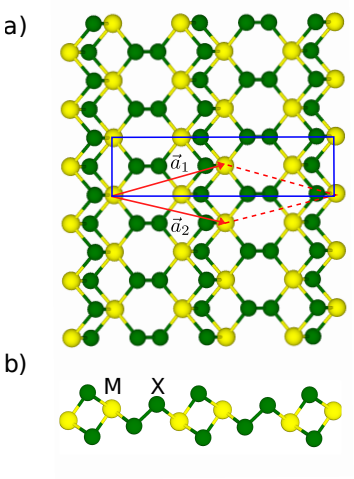


Figure 2.1: a) Top and b) side views of the studied r-$MX_2$ monolayer. The conventional (blue) and primitive (red) unit cells are illustrated in panel (a).

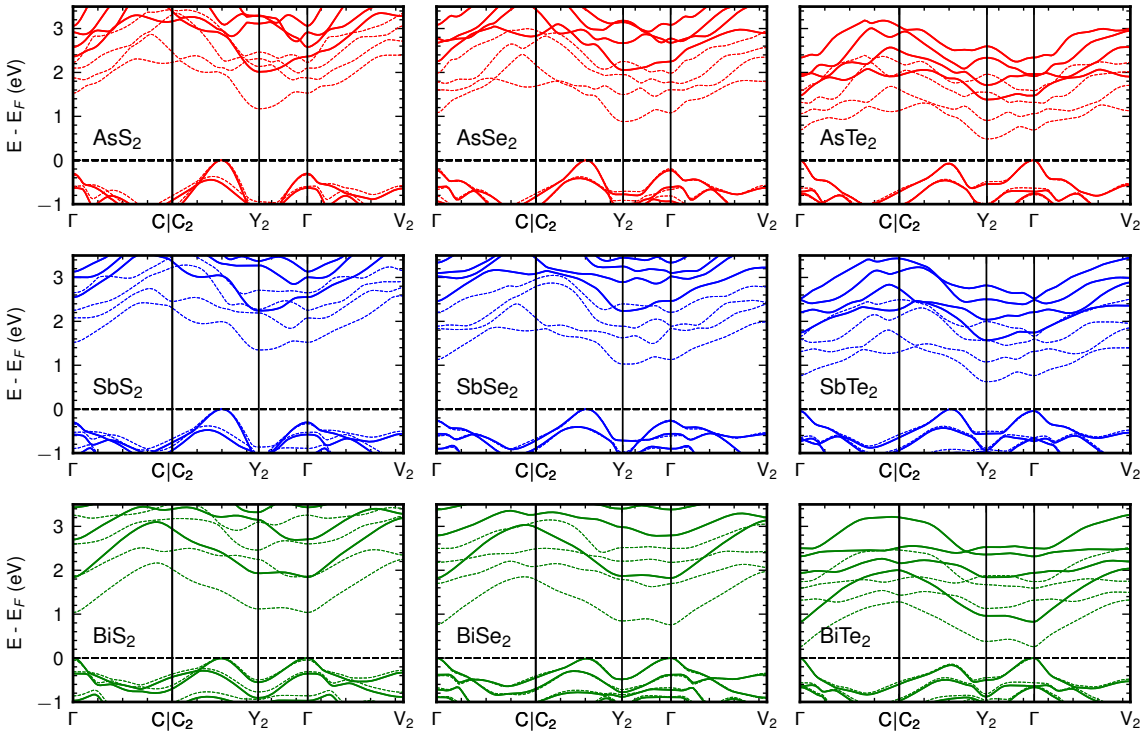


Figure 2.2: Electronic band structure of r-$MX_2$ monolayers calculated using $G_0W_0$ (solid lines) and PBE (dashed lines), including spin-orbit coupling effects. The Fermi energy ($E_F$) is set at the valence band maximum.

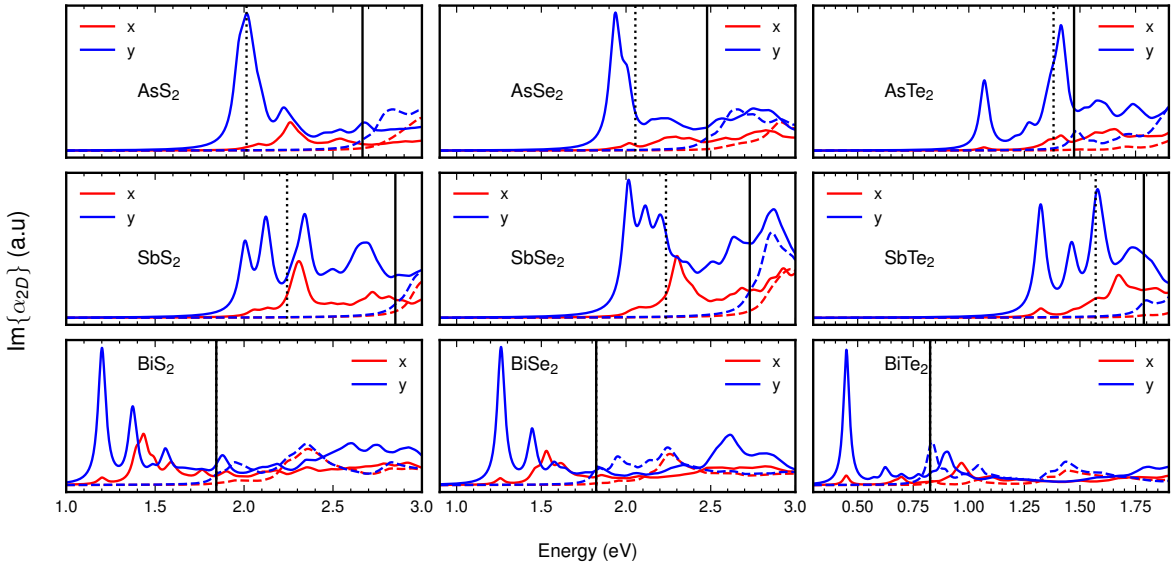


Figure 2.3: Optical absorption spectra for different r-$MX_2$ monolayers. The solid and dashed lines correspond to calculations with and without electron-hole interactions. The red and blue lines represent absorption along x and y polarization directions, respectively.

Finally, we analyze the anisotropic absorption of these materials. Unlike BP, where excitons exhibit distinct x/y coupling due to $D_{2h}$ symmetry, r-$MX_2$ monolayers ($C_{2h}$) show excitons coupling to both x and y polarizations, though with different intensities. The greater oscillator strength along the y-direction results from the crystal's in-plane anisotropy.

**Calculation details:**

All DFT calculations were performed using the QUANTUM ESPRESSO (QE) package [37] with the Perdew-Burke-Ernzerhof (PBE) exchange-correlation (XC) functional [87]. We used fully relativistic norm-conserving pseudopotentials from the PSEUDODOJO project [108] for the QE calculations. Spin-orbit coupling (SOC) was included in all the calculations unless specified otherwise.

Next for the $GW$ calculations, we first obtained the Kohn-Sham energies and wave functions on a uniform $9 \times 9 \times 1$ k-point grid by performing a non self-consistent calculation with a plane wave cutoff of 80 Ry using the QE code. In order to construct the microscopic dielectric tensor, we used a plane wave cutoff of 8 Ry and performed the summation with

1000 Kohn-Sham states. The frequency dependence of the dielectric tensor was described within a plasmon-pole approximation [40]. A 2D Coulomb cutoff along the out-of-plane was employed to remove the interactions with periodic images. In order to speed up the convergence of $G_0W_0$ calculations with respect to bands and k-points, we used a G-terminator [10] and RIM-W [44] technique, respectively.

To obtain well-converged absorption spectra, we used a uniform $\Gamma$-centred $30 \times 30 \times 1$ k-point grid for all r-$MX_2$ monolayers. A total of 250 bands and a cut-off of 4 Ry were used to build the static dielectric tensor. We included the top eight valence and the bottom eight conduction bands to construct the BSE interaction kernel. A plane-wave cutoff of 60 Ry and 4 Ry was used in the construction of bare exchange and screened Coulomb blocks, respectively.

In the next chapters, we will use the formalism introduced here to explore excitonic symmetries and exciton-phonon coupling phenomena.

# Chapter 3

# Symmetries of Excitons

In the previous chapter, we briefly presented some basic concepts of group theory and introduced the GW and BSE formalisms, which are state-of-the-art methods for computing exciton energies and eigenstates. One important aspect of excitons is their symmetry properties, which govern their optical selection rules and interactions with other quasiparticles.

Traditionally, the symmetries of excitonic states have been described by modeling them as hydrogenic systems and assigning atomic orbitals to their solutions. For example, in materials with strong dielectric screening, if the exciton consists mainly of transitions at the band extrema, only “s-like” excitons are optically active (bright) [30].

As mentioned earlier, although the hydrogenic model adequately describes the dipole selection rules in conventional bulk semiconductors with Wannier-Mott-type excitons [116], it fails to capture the selection rules for excitons that deviate from this type. For example, excitons in monolayer transition metal dichalcogenides (TMDCs) are known to deviate significantly from the hydrogenic Rydberg series [19]. Moreover, the hydrogenic model is insufficient for studying selection rules in processes such as exciton-phonon scattering. Therefore, more robust approaches are needed to understand the symmetries of all types of excitons.

In this chapter, we rigorously employ group theory methods to study the symmetry properties of the excitonic states obtained from the BSE. The contents of this chapter are planned to be integrated into a publication [80].

Before we study the symmetries of excitonic states, we first examine the symmetries of

the underlying electronic states.

## 3.1 Symmetries of electronic states in crystals

The set of all spatial symmetries that leave the crystal invariant forms a space group $\mathcal{G}$. The unitary operators $\hat{U}(g)$, for all $g \in \mathcal{G}$, form a projective representation (or a linear representation if spin is neglected) of $\mathcal{G}$ on the Hilbert space of electronic states [121, 118, 2]. It is worthwhile to highlight that one can work with linear representations of a much larger group instead of working with projective representations, which gives rise to the concept of double point groups [25] when dealing with projective representations of point groups with spin-orbit coupling in crystals. The electronic Hamiltonian $\hat{\mathcal{H}}$ remains invariant under the action of $g$ if and only if $\hat{U}(g)$ commutes with $\hat{\mathcal{H}}$, which is expressed as $[\hat{\mathcal{H}}, \hat{U}(g)] = 0$ [107].

Within the group $\mathcal{G}$, the set of all pure translational symmetries forms a normal subgroup $\mathcal{T}$ of $\mathcal{G}$. The group $\mathcal{T}$ is abelian, as the group multiplication is commutative. The space group $\mathcal{G}$ can be decomposed into unique left (or right) cosets of the subgroup $\mathcal{T}$ in $\mathcal{G}$, which is written as

$$\mathcal{G} \equiv \bigcup_{i=1}^{n} g_i \mathcal{T}, \tag{3.1}$$

where $g_i$ are the coset representatives, $g_i\mathcal{T}$ represents the cosets of $\mathcal{T}$ in $\mathcal{G}$, and $n$ is the index of $\mathcal{T}$ in $\mathcal{G}$. Since $\mathcal{T}$ is a normal subgroup of $\mathcal{G}$, it follows that the set of all left (or right) cosets of $\mathcal{T}$ in $\mathcal{G}$ forms the quotient group, represented by $\mathcal{G}/\mathcal{T}$ which is isomorphic to the point group $\mathcal{P}$ of the crystal [29]. The point group $\mathcal{P}$ is the set obtained by removing the translational components from the elements of the space group $\mathcal{G}$. It can happen that $\mathcal{P}$ is not be a subgroup of $\mathcal{G}$.

Since the Hamiltonian $\hat{\mathcal{H}}$ commutes with all elements in $\mathcal{T}$, it follows that both $\hat{\mathcal{H}}$ and $\hat{U}(g)$ for all $g \in \mathcal{T}$ can be simultaneously block-diagonalized, with each block classified by the one-dimensional irreducible representations of $\mathcal{T}$. Upon imposing the Born–von Karman boundary condition [4], these irreducible representations are labeled by the wavevector $\mathbf{k}$, which is restricted to the first Brillouin zone of reciprocal space. This allows us to express the eigenstates of $\hat{\mathcal{H}}$, which are Bloch states [107, 25, 29], as:

$$\psi_{\mathbf{k},m,\sigma}(\mathbf{r}) = e^{i\mathbf{k}\cdot\mathbf{r}} u_{\mathbf{k},m,\sigma}(\mathbf{r}), \tag{3.2}$$

where $u_{\mathbf{k},m,\sigma}(\mathbf{r})$ is the periodic part of the wavefunction, determined by the structure of the potential. Here, $m$ and $\sigma$ denote the band and spin indices, respectively.

The set of all symmetries in $\mathcal{G}$ that leave the wavevector $\mathbf{k}$ unchanged (up to a reciprocal lattice vector) forms the little group $\mathcal{G}_\mathbf{k}$ of $\mathbf{k}$, which is a subgroup of $\mathcal{G}$. The quotient group $\mathcal{G}_\mathbf{k}/\mathcal{T}$ is isomorphic to the little point group $\mathcal{P}_\mathbf{k}$ of $\mathbf{k}$, which is a subgroup of the point group of the crystal, $\mathcal{P}$.

Now, consider an element $g = \{R \mid \boldsymbol{\tau}\} \in \mathcal{G}$, which transforms the position vector $\mathbf{r}$ as $\mathbf{r} \to R\mathbf{r} + \boldsymbol{\tau}$, where $R$ is an orthogonal matrix and $\boldsymbol{\tau}$ is a translation, potentially a fractional multiple of the lattice vectors. The operator $\hat{U}(g)$ acts on the Bloch state $\psi_{\mathbf{k},m,\sigma}(\mathbf{r})$ as [2, 29]:

$$\hat{U}(g)\psi_{\mathbf{k},m,\sigma}(\mathbf{r}) = S_{\sigma'\sigma}(R)\psi_{\mathbf{k},m,\sigma}(R^{-1}(\mathbf{r} - \boldsymbol{\tau})), \tag{3.3}$$

where $S(R) = e^{-i\frac{\phi}{2}\hat{\mathbf{n}}\cdot\vec{\sigma}}$ is a $2 \times 2$ unitary matrix acting on the spinorial subspace of the electronic wavefunction. Here, $\vec{\sigma} = (\sigma_x, \sigma_y, \sigma_z)$ denotes the Pauli matrices, and $\hat{\mathbf{n}}$ and $\phi$ are the axis and angle of the orthogonal matrix $R$ (we treat improper rotations as product of proper rotation and inversion. As angular momentum is invariant under inversion, for improper rotations, $\hat{\mathbf{n}}$ and $\phi$ correspond to the matrix $-R$). If spin is neglected, $S(R)$ reduces to the $1 \times 1$ identity matrix.

Under the action of $g$, the wavefunction remains an eigenstate of $\hat{\mathcal{H}}$ but transforms to a wavevector $\mathbf{k}' = R\mathbf{k} + \mathbf{G}$, where $\mathbf{G}$ is a reciprocal lattice vector ensuring that $R\mathbf{k}$ lies within the first Brillouin zone [25]. Throughout this work, we adopt the convention $\psi_\mathbf{k}(\mathbf{r}) = \psi_{\mathbf{k}+\mathbf{G}}(\mathbf{r})$, known as the *periodic gauge*.

Assuming that the wave functions $\psi_{\mathbf{k},m',\sigma'}$ form an orthonormal set (for all $\mathbf{k}$), the wavefunctions $\hat{U}(g)\psi_{\mathbf{k},m,\sigma}(\mathbf{r})$ and $\psi_{R\mathbf{k},m,\sigma}(\mathbf{r})$ represent the same physical state, differing only by a phase (or a unitary rotation for degenerate states). This relation is expressed as:

$$\hat{U}(g)\psi_{\mathbf{k},m,\sigma}(\mathbf{r}) = \sum_{m'} \mathcal{D}_{\mathbf{k},m'm}(g)\psi_{R\mathbf{k},m',\sigma'}(\mathbf{r}), \tag{3.4}$$

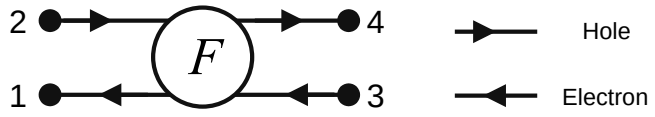


Figure 3.1: Feynman diagram for an arbitrary four-point function $F(1,2;3,4)$.

where $\mathcal{D}_{\mathbf{k}}(g) = \bigoplus_i \mathcal{D}_{\mathbf{k},i}(g)$ is a block-diagonal unitary matrix, with each block $\mathcal{D}_{\mathbf{k},i}(g)$ corresponding to a degenerate subspace that is preserved under the action of all symmetry operations (invariant subspace). The matrix $\mathcal{D}_{\mathbf{k}}(g)$ is given by:

$$\mathcal{D}_{\mathbf{k},m'm}(g) = \sum_{\sigma,\sigma'} \int \psi^*_{R\mathbf{k},m',\sigma'}(\mathbf{r}) S_{\sigma'\sigma}(R) \psi_{\mathbf{k},m,\sigma}(R^{-1}(\mathbf{r}-\boldsymbol{\tau}))\, d^3\mathbf{r}. \tag{3.5}$$

The unitary matrices $\mathcal{D}_{\mathbf{k}}(g)$ for all $g \in \mathcal{G}$ and k-points are central to the analysis of electronic-state symmetries in crystals. If $g$ belongs to the little group of $\mathbf{k}$, then $\mathcal{D}_{\mathbf{k}}(g)$ corresponds to the representation matrices of the symmetry operation, which can be further decomposed into irreducible representations of the electronic states.

Furthermore, the matrices $\mathcal{D}_{\mathbf{k}}$ can be extended to incorporate time-reversal symmetry $\mathscr{T}$, which is given by

$$\mathcal{D}_{\mathbf{k},m'm}(\mathscr{T}) = \sum_{\sigma,\sigma'} \int \psi^*_{-\mathbf{k},m',\sigma'}(\mathbf{r}) S_{\sigma'\sigma}(\mathscr{T}) \psi^*_{\mathbf{k},m,\sigma}(\mathbf{r})\, d^3\mathbf{r}. \tag{3.6}$$

where $S(\mathscr{T}) = -i\sigma_y$, or the $1 \times 1$ identity matrix if spin is neglected.

## 3.2 Symmetries of excitons

Building on this foundation, we now examine the symmetries of excitonic states. The exciton energies and eigenstates are obtained by solving the Bethe–Salpeter equation (BSE) [98, 1], as shown in the previous chapter. To understand the symmetry properties of excitons, we study the symmetries of the BSE itself. Rather than working directly with the BSE, we first generalize the symmetry analysis to an arbitrary four-point function that is invariant under symmetry operations. This general framework is then applied to the BSE as a special case.

Consider a generic four-point function $F(1,2;3,4)$, represented by the Feynman diagram shown in Fig. 3.1, where the indices denote position and time coordinates, e.g., $1 \to (\mathbf{r}_1\sigma_1, t_1)$. The Fourier transform of $F(1,2;3,4)$ in the time domain, denoted as $\tilde{F} = \tilde{F}(\mathbf{r}_1\sigma_1, \mathbf{r}_2\sigma_2; \mathbf{r}_3\sigma_3, \mathbf{r}_4\sigma_4; \omega, \omega', \omega'')$, can be expanded in terms of non-interacting one-electron Bloch states $\phi(\mathbf{r})$, which form an orthonormal basis, and is given by [93, 105] [1]:

$$\tilde{F} = \sum_{\substack{\mathbf{k}_1,\mathbf{k}_2,\mathbf{k}_3,\mathbf{k}_4 \\ a,b,c,d}} \phi_{\mathbf{k}_1,a,\sigma_1}(\mathbf{r}_1)\phi_{\mathbf{k}_4,d,\sigma_4}(\mathbf{r}_4)\phi^*_{\mathbf{k}_2,b,\sigma_2}(\mathbf{r}_2)\phi^*_{\mathbf{k}_3,c,\sigma_3}(\mathbf{r}_3)\tilde{F}_{\substack{\mathbf{k}_1 a,\mathbf{k}_2 b \\ \mathbf{k}_3 c,\mathbf{k}_4 d}}(\omega,\omega',\omega''), \tag{3.7}$$

where the matrix $\tilde{F}_{\substack{\mathbf{k}_1 a,\mathbf{k}_2 b \\ \mathbf{k}_3 c,\mathbf{k}_4 d}}(\omega,\omega',\omega'')$ represents the Fourier transform $\tilde{F}$ in the basis of one-electron Bloch states. Here, the indices $a$ and $c$ denote the band indices of the electron, while $b$ and $d$ correspond to the band indices of the hole.

Now consider the action of $\hat{U}(g)$ on the fourier transform of the four-point function, which is given by

$$\hat{U}(g)\tilde{F} = \tilde{F}' = \tilde{F}(\mathbf{r}'_1\sigma'_1, \mathbf{r}'_2\sigma'_2; \mathbf{r}'_3\sigma'_3, \mathbf{r}'_4\sigma'_4; \omega, \omega', \omega'') \tag{3.8}$$

where $\mathbf{r}'_i = R^{-1}(\mathbf{r}_i - \boldsymbol{\tau})\ \forall i \in \{1,2,3,4\}$. Combining Eqs. (3.7) and (3.8), and employing Eq. 3.4 we obtain

$$\begin{aligned}\tilde{F}' = \sum_{\substack{\mathbf{k}_1,\mathbf{k}_2,\mathbf{k}_3,\mathbf{k}_4 \\ a',b',c',d'}} & \phi_{R\mathbf{k}_1,a',\sigma'_1}(\mathbf{r}_1)\phi_{R\mathbf{k}_4,d',\sigma'_4}(\mathbf{r}_4)\phi^*_{R\mathbf{k}_2,b',\sigma'_2}(\mathbf{r}_2)\phi^*_{R\mathbf{k}_3,c',\sigma'_3}(\mathbf{r}_3) \\ & \times \sum_{a,b,c,d} \Big\{ \tilde{F}_{\substack{\mathbf{k}_1 a,\mathbf{k}_2 b \\ \mathbf{k}_3 c,\mathbf{k}_4 d}}(\omega,\omega',\omega'')\mathcal{D}_{\mathbf{k}_1,a'a}(g)\mathcal{D}^*_{\mathbf{k}_3,c'c}(g)\mathcal{D}^*_{\mathbf{k}_2,b'b}(g)\mathcal{D}_{\mathbf{k}_4,d'd}(g)\Big\}.\end{aligned} \tag{3.9}$$

If $\tilde{F}$ is invariant under the action of $g$, i.e $\tilde{F} = \tilde{F}'$ then from Eq. (3.9) we get

$$\begin{aligned}\tilde{F}_{\substack{R\mathbf{k}_1 a',R\mathbf{k}_2 b' \\ R\mathbf{k}_3 c',R\mathbf{k}_4 d'}}(\omega,\omega',\omega'') = \sum_{a,b,c,d} \Big\{ & \tilde{F}_{\substack{\mathbf{k}_1 a,\mathbf{k}_2 b \\ \mathbf{k}_3 c,\mathbf{k}_4 d}}(\omega,\omega',\omega'') \\ & \mathcal{D}_{\mathbf{k}_1,a'a}(g)\mathcal{D}^*_{\mathbf{k}_3,c'c}(g)\mathcal{D}^*_{\mathbf{k}_2,b'b}(g)\mathcal{D}_{\mathbf{k}_4,d'd}(g)\Big\}.\end{aligned} \tag{3.10}$$

[1] Due to time-translation symmetry, the number of independent frequency variables in the Fourier transform is reduced from four to three [105].

Equation (3.10) motivates us to define the matrices $\mathcal{U}(g)$ for all $g = \{R \mid \boldsymbol{\tau}\} \in \mathcal{G}$, given by

$$\underset{\mathbf{k}_1\mathbf{k}_2 a,b}{\mathcal{U}_{\mathbf{k}_1'\mathbf{k}_2' a',b'}}(g) = \mathcal{D}_{\mathbf{k}_1,a'a}(g)\mathcal{D}^*_{\mathbf{k}_2,b'b}(g)\delta_{R\mathbf{k}_1,\mathbf{k}_1'}\delta_{R\mathbf{k}_2,\mathbf{k}_2'}. \tag{3.11}$$

Similarly, in the case of time-reversal symmetry, the matrix $\mathcal{U}(\mathscr{T})$ is given by

$$\underset{\mathbf{k}_1\mathbf{k}_2 a,b}{\mathcal{U}_{\mathbf{k}_1'\mathbf{k}_2' a',b'}}(\mathscr{T}) = \mathcal{D}_{\mathbf{k}_1,a'a}(\mathscr{T})\mathcal{D}^*_{\mathbf{k}_2,b'b}(\mathscr{T})\delta_{-\mathbf{k}_1,\mathbf{k}_1'}\delta_{-\mathbf{k}_2,\mathbf{k}_2'}\hat{\mathscr{K}}, \tag{3.12}$$

where $\hat{\mathscr{K}}$ is the complex conjugation operator, which ensures the anti-unitary property of time-reversal symmetry.

This allows us to conveniently express Eq. (3.10) as $\mathcal{F} = \mathcal{U}\mathcal{F}\mathcal{U}^\dagger$, where $\mathcal{F}$ represents the matrix $\underset{\mathbf{k}_3 c,\mathbf{k}_4 d}{\tilde{F}_{\mathbf{k}_1 a,\mathbf{k}_2 b}}(\omega,\omega',\omega'')$. Here, we employ the closure property of the set of $\mathbf{k}$-points under space group operations. It is worthwhile to point out that if this closure property is not respected (for example, in some shifted $\mathbf{k}$-grids), the symmetry properties are destroyed, leading to erroneous results such as breaking of degeneracies (see, for example, Ref. [122]).

An important point to note is that since the $\mathcal{D}$ matrices are unitary, the $\mathcal{U}$ matrices are also unitary for spatial symmetries. To show this, let $n = \{\mathbf{k}_1, \mathbf{k}_2, a, b\}$ and consider the product $\mathcal{U}(g)\mathcal{U}(g)^\dagger$:

$$\begin{aligned}
\mathcal{U}(g)\mathcal{U}(g)^\dagger &= \sum_n \mathcal{U}_{n',n}(g)\mathcal{U}^*_{n'',n}(g) \\
&= \sum_{\mathbf{k_1},\mathbf{k_2},a,b} \mathcal{D}_{\mathbf{k}_1,a'a}(g)\mathcal{D}^*_{\mathbf{k}_2,b'b}(g)\delta_{R\mathbf{k}_1,\mathbf{k}_1'}\delta_{R\mathbf{k}_2,\mathbf{k}_2'}\mathcal{D}^*_{\mathbf{k}_1,a''a}(g)\mathcal{D}_{\mathbf{k}_2,b''b}(g)\delta_{R\mathbf{k}_1,\mathbf{k}_1''}\delta_{R\mathbf{k}_2,\mathbf{k}_2''} \\
&= \delta_{\mathbf{k}_2'',\mathbf{k}_2'}\delta_{\mathbf{k}_1'',\mathbf{k}_1'}\sum_{a,b}\mathcal{D}_{R^{-1}\mathbf{k}_1',a'a}(g)\mathcal{D}^*_{R^{-1}\mathbf{k}_2',b'b}(g)\mathcal{D}^*_{R^{-1}\mathbf{k}_1',a''a}(g)\mathcal{D}_{R^{-1}\mathbf{k}_2',b''b}(g) \\
&= \delta_{\mathbf{k}_2'',\mathbf{k}_2'}\delta_{\mathbf{k}_1'',\mathbf{k}_1'}\delta_{a'',a'}\delta_{b'',b'} = \delta_{n',n''}.
\end{aligned} \tag{3.13}$$

On the other hand, in the case of time-reversal symmetry, $\mathcal{U}$ is anti-unitary due to the presence of the complex conjugation operator.

A central result of this work is that the set of all matrices $\mathcal{U}(g)$ for $g \in \mathcal{G}$ constitutes a

unitary representation of the space group $\mathcal{G}$.

To prove that the set $\{\mathcal{U}(g)\}$ forms a linear representation of the space group, let $g_1 = \{R_1 \mid \boldsymbol{\tau}_1\}$ and $g_2 = \{R_2 \mid \boldsymbol{\tau}_2\}$ be two elements in $\mathcal{G}$. The product of these two elements is given by:

$$g_1 \cdot g_2 = \{R_1 R_2 \mid R_1 \boldsymbol{\tau}_2 + \boldsymbol{\tau}_1\}.$$

In order to show that the $\mathcal{U}(g)$ matrices form a linear representation of the space group, we need to show that it is a group homomorphism, i.e.,

$$\mathcal{U}(g_1)\mathcal{U}(g_1) = \mathcal{U}(g_1 \cdot g_2) \; \forall g_1, g_2 \in \mathcal{G} \tag{3.14}$$

To prove Eq. (3.14), we consider $\mathcal{U}(g_1)\mathcal{U}(g_2)$ and let $n = \{\mathbf{k_1}, \mathbf{k_2}, a, b\}$,

$$\begin{aligned}
(\mathcal{U}(g_1)\mathcal{U}(g_2))_{n',n''} &= \sum_n \mathcal{U}_{n',n}(g_1)\mathcal{U}_{n,n''}(g_2) \\
&= \sum_{\mathbf{k_1},\mathbf{k_2},a,b} \Big\{ \mathcal{D}_{\mathbf{k}_1,a'a}(g_1)\mathcal{D}^*_{\mathbf{k}_2,b'b}(g_1)\delta_{R_1\mathbf{k}_1,\mathbf{k}'_1}\delta_{R_1\mathbf{k}_2,\mathbf{k}'_2} \\
&\times \mathcal{D}_{\mathbf{k}''_1,aa''}(g_2)\mathcal{D}^*_{\mathbf{k}''_2,bb''}(g_2)\delta_{R_2\mathbf{k}''_1,\mathbf{k}_1}\delta_{R_2\mathbf{k}''_2,\mathbf{k}_2} \Big\} \\
&= \sum_{a,b} \Big\{ \mathcal{D}_{R_2\mathbf{k}''_1,a'a}(g_1)\mathcal{D}^*_{R_2\mathbf{k}''_2,b'b}(g_1)\mathcal{D}_{\mathbf{k}''_1,aa''}(g_2)\mathcal{D}^*_{\mathbf{k}''_2,bb''}(g_2)\delta_{R_1R_2\mathbf{k}''_1,\mathbf{k}'_1}\delta_{R_1R_2\mathbf{k}''_2,\mathbf{k}'_2} \Big\}
\end{aligned} \tag{3.15}$$

Now, consider the following product for the $\mathcal{D}$ matrices as given in Eq. (3.15)

$$\begin{aligned}
&\sum_a \mathcal{D}_{R_2\mathbf{k}''_1,a'a}(g_1)\mathcal{D}_{\mathbf{k}''_1,aa''}(g_2) \\
&= \sum_a \langle R_1R_2\mathbf{k}''_1, a'|U(g_1)|R_2\mathbf{k}''_1, a\rangle\langle R_2\mathbf{k}''_1, a|U(g_2)|\mathbf{k}''_1, a''\rangle \\
&= \langle R_1R_2\mathbf{k}''_1, a'|U(g_1)U(g_2)|\mathbf{k}''_1, a''\rangle \\
&= \langle R_1R_2\mathbf{k}''_1, a'|U(g_1 \cdot g_2)e^{i\phi(g_1,g_2)}|\mathbf{k}''_1, a''\rangle \\
&= e^{i\phi(g_1,g_2)}\mathcal{D}_{\mathbf{k}''_1,a'a''}(g_1 \cdot g_2)
\end{aligned} \tag{3.16}$$

where it is assumed that the set of $U(g)$ matrices forms a projective representation of the space group, i.e., $U(g_1)U(g_2) = e^{i\phi(g_1,g_2)}U(g_1 \cdot g_2)$. Substituing Eq. (3.16) in Eq. (3.15), we

obtain

$$\begin{aligned}(\mathcal{U}(g_1)\mathcal{U}(g_2))_{n',n''} &= \delta_{R_1R_2\mathbf{k}_1'',\mathbf{k}_1'}\delta_{R_1R_2\mathbf{k}_2'',\mathbf{k}_2'}e^{i\phi(g_1,g_2)}e^{-i\phi(g_1,g_2)} \\ &\times \mathcal{D}_{\mathbf{k}_1'',a'a''}(g_1\cdot g_2)\mathcal{D}^*_{\mathbf{k}_2'',b'b''}(g_1\cdot g_2) \\ &= \mathcal{U}_{n',n''}(g_1\cdot g_2)\end{aligned} \tag{3.17}$$

This implies that the set of $\mathcal{U}(g)\ \forall g\in\mathcal{G}$ forms a linear representation of the space group $\mathcal{G}$

An important consequence of Eq. (3.10) arises when considering the effect of pure lattice translations. If $g$ corresponds to a translation, i.e., $\mathbf{r}\to\mathbf{r}+\boldsymbol{\tau}$, which belongs to the translational subgroup $\mathcal{T}$, then

$$\mathcal{D}_{\mathbf{k},m,n}(g)=\delta_{m,n}e^{-i\mathbf{k}\cdot\boldsymbol{\tau}}. \tag{3.18}$$

Substituting into Eq. (3.10), we obtain that the matrix elements $\tilde{F}_{\substack{\mathbf{k}_1a,\mathbf{k}_2b\\ \mathbf{k}_3c,\mathbf{k}_4d}}(\omega,\omega',\omega'')$ are nonzero only if the following crystal momentum conservation condition is satisfied:

$$\mathbf{k}_3-\mathbf{k}_4=\mathbf{k}_1-\mathbf{k}_2+\mathbf{G}=\mathbf{Q}. \tag{3.19}$$

Eq. (3.19) implies that the matrix $\mathcal{F}$, along with the $\mathcal{U}$ matrices are block diagonal in the basis of one-particle Bloch states, with each block labeled by the crystal momentum $\mathbf{Q}$. This momentum corresponds to a one-dimensional representation of the subgroup $\mathcal{T}$ (analogous to the electronic Hamiltonian) and gives rise to the very well known concept of dispersion (such as exciton dispersion) [33]. This implies that the each block of $\mathcal{F}$ can be written as:

$$\mathcal{F}^{(\mathbf{Q})}=\tilde{F}^{(\mathbf{Q})}_{\substack{\mathbf{k}_1ab\\ \mathbf{k}_3cd}}(\omega,\omega',\omega'')=\tilde{F}_{\substack{\mathbf{k}_1a,\mathbf{k}_1-\mathbf{Q}b\\ \mathbf{k}_3c,\mathbf{k}_3-\mathbf{Q}d}}(\omega,\omega',\omega''). \tag{3.20}$$

Furthermore, from Eq .(3.10), block matrices $\mathcal{F}^{(\mathbf{Q})}$ and $\mathcal{F}^{(R\mathbf{Q})}$ are related by a similarity transformation i.e,

$$\mathcal{F}^{(R\mathbf{Q})}=\mathcal{U}^{(\mathbf{Q})}\mathcal{F}^{(\mathbf{Q})}(\mathcal{U}^{(\mathbf{Q})})^\dagger, \tag{3.21}$$

where the $\mathcal{U}^{(\mathbf{Q})}(g)$ matrices are defined as

$$\mathcal{U}^{(\mathbf{Q})} = \mathcal{U}^{(\mathbf{Q})}_{\substack{\mathbf{k}_1 ab \\ \mathbf{k}_3 cd}}(g) = \mathcal{U}_{\substack{\mathbf{k}_1, \mathbf{k}_1 - R\mathbf{Q}, ab \\ \mathbf{k}_3, \mathbf{k}_3 - \mathbf{Q}, cd}}(g). \tag{3.22}$$

If $g$ belongs to the little group of $\mathbf{q}$ i.e $R\mathbf{q} = \mathbf{q} + \mathbf{G}$, then we obtain

$$\mathcal{F}^{(\mathbf{Q})} = \mathcal{U}^{(\mathbf{Q})} \mathcal{F}^{(\mathbf{Q})} (\mathcal{U}^{(\mathbf{Q})})^{\dagger}. \tag{3.23}$$

Now, we apply the formalism developed above to the BSE. As written in Eq. (2.69) and Eq. (2.70), the BSE is given by [98, 97, 48, 1, 93]

$$\begin{aligned} L(1,2;3,4) = L_0(1,2;3,4) + \int d(5,6,7,8) \Big\{ & L_0(1,2;5,6) \\ & \times K(5,6;7,8) L(7,8;3,4) \Big\} \end{aligned} \tag{3.24}$$

and the electron-hole interaction kernel $K(5,6;7,8)$ is given by [105]

$$K(5,6;7,8) = iW(5,6)\delta(5,7)\delta(6,8) - iv(5,7)\delta(5,6)\delta(7,8). \tag{3.25}$$

From Eq. (2.67), by construction, the two-particle correlation function is invariant under space group operations. The BSE kernel is also invariant under, which can be shown as follows:

$$v(\mathbf{r}_1, \mathbf{r}_2) = \frac{1}{|\mathbf{r}_2 - \mathbf{r}_2|} \tag{3.26}$$

Now, if we apply a space group opearation $\mathbf{r}' = R\mathbf{r} + \boldsymbol{\tau}$

$$\begin{aligned} v(\mathbf{r}'_1, \mathbf{r}'_2) &= \frac{1}{|R\mathbf{r}_2 + \boldsymbol{\tau} - R\mathbf{r}_2 - \boldsymbol{\tau}|} \\ &= \frac{1}{|R(\mathbf{r}_2 - \mathbf{r}_2)|} = v(\mathbf{r}_1, \mathbf{r}_2) \end{aligned} \tag{3.27}$$

This implies that the bare exchange is invariant. Similarly, we can also show that the

screened Coulomb interaction is invariant:

$$W(\mathbf{r}_1, \mathbf{r}_2, \omega) = \int d^3\mathbf{r}''\, v(\mathbf{r}_1, \mathbf{r}'', \omega)\varepsilon^{-1}(\mathbf{r}'', \mathbf{r}_2, \omega), \tag{3.28}$$

The dielectric function is invariant under the crystal symmetry operation, i.e.,

$$\varepsilon^{-1}(\mathbf{r}'', \mathbf{r}_2, \omega) = \varepsilon^{-1}(R\mathbf{r}'' + \boldsymbol{\tau}, R\mathbf{r}_2 + \boldsymbol{\tau}, \omega).$$

This gives us

$$\begin{aligned} W(\mathbf{r}_1', \mathbf{r}_2', \omega) &= \int d^3\mathbf{r}''\, v(\mathbf{r}_1', \mathbf{r}'')\varepsilon^{-1}(\mathbf{r}'', \mathbf{r}_2', \omega) \\ &= \int d^3\mathbf{r}''\, v(\mathbf{r}_1, R^{-1}(\mathbf{r}'' - \boldsymbol{\tau}))\varepsilon^{-1}(R^{-1}(\mathbf{r}'' - \boldsymbol{\tau}), \mathbf{r}_2, \omega) \\ &= \int d^3\mathbf{r}''\, v(\mathbf{r}_1, \mathbf{r}'', \omega)\varepsilon^{-1}(\mathbf{r}'', \mathbf{r}_2, \omega) \\ &= W(\mathbf{r}_1, \mathbf{r}_2, \omega). \end{aligned} \tag{3.29}$$

Due to the invariance of the four-point functions $L(7,8;3,4)$ and $K(5,6;7,8)$ under space group operations, their Fourier transform in single-particle basis follows Eq. (3.10). This implies that the effective two-particle BSE in the frequency domain can be solved separately for each momentum transfer $\mathbf{Q}$ as shown in the previous chapter.

As given in Eq. (2.81) and Eq. (2.82), the BSE and the effective two-particle Hamiltonian for each momentum transfer $\mathbf{Q}$ are written as

$$\tilde{L}^{(\mathbf{Q})}_{\substack{\mathbf{k}_1 ab \\ \mathbf{k}_3 cd}}(\omega) = \frac{i(f_{\mathbf{k_3},c} - f_{\mathbf{k_3}-\mathbf{Q},d})}{\omega - \tilde{H}^{(\mathbf{Q})}_{\substack{\mathbf{k}_1 ab \\ \mathbf{k}_3 cd}}}, \tag{3.30}$$

with the two-particle exciton Hamiltonian given by

$$\mathcal{H}^{(\mathbf{Q})} = \tilde{H}^{(\mathbf{Q})}_{\substack{\mathbf{k}_1 ab \\ \mathbf{k}_3 cd}} = \delta_{a,c}\delta_{b,d}\delta_{\mathbf{k_1},\mathbf{k_3}}(\varepsilon_{\mathbf{k_3},c} - \varepsilon_{\mathbf{k_3}-\mathbf{Q},d}) + i(f_{\mathbf{k_3},c} - f_{\mathbf{k_3}-\mathbf{Q},d})\tilde{K}^{(\mathbf{Q})}_{\substack{\mathbf{k}_1 ab \\ \mathbf{k}_3 cd}}. \tag{3.31}$$

An important point to note is that, unlike the $\mathcal{L}^{\mathbf{Q}}$ and $\mathcal{K}^{\mathbf{Q}}$ matrices, the $\mathcal{H}^{(\mathbf{Q})}$ matrix does not follow the similarity transformation given in Eq. (3.21) due to the presence of the factor

$(f_{\mathbf{k_3},c} - f_{\mathbf{k_3}-\mathbf{Q},d})$ in Eq. (3.31). To obtain a similarity transformation analogous to Eq. (3.21) for the exciton Hamiltonian defined in Eq. (3.31), we use the block diagonal form of the BSE Hamiltonian as given in Eq. (2.83):

$$\mathcal{H}_{2p}^{(\mathbf{Q})} = \begin{pmatrix} R^{(\mathbf{Q})} & C^{(\mathbf{Q})} \\ -(C^{(\mathbf{Q})})^{\dagger} & -D^{(\mathbf{Q})} \end{pmatrix} \tag{3.32}$$

The band transitions $(c,d) \to (a,b)$ for the $R^{(\mathbf{Q})}$ block are $(\tilde{c},\tilde{v}) \to (\tilde{c}',\tilde{v}')$, for the $D^{(\mathbf{Q})}$ block the transitions are $(\tilde{v},\tilde{c}) \to (\tilde{v}',\tilde{c}')$, and for the $C^{(\mathbf{Q})}$ block the transitions are $(\tilde{c},\tilde{v}) \to (\tilde{v}',\tilde{c}')$.

Using Eq. (3.21) for the kernel matrix elements, we obtain

$$\mathcal{H}_{2p}^{(R\mathbf{Q})} = \mathscr{U}^{(\mathbf{Q})}(g)\mathcal{H}_{2p}^{(\mathbf{Q})}(\mathscr{U}^{(\mathbf{Q})}(g))^{\dagger}, \tag{3.33}$$

where $\mathscr{U}^{(\mathbf{Q})}(g)$ is defined as

$$\mathscr{U}^{(\mathbf{Q})}(g) = \begin{pmatrix} \mathcal{U}_1^{(\mathbf{Q})}(g) & 0 \\ 0 & \mathcal{U}_2^{(\mathbf{Q})}(g) \end{pmatrix}, \tag{3.34}$$

with $\mathcal{U}_1^{(\mathbf{Q})}(g)$ and $\mathcal{U}_2^{(\mathbf{Q})}(g)$ given in Eq. (3.22).

The band transitions $(c,d) \to (a,b)$ for the $\mathcal{U}_1^{(\mathbf{Q})}(g)$ block correspond to $(\tilde{c},\tilde{v}) \to (\tilde{c}',\tilde{v}')$, while for $\mathcal{U}_2^{(\mathbf{Q})}(g)$, they correspond to $(\tilde{v},\tilde{c}) \to (\tilde{v}',\tilde{c}')$.

Similarly, for time-reversal symmetry $\mathscr{T}$, Eq. (3.33) takes the following form:

$$\mathcal{H}_{2p}^{(-\mathbf{Q})} = \mathscr{U}^{(\mathbf{Q})}(\mathscr{T})\mathcal{H}_{2p}^{(\mathbf{Q})}(\mathscr{U}^{(\mathbf{Q})}(\mathscr{T}))^{\dagger}, \tag{3.35}$$

where the matrix $\mathscr{U}^{(\mathbf{Q})}(\mathscr{T})$ is given by

$$\mathscr{U}^{(\mathbf{Q})}(\mathscr{T}) = \begin{pmatrix} \mathcal{U}_1^{(\mathbf{Q})}(\mathscr{T}) & 0 \\ 0 & \mathcal{U}_2^{(\mathbf{Q})}(\mathscr{T}) \end{pmatrix}. \tag{3.36}$$

An important consequence of Eqs. (3.33) and (3.35) is that the action of a symmetry operation on an exciton wavefunction with momentum transfer $\mathbf{Q}$ yields an exciton wavefunc-

tion with momentum transfer $R\mathbf{Q}$ with the same eigenvalue. This can be explicitly written by considering an excitonic state with momentum transfer $\mathbf{Q}$, given by [97, 98, 1]:

$$\Psi_S^{\mathbf{Q}}(\mathbf{r}_e, \mathbf{r}_h) = \sum_{\mathbf{k}ij} A_{\mathbf{k},ij}^{S,(\mathbf{Q})}\ \phi_{\mathbf{k}i}(\mathbf{r}_e)\ \phi^*_{\mathbf{k}-\mathbf{Q},j}(\mathbf{r}_h), \tag{3.37}$$

where $A_{\mathbf{k},ij}^{S,(\mathbf{Q})}$ is the right eigenvector of the excitonic Hamiltonian $\mathcal{H}_{2p}^{(\mathbf{Q})}$ given in Eq. (3.32), and $\phi_{\mathbf{k}i}(\mathbf{r}_e)$ and $\phi^*_{\mathbf{k}-\mathbf{Q},j}(\mathbf{r}_h)$ are the Bloch states corresponding to the electron and hole, whose position coordinates are $\mathbf{r}_e$ and $\mathbf{r}_h$, respectively.

The action of a symmetry operator on $\Psi_S^{\mathbf{Q}}(\mathbf{r}_e, \mathbf{r}_h)$ is given by

$$\begin{aligned}\hat{U}(g)\Psi_S^{\mathbf{Q}}(\mathbf{r}_e, \mathbf{r}_h) = \sum_{\mathbf{k}ji i'j'\mathbf{k}'} \Big\{ &\mathscr{U}^{(\mathbf{Q})}_{\mathbf{k}'i'j',\mathbf{k}ij} A_{\mathbf{k},ij}^{S,(\mathbf{Q})} \\ &\times \phi_{\mathbf{k}'i'}(\mathbf{r}_e)\ \phi^*_{\mathbf{k}'-R\mathbf{Q},j'}(\mathbf{r}_h)\Big\}.\end{aligned} \tag{3.38}$$

Since $\hat{U}(g)\Psi_S^{\mathbf{Q}}(\mathbf{r}_e, \mathbf{r}_h)$ and $\Psi_S^{R\mathbf{Q}}(\mathbf{r}_e, \mathbf{r}_h)$ correspond to the same states, they must differ by a phase (or by a rotation matrix), given by

$$\hat{U}(g)\Psi_S^{\mathbf{Q}}(\mathbf{r}_e, \mathbf{r}_h) = \mathscr{D}_{\mathbf{Q},S'S}(g)\Psi_{S'}^{R\mathbf{Q}}(\mathbf{r}_e, \mathbf{r}_h), \tag{3.39}$$

where $\mathscr{D}_{\mathbf{Q},S'S}(g)$ is a rotation matrix which is block diagonal in degenerate space and is given by

$$\mathscr{D}_{\mathbf{Q},S'S}(g) = \sum_{\mathbf{k}ji i'j'\mathbf{k}'} \mathscr{U}^{(\mathbf{Q})}_{\mathbf{k}'i'j',\mathbf{k}ij} A_{\mathbf{k},ij}^{S,(\mathbf{Q})} (\tilde{A}^{,S'(R\mathbf{Q})}_{\mathbf{k}',i'j'})^*, \tag{3.40}$$

where $\tilde{A}^{S'(R\mathbf{Q})}$ are the left eigenvectors. In Eq. (3.40), we assume that the overlap matrix between the left and right eigenvectors is an identity matrix[2].

Since the BSE Hamiltonian is non-Hermitian, its eigenvectors are not mutually orthogonal, and consequently, its invariant subspaces may not be orthogonal either. However, within the Tamm-Dancoff approximation, the Hamiltonian becomes Hermitian, and the eigenvectors form an orthogonal set. Throughout the remainder of this thesis, we adopt the Tamm-

[2]We can always choose the left eigenvectors such that their overlap with the right eigenvectors yields the identity matrix.

Dancoff approximation, which enables the use of standard group-theoretical methods to derive selection rules.

If $g$ is in the little group of $\mathbf{Q}$, then $\mathscr{D}_{\mathbf{Q},S'S}(g)$ corresponds to a representation matrix of the excitonic states (including the non-unitary case, where the representation is non-unitary). In order to obtain the irreducible labels for the excitonic states, we decompose the little group $\mathcal{G}_{\mathbf{Q}}$ of $\mathbf{Q}$ into left cosets of the subgroup $\mathcal{T}$ in $\mathcal{G}_{\mathbf{Q}}$, i.e.,

$$\mathcal{G}_{\mathbf{Q}} \equiv \bigcup_{i=1}^{n_{\mathbf{Q}}} g_i^{\mathbf{Q}} \mathcal{T}, \tag{3.41}$$

where $g_i^{\mathbf{Q}}$ are the coset representatives, $g_i^{\mathbf{Q}}\mathcal{T}$ represents the cosets of $\mathcal{T}$ in $\mathcal{G}_{\mathbf{Q}}$, and $n_{\mathbf{Q}}$ is the index of $\mathcal{T}$ in $\mathcal{G}_{\mathbf{Q}}$. The quotient group $\mathcal{G}_{\mathbf{Q}}/\mathcal{T}$ is isomorphic to the point group $\mathcal{P}_{\mathbf{Q}}$ [29, 25].

The set of coset representatives $g_i^{\mathbf{Q}}$ is obtained by removing the lattice translational part (excluding fractional translations) from the little group symmetries $\mathcal{G}_{\mathbf{Q}}$. The set of coset representatives does not necessarily form a group, which allows for a slight redefinition of the representation matrices. The new, redefined exciton representation matrix for an element $g$ is given by

$$\bar{\mathscr{D}}_{\mathbf{Q}}(g) = \mathscr{D}_{\mathbf{Q}}(g) e^{i\mathbf{Q}\cdot\boldsymbol{\tau}}. \tag{3.42}$$

The new representation matrices are identical for elements within a given coset. The group multiplication rule for two elements $g_1 = \{R_1 \mid \boldsymbol{\tau}_1\}$ and $g_2 = \{R_2 \mid \boldsymbol{\tau}_2\}$ from two different cosets is given by

$$\bar{\mathscr{D}}_{\mathbf{Q}}(g_1)\bar{\mathscr{D}}_{\mathbf{Q}}(g_2) = \bar{\mathscr{D}}_{\mathbf{Q}}(g_1 \cdot g_2) e^{-i\mathbf{G}_0\cdot\boldsymbol{\tau}_2}, \tag{3.43}$$

where $\mathbf{G}_0 = R_1^{-1}\mathbf{Q} - \mathbf{Q}$ is reciprocal lattice vector. If $\mathbf{G}_0 = 0$, i.e., if there are no fractional translations in the little group $\mathcal{G}_{\mathbf{Q}}$, then $\bar{\mathscr{D}}_{\mathbf{Q}}$ corresponds to a linear representation. Otherwise, it corresponds to a projective representation of the point group $\mathcal{P}_{\mathbf{Q}}$. For demonstration purposes, we discuss only points where $\mathbf{G}_0 = 0$. i.e., symmorphic symmetries. Projective representations can be worked out using the procedure laid out in Ref. [29].

To obtain the irreducible representations of the excitonic states, we decompose $\bar{\mathscr{D}}_{\mathbf{Q}}$ into

the irreducible representations of the little point group $\mathcal{P}_{\mathbf{Q}}$, i.e.,

$$\bar{\mathscr{D}}_{\mathbf{Q}} = \bigoplus c_l \bar{\mathscr{D}}^l_{\mathbf{Q}}, \tag{3.44}$$

where $\bar{\mathscr{D}}^l_{\mathbf{Q}}$ corresponds to the $l^{\text{th}}$ irreducible representation of the point group, and $c_l$ is its multiplicity in the decomposition. We use the standard orthogonality relation [29, 25] for the characters to obtain $c_l$, which is given by

$$c_l = \frac{1}{|G|} \sum_{g \in G} \chi^{(l)}(g)^* \chi(g), \tag{3.45}$$

where $|G|$ is the order of the group, $\chi^{(l)}(g)$ is the character of the $l^{\text{th}}$ irreducible representation, and $\chi(g)$ is the trace of $\bar{\mathscr{D}}_{\mathbf{Q}}$.

## 3.3 Symmetries of excitons in LiF

Now, we demonstrate the application of the above methods to understand the symmetries of excitonic states in a widely studied material: LiF, which possesses $O_h$ point group symmetry and lacks non-symmorphic symmetries. This implies that we only need to work with linear representations at every $\mathbf{Q}$-point in the Brillouin zone.

We first assign irreducible representation labels to the excitonic states computed from *ab-initio* approaches by solving the BSE within the Tamm-Dancoff approximation and then reveal the underlying selection rules governing exciton-light interactions, as evidenced by their signatures in optical absorption spectroscopy.

In Fig. 3.2, we show the computed exciton dispersion of LiF. The longitudinal-transverse splitting at the $\Gamma$ point was turned off (this is done by setting the $\mathbf{G} = 0$ component of the bare exchange term to 0), as it breaks the degeneracies due to the presence of a long-range exchange interaction. As shown in the figure, each excitonic state at the high-symmetry points is labeled with the irreducible representations of the corresponding little group, computed using the method described above.

Along the $\Gamma \to X$ path, the lowering of point group symmetry causes the lowest triply

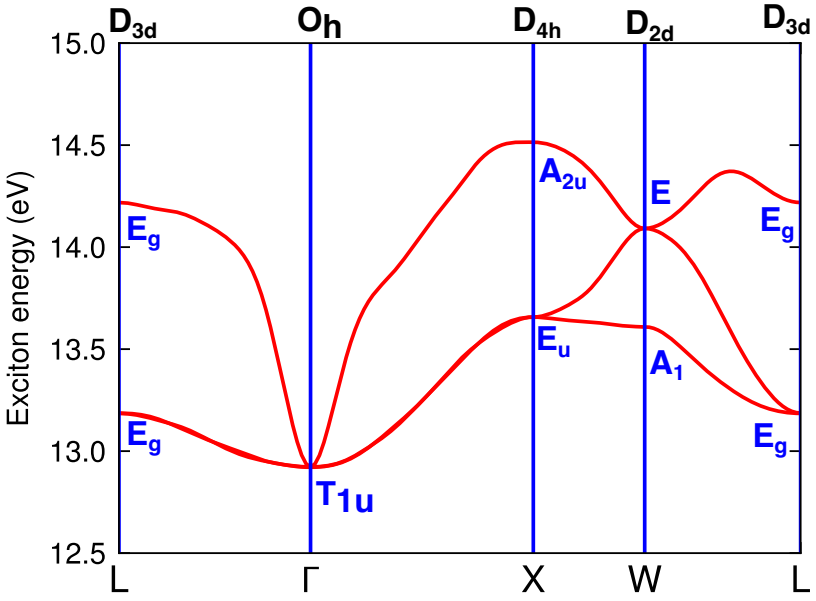


Figure 3.2: Exciton dispersion of LiF, computed using *ab initio* methods. Excitonic states at high-symmetry points are labeled with their corresponding irreducible representation labels.

degenerate exciton to split into singly and doubly degenerate modes. As we proceed along the $X \rightarrow W$ direction, further symmetry reduction leads to the additional splitting of the previously degenerate $E_u$ representation. Finally, along the $W \rightarrow L$ path, the degeneracy of the lowest two bands is lifted when moving away from the $W$ point, but they merge again at the $L$ point due to the higher point group symmetry present there.

Next, we focus our attention on the excitonic states at the $\Gamma$ point, as only they participate in the absorption of light by the material. In order to obtain the optical absorption spectrum, we calculate the imaginary part of the dielectric tensor, which is given by [98]

$$\varepsilon_2(\omega) = \frac{8\pi^2 e^2}{\omega^2} \sum_S \left| \langle 0 | \, \mathbf{e} \cdot \mathbf{r} \, | S \rangle \right|^2 \delta(\omega - E_S) \tag{3.46}$$

where $\mathbf{e}$ is the light polarization direction, $\mathbf{r}$ is the dipole operator, and $E_S$ are exciton energies.

In Fig. 3.3, we show the absorption spectrum of LiF, with red and blue vertical lines representing the bright and dark excitons, respectively. As seen in Eq. (3.46), absorption is

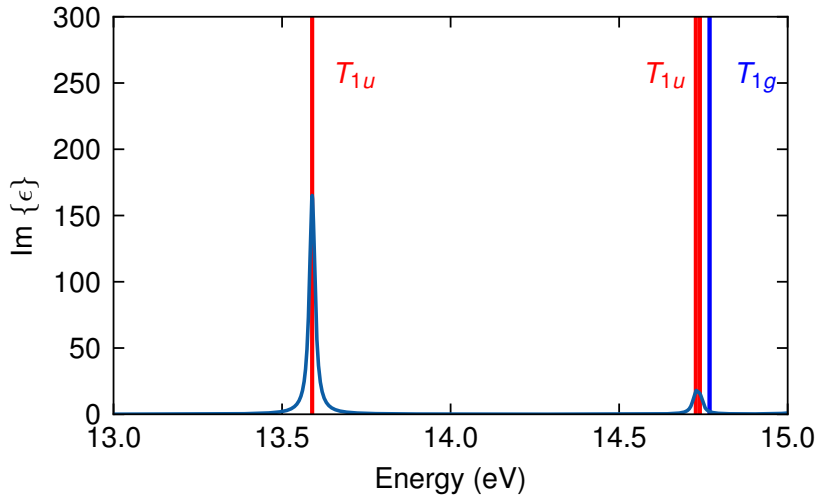


Figure 3.3: The absorption spectrum of LiF, computed using *ab initio* methods. The red and blue vertical lines indicate the positions of optically bright and dark excitons, respectively. The red and blue labels correspond to the irreducible representation labels for bright and dark excitons. The second vertical red line at higher energy appears broader than the first due to a slight breakdown of degeneracy among the excitons, introduced by numerical inaccuracies in the single-precision diagonalization solver. Using double precision and enforcing much stricter convergence criteria for the eigenvalues would reduce this error.

directly proportional to the absolute square of the dipole matrix elements. So excitons with finite exciton-photon matrix elements appear in the absorption spectrum.

As depicted in Fig. 3.3, the lowest bright excitons transform under the $T_{1u}$ representation. The first dark exciton transforms under the $T_{1g}$ representation. Both $T_{1u}$ and $T_{1g}$ excitons shown in Fig. 3.3 are triply degenerate. From the character table of the $O_h$ point group, we know that the dipole operators transform under the $T_{1u}$ representation. Therefore, excitons that transform under the $T_{1u}$ representation are optically active (bright), as manifested in the absorption spectrum.

Of course, one could perform a similar analysis on any other material without even plotting the excitonic wavefunctions. In the next chapter, we will apply our formalism to more complex systems, such as $h$BN, which possesses non-symmorphic symmetries, and monolayer $MoSe_2$, which exhibits strong spin-orbit coupling effects.

## 3.4 Application of Symmetries in Computational Aspects

Before concluding this chapter, we briefly discuss or highlight how one can improve the computation of the excitonic states using symmetries. Up to this point, we have focused on the formalism and its application to understand the symmetries of excitonic states. However, one of the most important uses of symmetry is its ability to greatly simplify the problem and reduce the computational cost of quantities that can be obtained by applying symmetry operations.

The first application of symmetry is to obtain the exciton wavefunctions across the entire Brillouin zone by applying symmetry operations to the wavefunctions computed in the irreducible part. In order to obtain the exciton wavefunction at a point $R\mathbf{Q}$ from $\mathbf{Q}$ using the symmetry $g = \{R \,|\boldsymbol{\tau}\}$, one can use Eq. (3.38) i.e :

$$A^{S,(R\mathbf{Q})}_{\mathbf{k},ij}(\mathbf{r}_e, \mathbf{r}_h) = \sum_{\mathbf{k}',i'j'} \mathscr{U}^{(\mathbf{Q})}_{\mathbf{k}'i'j',\mathbf{k}ij}(g) A^{S,(\mathbf{Q})}_{\mathbf{k}',i'j'}. \tag{3.47}$$

This completely avoids the need to construct the BSE kernel and diagonalize the two-particle BSE Hamiltonian at the $R\mathbf{Q}$ point, as the full wavefunction information can be ob-

tained through symmetry operations.

The second application is to construct the full BSE Hamiltonian by explicitly computing only a subset of the matrix elements, with the remainder obtained through symmetry operations. Suppose we want to construct a BSE Hamiltonian for a finite momentum transfer $\mathbf{Q}$. In this case, one could use the symmetries in the little group of $\mathbf{Q}$ to avoid computing matrix elements by using Eq. (3.33), which can significantly speed up the calculation. It is important to take into account the sparsity of the $\mathscr{U}(g)$ matrices rather than explicitly constructing them and performing brute-force full matrix multiplication.

Of course, one can do much more with symmetries. For example, the BSE Hamiltonian can be block-diagonalized by constructing symmetry-adapted bases using projection operators. This approach allows each block to correspond to an irreducible representation of the symmetry group, thereby significantly reducing the size of the matrix that needs to be diagonalized. However, a detailed implementation of this methodology is left for future work.

# Chapter 4

# Symmetries in Exciton-phonon interactions

In the previous chapter, we discussed the transformation properties of excitonic states under symmetry operations. In this chapter, we use the developed formalism to understand the selection rules governing exciton-phonon interactions. Moreover, we will see how these selection rules manifest beautifully in optical scattering experiments such as resonant Raman scattering and phonon-assisted luminescence. Additionally, we introduce the concept of total crystal angular momentum, which is analogous to crystal momentum, and present expressions for computing exciton-phonon matrix elements using symmetries. Parts of this chapter will be published in Ref. [79].

We start by writing the effective two-particle Bethe-Salpeter Hamiltonian for finite-momentum transfer within the Tamm-Dancoff approximation [22] as given by Eq. (2.84):

$$\mathcal{H}^{(\mathbf{Q})}_{v'c'\mathbf{k}',vc\mathbf{k}} = (\varepsilon_{c\mathbf{k}} - \varepsilon_{v\mathbf{k}-\mathbf{Q}})\delta_{v'c'\mathbf{k}',vc\mathbf{k}} + K^{(\mathbf{Q})}_{v'c'\mathbf{k}',vc\mathbf{k}}, \tag{4.1}$$

where$K^{(\mathbf{Q})}_{v'c'\mathbf{k}',vc\mathbf{k}}$ is the two-particle interaction kernel, and $c/c'$ denote conduction band indices, while $v/v'$ represent valence band indices. The terms $\varepsilon_{c\mathbf{k}}$ and $\varepsilon_{v\mathbf{k}-\mathbf{Q}}$ correspond to the single-particle energies of the Bloch states $\phi_{c\mathbf{k}}(\mathbf{r})$ and $\phi_{v\mathbf{k}-\mathbf{Q}}(\mathbf{r})$, respectively.

The exciton energies and eigenstates at a finite momentum transfer $\mathbf{Q}$ are obtained by

diagonalizing the BSE Hamiltonian in Eq. (4.1), which is written as

$$\sum_{vc\mathbf{k}} \mathcal{H}^{(\mathbf{Q})}_{v'c'\mathbf{k}',vc\mathbf{k}} A^{S,(\mathbf{Q})}_{vc\mathbf{k}} = \mathcal{E}^{(\mathbf{Q})}_{S} A^{S,(\mathbf{Q})}_{v'c'\mathbf{k}'}, \tag{4.2}$$

where $\mathcal{E}^{(\mathbf{Q})}_{S}$ are the exciton energies, and $A^{S,(\mathbf{Q})}_{vc\mathbf{k}}$ are their corresponding eigenvectors in the two-particle electron-hole basis [97, 98, 1].

Now consider a crystal symmetry operator $g = \{R \mid \mathbf{v}\}$, which transforms the coordinates as $\mathbf{r} \to R\mathbf{r} + \mathbf{v}$. If $g$ belongs to the little group $\mathcal{G}_{\mathbf{Q}}$ of $\mathbf{Q}$, i.e., $R\mathbf{Q} = \mathbf{Q} + \mathbf{G}$, where $\mathbf{G}$ is a lattice vector, then the representation matrix of the excitonic states, $\mathscr{D}_{\mathbf{Q}}(g)$, for the symmetry operation $g$, which is block diagonal in the degenerate subspace, is given by Eq. (3.40) and is written as:

$$\mathscr{D}_{\mathbf{Q},S'S}(g) = \sum_{\mathbf{k},cv,\mathbf{k}'c'v'} (A^{S',(\mathbf{Q})}_{\mathbf{k}',c'v'})^* \, \mathcal{U}^{(\mathbf{Q})}_{\mathbf{k}'c'v',\mathbf{k}cv}(g) \, A^{S,(\mathbf{Q})}_{\mathbf{k},cv}. \tag{4.3}$$

The unitary matrix $\mathcal{U}^{(\mathbf{Q})}(g)$ is given by [79]:

$$\mathcal{U}^{(\mathbf{Q})}_{\mathbf{k}'c'v',\mathbf{k}cv}(g) = \mathcal{D}_{\mathbf{k},c'c}(g) \, \mathcal{D}^{*}_{\mathbf{k}-\mathbf{Q},v'v}(g) \, \delta_{R\mathbf{k},\mathbf{k}'}. \tag{4.4}$$

Here, $\mathcal{D}_{\mathbf{k}}(g)$ represents the phase matrices, defined as in Eq. (3.5).

## 4.1 Total crystal angular momentum

Although, as shown in the previous chapter, one could derive selection rules from the irreducible representations of the little group, it is often more intuitive to consider quantum numbers analogous to total angular momentum. Due to the lack of continuous rotational symmetries in crystals or molecules, the conservation of angular momentum is no longer valid. This motivates us to define the total crystal angular momentum of an exciton or a phonon, analogous to the crystal momentum for translations.

If the little point group of $\mathbf{Q}$ contains an $n$-fold rotational symmetry along the rotational axis $\hat{\mathbf{n}}$ (in case of multiple rotations, we take the largest $n$), represented by $R_n(\hat{\mathbf{n}})$, the cor-

responding unitary matrix $U(R_n(\hat{\mathbf{n}}))$ can be expressed as

$$U(R_n(\hat{\mathbf{n}})) = \exp\left(-\frac{2\pi i J_{\hat{\mathbf{n}}}}{n}\right), \tag{4.5}$$

where $J_{\hat{\mathbf{n}}}$ is a Hermitian matrix, which we refer to as the *total crystal angular momentum* or *pseudo angular momentum* operator along the rotation axis $\hat{\mathbf{n}}$ [106].

Since the order of the $n$-fold rotation symmetry is $n$, i.e., $(R_n(\hat{\mathbf{n}}))^n = I$, where $I$ is the identity operation, this implies that the corresponding unitary matrix $U(R_n(\hat{\mathbf{n}}))$ possesses eigenvalues of the form $\exp\left(-\frac{2\pi i j}{n}\right)$. Furthermore, since $[U(R_n(\hat{\mathbf{n}})), \mathscr{H}^{(\mathbf{Q})}] = 0$, where $\mathscr{H}^{(\mathbf{Q})}$ represents either the dynamical matrix for the phonon wavevector $\mathbf{Q}$ or the excitonic Hamiltonian matrix for a transfer momentum $\mathbf{Q}$, it follows that $J_{\hat{\mathbf{n}}}$ and $\mathscr{H}^{(\mathbf{Q})}$ commute. Consequently, they are simultaneously diagonalizable. This allows us to assign a quantum number $j$ to each eigenstate of $\mathscr{H}^{(\mathbf{Q})}$, which we refer to as the total crystal angular momentum of the exciton or the phonon. It is important to emphasize that the total crystal angular momentum of the exciton or the phonon does not depend on the choice of basis or starting point. This is because the eigenvalues corresponding to irreducible representations remain invariant under similarity transformations, just like the character of a representation.

Now, consider a set $\{\Phi_{\mathbf{Q},S'}\}$ of degenerate eigenstates of $\mathscr{H}^{(\mathbf{Q})}$ that form an invariant subspace under the action of the symmetry elements of the little group $\mathcal{G}_{\mathbf{Q}}$. The action of the symmetry operation $\hat{U}(R_n(\hat{\mathbf{n}}))$ on an eigenstate from this set can be expressed as

$$\hat{U}(R_n(\hat{\mathbf{n}}))\Phi_{\mathbf{Q},S} = \sum_{S'=1}^{l} \Gamma_{S'S}\Phi_{\mathbf{Q},S'}, \tag{4.6}$$

where $\Gamma_{S'S}$ is the $l$-dimensional representation matrix corresponding to the phonon (given in Ref. [64]) or exciton (as defined in Eq. (3.42)) for the symmetry operation $R_n(\hat{\mathbf{n}})$.

If the basis $\{\Phi_{\mathbf{Q},S'}\}$ does not form a simultaneous eigenbasis of $\hat{U}(R_n(\hat{\mathbf{n}}))$ and $\mathscr{H}^{(\mathbf{Q})}$, then the representation matrix $\Gamma_{S'S}$ is not diagonal. To obtain a simultaneous eigenbasis, we diagonalize the unitary matrix $\Gamma_{S'S}$. The unitary matrix that diagonalizes $\Gamma_{S'S}$ transforms the basis $\{\Phi_{\mathbf{Q},S'}\}$ into a new set of eigenstates that simultaneously diagonalize both $J_{\hat{\mathbf{n}}}$ and $\mathscr{H}^{(\mathbf{Q})}$, with the corresponding eigenvalues given by $e^{-2\pi i j_n/n}$. The values $j_n \in$

$\{0, 1, \ldots, n-1\}$ represent the total crystal angular momentum quantum numbers for phonons or excitons. These quantum numbers are responsible for *"chiral"* behavior in excitons [50] and phonons [125], particularly in hexagonal materials, as will be demonstrated in the next section.

## 4.2 Chirality

Over the past few years, there has been significant interest in circularly polarized phonons, known as chiral phonons [125, 115]. Similarly, the first bright excitons in TMDCs have been shown to possess a form of chirality that selectively couples with left- and right-circularly polarized light [50, 112]. A natural question to ask is: where does this chirality come from?

To answer this, consider a hexagonal lattice that possesses a three-fold rotational symmetry in the little groups of the $\Gamma$ and $K^{(\prime)}$ points. This symmetry implies that the total crystal angular momentum for excitons or phonons can take values $\{-1, 0, 1\}$ (we use $-1$ instead of $2$, since the total crystal angular momentum is defined modulo $n$ for an $n$-fold rotation). Point groups with $C_3$ symmetry contain an $E$ representation, which can be single or double degenerate and carry a total crystal angular momentum of $\pm 1$. This implies that the simultaneous eigenstates of excitons or phonons that transform under $E$ modes will be chiral and will selectively couple with other quasiparticles.

The phonon eigenvectors which are also eigenstates of the $C_3$ rotation operator are known as *chiral phonons*, and the total crystal angular momentum is referred to as the "pseudo angular momentum" of phonons [125]. Similar to phonons, the first bright excitons in TMDCs carry a total crystal angular momentum of $\pm 1$, which causes them to selectively couple with left- or right-circularly polarized light. Due to spin-orbit coupling effects, these excitons become even more interesting; a more detailed discussion is provided in the next section. This total crystal angular momentum is sometimes also referred to as the valley index, chiral index, or pseudospin [112].

## 4.3 Exciton-phonon coupling

As discussed previously, the coupling of excitons with phonons plays an important role in optical scattering processes such as resonant Raman scattering (which will be discussed in the next section). One of the central ingredients required to compute physical properties involving exciton-phonon scattering is the exciton-phonon matrix element. These matrix elements are analogous to the electron-phonon matrix elements that are essential for studying phenomena involving electron-phonon interactions.

Unlike electron-phonon matrix elements, there are different definitions of exciton-phonon matrix elements found in the literature. For example, Ref. [17] defines them as the expectation value of the directional derivative of the BSE Hamiltonian along the phonon eigenvector, whereas Ref. [3] defines them as the expectation value of the Kohn-Sham deformation potential with respect to excitonic states. Although the definitions differ in form, they yield the same final expression. This is the same result obtained from a perturbative expansion of the matrix elements involved in Raman scattering [95].

The exciton phonon matrix elements within the TDA are given by

$$\begin{aligned} \mathcal{G}^{\lambda}_{S',S}(\mathbf{Q},\mathbf{q}) = &\sum_{\mathbf{k}cc'v} (A^{S',(\mathbf{Q}+\mathbf{q})}_{\mathbf{k}+\mathbf{q},c'v})^* A^{S,(\mathbf{Q})}_{\mathbf{k},cv} \tilde{g}^{\lambda}_{c',c}(\mathbf{k},\mathbf{q}) \\ &- \sum_{\mathbf{k}cvv'} (A^{S',(\mathbf{Q}+\mathbf{q})}_{\mathbf{k},cv'})^* A^{S,(\mathbf{Q})}_{\mathbf{k},cv} \tilde{g}^{\lambda}_{v,v'}(\mathbf{k}-\mathbf{Q}-\mathbf{q},\mathbf{q}). \end{aligned} \tag{4.7}$$

The electron-phonon matrix elements $\tilde{g}^{\lambda}_{c',c}(\mathbf{k},\mathbf{q})$ are given by

$$\tilde{g}^{\lambda}_{c',c}(\mathbf{k},\mathbf{q}) = \langle \mathbf{k}+\mathbf{q}, c' | \, \partial^{\lambda}_{\mathbf{q}} V \, | \mathbf{k}, c \rangle \,, \tag{4.8}$$

where $\partial^{\lambda}_{\mathbf{q}} V$ is the directional derivative of the total Kohn-Sham potential with respect to the phonon displacement vector of mode index $\lambda$ and momentum $\mathbf{q}$.

The exciton-phonon matrix element in Eq. (4.7) can be interpreted as the quantum mechanical sum of two independent processes: (i) the scattering of an electron from momentum $\mathbf{k}$ to $\mathbf{k}+\mathbf{q}$ via absorption of a phonon with momentum $\mathbf{q}$, while the hole remains at fixed

momentum $\mathbf{k}-\mathbf{Q}$; and (ii) the scattering of a hole from momentum $\mathbf{k}-\mathbf{Q}$ to $\mathbf{k}-\mathbf{Q}-\mathbf{q}$ via emission of a phonon with momentum $\mathbf{q}$, while the electron remains at fixed momentum $\mathbf{k}$.

### 4.3.1 Bra-Ket notation for exciton phonon matrix elements

In this subsection, we demonstrate how the exciton-phonon matrix elements defined in Eq. (4.7) can be written in compact Bra-Ket notation. This formulation will be useful later when deriving selection rules.

We consider the following matrix element within the Tamm-Dancoff approximation [22]:

$$\tilde{\mathcal{G}}^{\lambda}_{S',S}(\mathbf{Q},\mathbf{q}) \equiv \langle S', \mathbf{q}+\mathbf{Q} \,|\partial^{\lambda}_{\mathbf{q}} V|\, S, \mathbf{Q}\rangle \tag{4.9}$$

where $\mathbf{Q}$ is the transfer momentum of the initial exciton $S$, $\mathbf{q}$ is the momentum of the phonon with mode index $\lambda$ and deformation potential $\partial^{\lambda}_{\mathbf{q}} V$, and $\mathbf{Q}+\mathbf{q}$ is the transfer momentum of the outgoing exciton $S'$. The excitonic state $|S,\mathbf{Q}\rangle$ can be written as [97, 98, 1]:

$$|S,\mathbf{Q}\rangle = \sum_{\mathbf{k}cv} A^{S,Q}_{\mathbf{k},cv} a^{\dagger}_{\mathbf{k}c} a_{\mathbf{k}-\mathbf{Q}v} |0\rangle, \tag{4.10}$$

where $|0\rangle$ is the non-interacting ground state. Furthermore, the phonon deformation potential can be expressed in terms of one-particle Bloch states as

$$\begin{aligned} \partial^{\lambda}_{\mathbf{q}} V &= \sum_{m,n,\tilde{\mathbf{k}}} \langle m, \mathbf{q}+\tilde{\mathbf{k}} \,|\partial^{\lambda}_{\mathbf{q}} V|\, n, \tilde{\mathbf{k}}\rangle \; a^{\dagger}_{\mathbf{k}+\mathbf{q}m} a_{\mathbf{k}n} \\ &= \sum_{m,n,\tilde{\mathbf{k}}} a^{\dagger}_{\tilde{\mathbf{k}}+\mathbf{q}m} a_{\tilde{\mathbf{k}}n} \tilde{g}^{\lambda}_{m,n}(\tilde{\mathbf{k}},\mathbf{q}), \end{aligned} \tag{4.11}$$

where $\tilde{g}^{\lambda}_{m,n}(\tilde{\mathbf{k}},\mathbf{q})$ are the electron-phonon matrix elements. Substituting Eq. (4.10) and Eq. (4.11) into Eq. (4.9) gives

$$\begin{aligned} \tilde{\mathcal{G}}^{\lambda}_{S',S}(\mathbf{Q},\mathbf{q}) = \sum_{\mathbf{k}\mathbf{k}'\tilde{\mathbf{k}}cc'vv'mn} \Big\{ &(A^{S',(\mathbf{Q}+\mathbf{q})}_{\mathbf{k}',c'v'})^{*} A^{S,(\mathbf{Q})}_{\mathbf{k},cv} \tilde{g}^{\lambda}_{m,n}(\tilde{\mathbf{k}},\mathbf{q}) \\ &\times \langle 0| a^{\dagger}_{\mathbf{k}'-\mathbf{Q}-\mathbf{q}v'} a_{\mathbf{k}'c'} a^{\dagger}_{\tilde{\mathbf{k}}+\mathbf{q}m} a_{\tilde{\mathbf{k}}n} a^{\dagger}_{\mathbf{k}c} a_{\mathbf{k}-\mathbf{Q}v} |0\rangle \Big\}. \end{aligned} \tag{4.12}$$

Considering the correlation function in Eq. (4.12), and employing Wick's contractions gives

$$\begin{aligned}
&\langle 0|a^{\dagger}_{\mathbf{k}'-\mathbf{Q}-\mathbf{q}v'}a_{\mathbf{k}'c'}a^{\dagger}_{\tilde{\mathbf{k}}+\mathbf{q}m}a_{\tilde{\mathbf{k}}n}a^{\dagger}_{\mathbf{k}c}a_{\mathbf{k}-\mathbf{Q}v}|0\rangle \\
=&\Big\{ -\delta_{\mathbf{k}-\mathbf{Q},\tilde{\mathbf{k}}+\mathbf{q}}\delta_{v,m}\delta_{\mathbf{k}',\mathbf{k}}\delta_{c',c}\delta_{\tilde{\mathbf{k}},\mathbf{k}'-\mathbf{Q}-\mathbf{q}}\delta_{v',n} \\
&+\delta_{\mathbf{k}'-\mathbf{Q}-\mathbf{q},\mathbf{k}-\mathbf{Q}}\delta_{v',v}\delta_{\mathbf{k}',\tilde{\mathbf{k}}+\mathbf{q}}\delta_{c',m}\delta_{\tilde{\mathbf{k}},\mathbf{k}}\delta_{n,c} \\
&+\delta_{\mathbf{k}'-\mathbf{Q}-\mathbf{q},\mathbf{k}-\mathbf{Q}}\delta_{v',v}\delta_{\mathbf{k}',\mathbf{k}}\delta_{c',c}\delta_{\tilde{\mathbf{k}}+\mathbf{q},\tilde{\mathbf{k}}}\delta_{m,n}\Big\}.
\end{aligned} \tag{4.13}$$

Substituting Eq. (4.13) into Eq. (4.12), we obtain

$$\tilde{\mathcal{G}}^{\lambda}_{S',S}(\mathbf{Q},\mathbf{q}) = \mathcal{G}^{\lambda}_{S',S}(\mathbf{Q},\mathbf{q}) + \delta_{\mathbf{q},0}\delta_{S,S'}\sum_{m,\mathbf{k}}\tilde{g}^{\lambda}_{m,m}(\mathbf{k},\mathbf{q}=0), \tag{4.14}$$

where $\mathcal{G}^{\lambda}_{S',S}(\mathbf{Q},\mathbf{q})$ are the exciton-phonon matrix elements as defined in Eq. (4.7). The extra term in Eq. (4.14) corresponds to a disconnected diagram and is canceled when performing a perturbation expansion due to normalization (for example, see supplementary information of Ref. [95] in the case of resonant Raman matrix elements).

### 4.3.2 Rotation of electron-phonon matrix elements

As electron-phonon matrix elements are one of the central ingredients when computing exciton-phonon matrix elements, it would be beneficial to obtain them using symmetry relations without explicitly performing the computation of the bra-ket.

In this section, we demonstrate how electron-phonon matrix elements transform under symmetry operations. The action of the symmetry operator $\hat{U}(g)$ on the phonon deformation potential is given by [39, 64]

$$\hat{U}(g)\partial^{\lambda}_{\mathbf{q}}V_{\mathsf{scf}}(\mathbf{r})\hat{U}^{\dagger}(g) = \sum_{\lambda'}\Gamma_{\mathbf{q},\lambda'\lambda}(g)\partial^{\lambda'}_{R\mathbf{q}}V_{\mathsf{scf}}(\mathbf{r}), \tag{4.15}$$

where $g$ represents a spatial crystal symmetry operation or time-reversal symmetry. If $g$ is a spatial crystal symmetry operation, it corresponds to a coordinate transformation $\mathbf{r} \to R\mathbf{r}+\mathbf{v}$, with $R$ being an orthogonal matrix and $\mathbf{v}$ a translation vector.

The term $\Gamma_{\mathbf{q},\lambda'\lambda}(g)$ is the phase matrix (or representation matrix, if $g$ belongs to the little group of $\mathbf{q}$) for the phonon modes, analogous to the $\mathcal{D}$ matrices for Bloch states. It is unitary and block diagonal in degenerate subspaces when phonon eigenvectors are chosen to be orthogonal. When $g$ is a spatial symmetry, $\Gamma_{\mathbf{q},\lambda'\lambda}(g)$ is given by [64]

$$\begin{aligned}\Gamma_{\mathbf{q},\lambda'\lambda}(g) &= (\mathbf{d}^{\lambda'}_{R\mathbf{q}})^\dagger \hat{U}(g)\mathbf{d}^{\lambda}_{\mathbf{q}} \\ &= \sum_{\kappa,\beta,\tilde{\kappa},\alpha} e^{i\mathbf{q}\cdot(g^{-1}\boldsymbol{\tau}_{\tilde{\kappa}}-\boldsymbol{\tau}_\kappa)} R_{\alpha\beta} d^{\lambda}_{\mathbf{q},\kappa,\beta}(d^{\lambda'}_{R\mathbf{q},\tilde{\kappa},\alpha})^*.\end{aligned} \tag{4.16}$$

Here, $\mathbf{d}^{\lambda'}_{R\mathbf{q}}$ and $\mathbf{d}^{\lambda}_{\mathbf{q}}$ are the phonon eigenvectors for $\mathbf{q}$ and $R\mathbf{q}$ phonon crystal momenta. In the case of time-reversal symmetry, we have

$$\Gamma_{\mathbf{q},\lambda'\lambda}(g) = (\mathbf{d}^{\lambda'}_{-\mathbf{q}})^\dagger (\mathbf{d}^{\lambda}_{\mathbf{q}})^*. \tag{4.17}$$

If $R\mathbf{q} \neq \mathbf{q} + \mathbf{G}$, where $\mathbf{G}$ is a reciprocal lattice vector, and the phonon eigenvector at $R\mathbf{q}$ is obtained by applying the symmetry operation $g$ to the eigenvector at $\mathbf{q}$, then $\Gamma_{\mathbf{q}}(g)$ is an identity matrix.

It is important to note that the deformation potential is generally a $2\times2$ matrix in the spinor subspace. Therefore, the symmetry operators $\hat{U}(g)$ must include spin rotation matrices that account for transformations in the spinor subspace.

Now, consider the following electron-phonon matrix elements:

$$\tilde{g}^{\lambda'}_{m,n}(R\mathbf{k}, R\mathbf{q}) = \langle m, R\mathbf{q} + R\mathbf{k} \,|\big(\partial^{\lambda'}_{R\mathbf{q}} V \mid n, R\mathbf{k}\rangle\big), \tag{4.18}$$

where we use parentheses to distinguish the action of the operator on either the bra or the ket, also taking time-reversal symmetry into account.

From the definition of the phase matrices in Eq (3.5), and using their unitary property, we have:

$$
\begin{aligned}
|n, R\mathbf{k}\rangle &= \sum_{n'} \mathcal{D}^{*}_{\mathbf{k},nn'}(g)\hat{U}(g)\,|n', \mathbf{k}\rangle\,, \\
|m, R\mathbf{k}+R\mathbf{q}\rangle &= \sum_{m'} \mathcal{D}^{*}_{\mathbf{k}+\mathbf{q},mm'}(g)\hat{U}(g)\,|m', \mathbf{k}+\mathbf{q}\rangle\,.
\end{aligned}
\tag{4.19}
$$

Substituting Eq. (4.19) into Eq. (4.18), and using Eq. (4.15), we obtain:

$$
\begin{aligned}
\tilde{g}^{\lambda'}_{m,n}(R\mathbf{k}, R\mathbf{q}) = \sum_{m',n'} \Bigg\{ & \mathcal{D}_{\mathbf{k}+\mathbf{q},mm'}(g)\mathcal{D}^{*}_{\mathbf{k},nn'}(g) \\
& \left(\langle m', \mathbf{q}+\mathbf{k}\,|\hat{U}^{\dagger}(g)\right)\left(\Gamma^{*}_{\mathbf{q},\lambda'\lambda}(g)\hat{U}(g)\partial^{\lambda}_{\mathbf{q}}V_{\mathsf{scf}}(\mathbf{r})\hat{U}^{\dagger}(g)\hat{U}(g)|\; n', \mathbf{k}\rangle\right) \Bigg\}
\end{aligned}
\tag{4.20}
$$

If $g$ is a normal spatial symmetry, we have:

$$
\begin{aligned}
\tilde{g}^{\lambda'}_{m,n}(R\mathbf{k}, R\mathbf{q}) = \Big\{ & \sum_{m',n',\lambda'} \Gamma^{*}_{\mathbf{q},\lambda'\lambda}(g)\mathcal{D}_{\mathbf{k}+\mathbf{q},mm'}(g) \\
& \times \mathcal{D}^{*}_{\mathbf{k},nn'}(g)\tilde{g}^{\lambda}_{m',n'}(\mathbf{k}, \mathbf{q}) \Big\}.
\end{aligned}
\tag{4.21}
$$

In the case where $g$ is time-reversal symmetry which is anti-unitary, we need to conjugate $\tilde{g}^{\lambda}_{m',n'}(\mathbf{k}, \mathbf{q})$ due to the transfer of the action of the leftmost $\hat{U}^{\dagger}(g)$ from the bra to the ket in Eq. (4.20), i.e.,

$$
\begin{aligned}
\tilde{g}^{\lambda'}_{m,n}(-\mathbf{k}, -\mathbf{q}) = \Big\{ & \sum_{m',n',\lambda'} \Gamma_{\mathbf{q},\lambda'\lambda}(g)\mathcal{D}_{\mathbf{k}+\mathbf{q},mm'}(g) \\
& \times \mathcal{D}^{*}_{\mathbf{k},nn'}(g)(\tilde{g}^{\lambda}_{m',n'}(\mathbf{k}, \mathbf{q}))^{*} \Big\}.
\end{aligned}
\tag{4.22}
$$

From Eqs. (4.22) and (4.21), we can obtain the electron-phonon matrix elements for the $R\mathbf{q}$ phonon wavevectors without explicitly evaluating the bracket. Furthermore, when $g$ belongs to the little group of $\mathbf{q}$, we can also retrieve the $R\mathbf{k}$ matrix elements from the $\mathbf{k}$ matrix elements with the correct gauge consistency.

### 4.3.3 Rotation of exciton-phonon matrix elements

In this section, we show how exciton-phonon matrix elements transform within the Tamm-Dancoff approximation [22] using symmetries, in a manner similar to electron-phonon matrix

elements. Consider the following bracket:

$$\tilde{\mathcal{G}}^{\lambda'}_{m,n}(R\mathbf{Q}, R\mathbf{q}) = \langle m, R\mathbf{q} + R\mathbf{Q} \,|\big(\partial^{\lambda'}_{R\mathbf{q}} V \mid n, R\mathbf{Q}\rangle\big), \tag{4.23}$$

where $\tilde{\mathcal{G}}$ represents the exciton-phonon interaction matrix elements.

Similar to the phase matrices for Bloch states, the phase matrices for excitonic states under symmetry operations are written as:

$$\hat{U}\,|S, \mathbf{Q}\rangle = \mathscr{D}_{\mathbf{Q},S'S}(g)\,|S', R\mathbf{Q}\rangle\,, \tag{4.24}$$

where $\mathscr{D}_{\mathbf{Q},S'S}(g)$ is a unitary matrix when the excitonic states are chosen to be orthogonal. This implies that

$$\begin{aligned} |n, R\mathbf{Q}\rangle &= \sum_{n'} \mathscr{D}^*_{\mathbf{Q},nn'}(g)\hat{U}(g)\,|n', \mathbf{Q}\rangle\,, \\ |m, R\mathbf{Q} + R\mathbf{q}\rangle &= \sum_{m'} \mathscr{D}^*_{\mathbf{Q}+\mathbf{q},mm'}(g)\hat{U}(g)\,|m', \mathbf{Q} + \mathbf{q}\rangle\,. \end{aligned} \tag{4.25}$$

Following the procedure outlined for electron-phonon matrix elements in the previous section, we obtain the following transformation rules. If $g$ is a normal spatial symmetry, we have:

$$\begin{aligned} \tilde{\mathcal{G}}^{\lambda'}_{m,n}(R\mathbf{Q}, R\mathbf{q}) = \sum_{m',n',\lambda'} &\Gamma^*_{\mathbf{q},\lambda'\lambda}(g)\mathscr{D}_{\mathbf{Q}+\mathbf{q},mm'}(g) \\ &\times \mathscr{D}^*_{\mathbf{Q},nn'}(g)\tilde{\mathcal{G}}^{\lambda}_{m',n'}(\mathbf{Q}, \mathbf{q}). \end{aligned} \tag{4.26}$$

If $g$ corresponds to time-reversal symmetry, we obtain:

$$\begin{aligned} \tilde{\mathcal{G}}^{\lambda'}_{m,n}(-\mathbf{Q}, -\mathbf{q}) = \sum_{m',n',\lambda'} &\Gamma_{\mathbf{q},\lambda'\lambda}(g)\mathscr{D}_{\mathbf{Q}+\mathbf{q},mm'}(g) \\ &\times \mathscr{D}^*_{\mathbf{Q},nn'}(g)(\tilde{\mathcal{G}}^{\lambda}_{m',n'}(\mathbf{Q}, \mathbf{q}))^*. \end{aligned} \tag{4.27}$$

Substituting Eq. (4.14) into Eqs. (4.27) and (4.26), we obtain an identical relation for the exciton-phonon matrix elements, where $\tilde{\mathcal{G}}$ is replaced with $\mathcal{G}$.

From Eqs. (4.27) and (4.26), we conclude that the exciton-phonon matrix elements for $R\mathbf{q}$

phonon wavevectors can be determined without explicitly evaluating the bracket. Furthermore, when $g$ belongs to the little group of $\mathbf{q}$, we can also retrieve the $R\mathbf{Q}$ matrix elements from the $\mathbf{Q}$ matrix elements, with the correct gauge.

## 4.4 Conservation of total crystal angular momentum

In this section, we derive a conservation rule for the total crystal angular momentum, analogous to the conservation of the total angular momentum.

Suppose that there is an $n$-fold rotational symmetry along the rotational axis $\hat{\mathbf{n}}$ in both the little point groups of $\mathbf{Q}$ (exciton transfer momentum) and $\mathbf{q}$ (phonon momentum); then

$$\begin{aligned}\langle S', \mathbf{Q}+\mathbf{q}|\, \partial^{\nu}_{\mathbf{q}} V\, |S, \mathbf{Q}\rangle &= \langle S', \mathbf{Q}+\mathbf{q}|\, U^{\dagger}U\, \partial^{\nu}_{\mathbf{q}} V\, U^{\dagger}U\, |S, \mathbf{Q}\rangle \\ &= \langle S', \mathbf{Q}+\mathbf{q}|\, \partial^{\nu}_{\mathbf{q}} V\, |S, \mathbf{Q}\rangle\, e^{-i\frac{2\pi}{n}(j_S + j_\nu - j_{S'})}\end{aligned} \tag{4.28}$$

where $U$ is the unitary operator corresponding to the $n$-fold rotational symmetry, and $j_S$, $j_\nu$, and $j_{S'}$ are the total crystal angular momenta of the $S$ exciton, $\nu$ mode phonon, and $S'$ exciton, respectively. We assumed that we are in the simultaneous eigenbasis of the Hamiltonian (either phonon or exciton) and unitary matrix. If this is not the case, we transform to a new basis such that they become simultaneous eigenbases.

From (4.28), we see that the matrix element $\langle S', \mathbf{Q}+\mathbf{q}|\, \partial^{\nu}_{\mathbf{q}} V\, |S, \mathbf{Q}\rangle$ can be non-zero only if

$$j_S + j_\nu - j_{S'} = l\, n, \tag{4.29}$$

where $l$ is an integer. The disconnected term transforms similarly as the matrix elements $\langle S', \mathbf{Q}+\mathbf{q}|\, \partial^{\nu}_{\mathbf{q}} V\, |S, \mathbf{Q}\rangle$, which implies that the conservation rule in (4.29) is equally applicable to exciton-phonon matrix elements.

## 4.5 Resonant Raman scattering in $MoSe_2$

We now demonstrate the application of the above methods to understand the symmetries of excitonic states in two widely studied materials: monolayer $MoSe_2$ and bulk hexagonal boron nitride ($h$BN). In particular, we reveal the underlying selection rules governing exciton-photon and exciton-phonon interactions, as evidenced by their optical spectroscopic signatures.

First, we examine the zero-momentum excitonic states of monolayer $MoSe_2$, which belongs to the $D_{3h}$ point group. At the center of the Brillouin zone, the little group includes all the symmetries of the crystal point group. This implies that the zero-momentum excitonic states must transform under the representations of the crystal point group.

In Fig. 4.1a, we show the energies of the first few zero-momentum excitonic states, calculated using GW-BSE [53, 98] on top of density functional theory (DFT) calculations. The excitonic states are labeled with the irreducible representations of the point group, with bright and dark excitons represented in red and blue, respectively. The first exciton, which is doubly degenerate due to time-reversal symmetry, is spin-forbidden and optically dark for in-plane light polarization as it transforms under $A_1'' + A_2''$ representation. Since the out-of-plane dipole operator $\hat{z}$ transforms under the $A_2''$ representation, the first dark exciton can possesses a finite out-of-plane dipole moment and is therefore optically bright for out-of-plane light polarization. In contrast, dark excitons near $\sim$1.8 eV lack the $A_2''$ representation and, therefore, do not possess an in-plane or out-of-plane dipole moment. On the other hand, the first bright exciton, which is doubly degenerate and commonly referred to as the $A_{1s}$ exciton, transforms under the $E'$ irreducible representation. Since the in-plane dipole operators $\hat{x}$ and $\hat{y}$ transform under the $E'$ representation, the $A_{1s}$ exciton possesses a finite in-plane dipole moment, which makes it optically bright for in-plane light polarization.

One of the most intriguing properties of monolayer transition metal dichalcogenides (TMDCs) is their ability to selectively populate the electron and hole densities of the $A_{1s}$ exciton in the inequivalent $K$ valleys using left- or right-circularly polarized light. To understand this phenomenon, we analyze the total crystal angular momentum of the $A_{1s}$ exciton along the principal axis, which takes the values $j = \pm 1$. These $j$ values are obtained by diag-

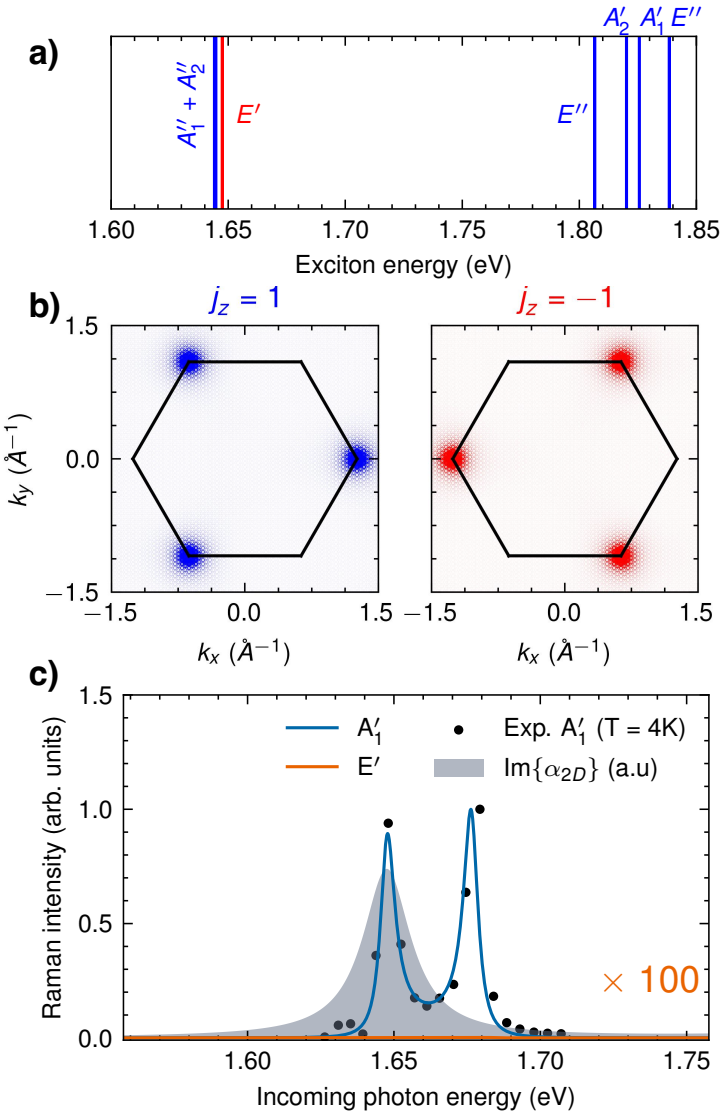


Figure 4.1: Excitons in monolayer $MoSe_2$. (a) Exciton energy spectrum at the $\Gamma$ point with corresponding irreducible representations. The blue/red vertical lines indicate the positions of dark/bright excitons, respectively. (b) Reciprocal space plot of the $A_{1s}$ exciton wavefunction in the simultaneous eigenstate of the total crystal angular momentum matrix and the exciton Hamiltonian. (c) Resonant Raman spectrum as a function of incoming photon energy. The $A_1'$ and $E'$ Raman modes are represented by blue and orange lines, respectively. The grey shading corresponds to the imaginary part of the 2D polarizability tensor, representing the absorption spectrum. The black dots denote experimental data for the $A_1'$ mode, taken from Ref. [70].

onalizing the two-dimensional representation matrix of the $A_{1s}$ exciton corresponding to the three-fold rotational symmetry of the crystal. The unitary matrix obtained from this diagonalization is then used to transform the energy eigenstates into the simultaneous eigenstates of the exciton Hamiltonian matrix and the total crystal angular momentum matrix along the principal axis.

Since circularly polarized light carries a total crystal angular momentum of $\pm 1$ along the out-of-plane direction [1], the simultaneous eigenstates of the $A_{1s}$ exciton selectively couple with left- or right-circularly polarized light upon absorption or emission, giving rise to the concept of chirality in excitons of monolayer TMDCs.

In Fig. 4.1b, we plot the phase-space map of the $A_{1s}$ exciton, defined as $A(\mathbf{k}) = \sum_{c,v} |A_{\mathbf{k}cv}|^2$, showing its simultaneous eigenstates along with the corresponding eigenvalue $j_z$ of the total crystal angular momentum operator along the principal axis. For each $j_z$, the $A_{1s}$ exciton is localized in its corresponding $K$ valley, thereby enabling the selective excitation of electron and hole densities in a specific valley using circularly polarized light.

The properties of the $A_{1s}$ exciton, such as its lifetime, are strongly influenced by exciton-phonon interactions [15]. These exciton-phonon interactions, in general, play an important role in optical-scattering processes such as resonant Raman scattering [95]. To understand the selection rules in these interactions, we look at phonon-mediated Stokes resonant Raman scattering in monolayer $MoSe_2$. Using the approach outlined in Refs. [94, 95], we compute the resonant Raman intensities at zero temperature within the Tamm-Dancoff approximation [22]. It is given by:

$$I^{\lambda} \propto \frac{\omega_{\mathrm{L}} - \omega_{\lambda}}{\omega_{\mathrm{L}}} \Big| \sum_{S,S'} \frac{\left(d^{\nu}_{S'}\right)^* \left(\mathcal{G}^{\lambda}_{SS'}\right)^* d^{\mu}_{S}}{\left(\hbar\omega_{\mathrm{L}} - E_S + i\gamma\right)\left(\hbar\omega_{\mathrm{L}} - \hbar\omega_{\lambda} - E_{S'} + i\gamma\right)} + \sum_{S,S'} \frac{\left(d^{\mu}_{S}\right)^* \mathcal{G}^{\lambda}_{SS'} d^{\nu}_{S'}}{\left(\hbar\omega_{\mathrm{L}} + E_S - i\gamma\right)\left(\hbar\omega_{\mathrm{L}} - \hbar\omega_{\lambda} + E_{S'} - i\gamma\right)} \Big|^2 . \tag{4.30}$$

[1] Applying an $n$-fold rotation operator to left- and right-circularly polarized light vectors, $\frac{1}{\sqrt{2}} \begin{bmatrix} 1 \\ \pm i \end{bmatrix}$, results in $e^{-i(\pm)\frac{1}{\sqrt{2}}} \begin{bmatrix} 1 \\ \pm i \end{bmatrix}$, implying that the total crystal angular momentum is $\pm 1$.

Here, $\mu/\nu$ indicate the polarizations of the incident and scattered light, $\omega_{\mathrm{L}}$ is the energy of the incoming photon, and $\omega_\lambda$ is the phonon frequency of mode $\lambda$. The sums run over excitonic states $S(S')$ with energies $E_{S(S')}$. The peak width is given by an empirical decay constant $\gamma$. The term $d_S^\mu$ represents the exciton-dipole matrix element along polarization $\mu$ for photon absorption, while $(\mathcal{G}^\lambda_{SS'})^*$ denotes the exciton-phonon coupling matrix element for exciton $S$ scattering into $S'$ via phonon emission of mode $\lambda$ [95] (see Eq. (4.7) for the expression of exciton-phonon matrix elements).

In Fig. 4.1c, we show the calculated resonant Raman intensities (solid lines) for the $A_1'$ and $E'$ Raman modes of monolayer $MoSe_2$ as a function of the incoming photon energy near the $A_{1s}$ exciton energy. The black dots correspond to the experimental Raman intensities of $A_1'$ measured at $T = 4$ K, taken from Ref. [70]. The grey shading represents the imaginary part of the in-plane polarizability tensor (absorption spectrum). The most striking observation is that the intensities of the $A_1'$ mode are orders of magnitude higher than the $E'$ mode. In order to understand this observation, we look at the underlying selection rules.

From Eq. (4.30), we can notice that only excitons that have finite $d_S^{\mu/\nu}$, i.e., bright excitons, participate in one-phonon resonant Raman scattering. This implies that near the optical gap of monolayer $MoSe_2$, only the $A_{1s}$ excitons are responsible for the majority of the resonant Raman scattering.

The $A_1'$ and $E'$ phonon modes possess total crystal angular momentum of $0$ and $\pm 1$ along the principal axis, respectively. Similar to the excitons, these $j$ values give rise to the concept of chirality for these phonons. Since $A_{1s}$ excitons possess $\pm 1$ total crystal angular momentum, we can use the conservation of total crystal momentum, which is given by

$$j_{S'} = j_S + j_\lambda + 3l \tag{4.31}$$

where $j_{S'}$, $j_S$, and $j_\lambda$ represent the total crystal angular momenta of the scattered exciton, incoming exciton, and phonon, respectively, and $l$ is an integer.

Clearly, from Eq. (4.31) and with the knowledge of total crystal angular momentum, we see that the $A_1'$ modes do not change the total crystal angular momentum of excitons, but

the $E'$ modes change it by $\pm 1$. This implies that the $A_1'$ mode allows only for intra-valley scattering of the $A_{1s}$ exciton, while the $E'$ mode allows inter-valley scattering. However, the intervalley scattering is largely forbidden due to spin conservation rules for electrons and holes and the very minimal overlap of excitonic states localized at $K/K'$, as seen in Fig. 4.1c. This implies that the $E'$ mode has much less intensity than the $A_1'$ mode, as seen in Fig. 4.1c. It should be noted that our analysis is more rigorous than the hand-waving argument presented in the previous work [95, 73], which relied on the conservation of the angular momentum based on the roughly circularly symmetric band structure near the $K/K'$ points.

## 4.6 Phonon assisted luminescence in $h$BN

Next, we examine the selection rules in absorption and phonon-assisted luminescence of bulk $h$BN, which possesses a $D_{6h}$ point group. In Fig. 4.2a, we present the absorption spectrum of $h$BN, where the vertical red and blue lines indicate the positions of in-plane bright and in-plane dark excitons, respectively. The in-plane and out-of-plane dipoles transform under the $E_{1u}$ and $A_{2u}$ representations of the $D_{6h}$ point group, respectively. In $h$BN, the first exciton is dark as it transforms under the $E_{2g}$ representation, whereas the second exciton is an in-plane bright exciton which transforms under the $E_{1u}$ representation. The first out-of-plane dipole-active exciton appears around $6.5$ eV and exhibits very weak dipole strength along the out-of-plane direction.

When moving away from the $\Gamma$ point, the symmetry of the system is reduced. As illustrated in Figs. 4.2b and c, the symmetry point group along the high-symmetry path $\Gamma - K$ is reduced to $C_{2v}$. One of the defining symmetries of this $C_{2v}$ group is the horizontal mirror symmetry of $h$BN. In the exciton dispersion, we observe that the $E_{2g}$ mode splits into $A_1$ and $B_1$ representations, both of which are even under horizontal mirror symmetry. Similarly, in the case of phonons, the out-of-plane modes (ZA/ZO), marked in green, are odd under horizontal mirror symmetry, while the in-plane modes (LA/TA or TO/LO) are even under horizontal mirror symmetry.

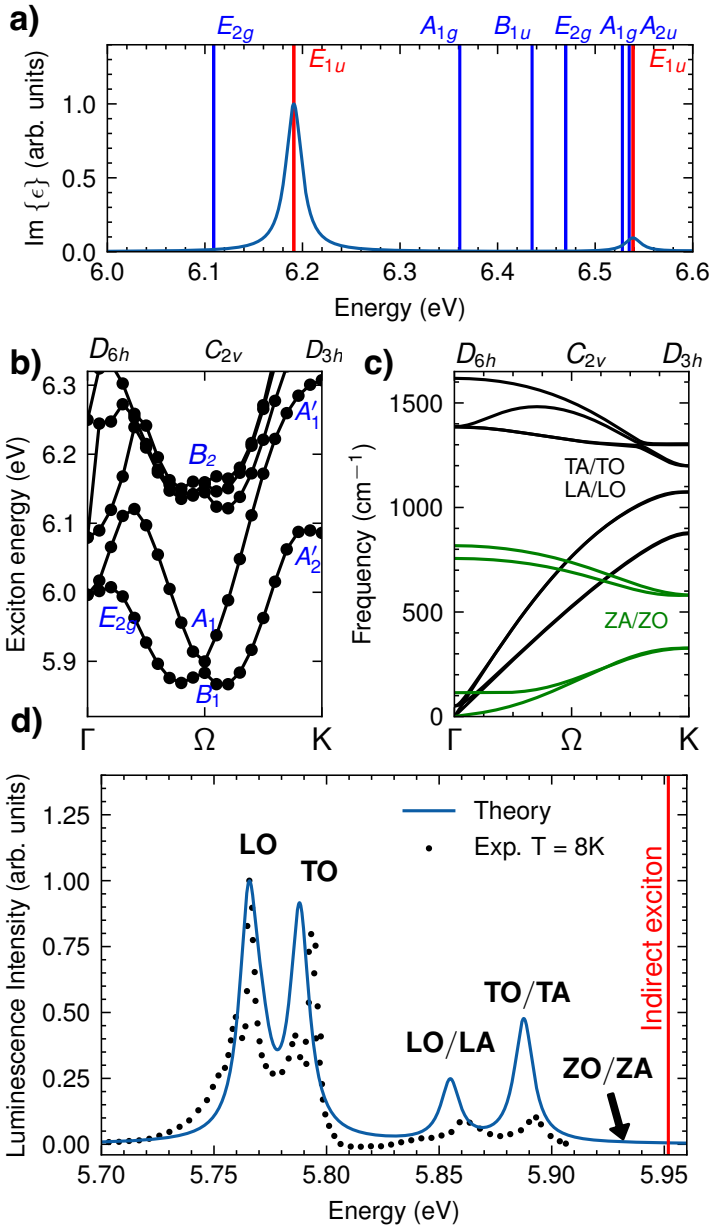


Figure 4.2: Excitons in bulk $h$BN. (a) Optical absorption spectrum of $h$BN. Blue/red vertical lines represent the positions of in-plane dark/bright excitons with their corresponding irreducible representations. (b) Exciton dispersion of the two lowest excitons of bulk $h$BN. The labels correspond to the irreducible representations at the high-symmetry points. (c) Phonon dispersion of bulk $h$BN. The green lines correspond to out-of-plane modes, which are odd under horizontal mirror symmetry. (d) Experimental (dots, taken from Ref. [111]) and computed (solid blue line) phonon-assisted luminescence spectrum of $h$BN.

One can also see the symmetries of excitons by visualizing their wavefunctions in real space by fixing the position of either the hole or the electron. Typically, a single hole is fixed at a position where the hole density is expected to be finite. For example, in the case of the lowest excitons in $h$BN, a reasonable choice is to place the hole slightly above the nitrogen atom, as the hole state is primarily composed of nitrogen $p_z$ orbitals [32]. However, this placement breaks the horizontal mirror symmetry, since applying the horizontal mirror operation would not map the hole back to the same position.

To restore mirror symmetry, we consider two hole positions [84]: one slightly above and the other slightly below the nitrogen atom. These two positions are mirror images of each other with respect to the horizontal mirror plane passing through the $h$BN layer. Once the two holes are fixed, we define the following antisymmetrized wavefunction:

$$\tilde{\Psi}(\mathbf{r}) = \Psi(\mathbf{r}, z + z_p) - \Psi(\mathbf{r}, z - z_p), \tag{4.32}$$

where $\Psi(\mathbf{r}, z \pm z_p)$ is the excitonic wavefunction with the hole fixed at a vertical distance $z_p$ above or below the horizontal mirror plane at $z$, and $\mathbf{r}$ is the electron position. We take the difference between the excitonic wavefunctions at the two hole positions to account for the fact that nitrogen $p_z$ orbitals are odd under horizontal mirror symmetry; a symmetric construction would otherwise lead to an almost complete cancellation of the total wavefunction. From Eq. (4.32), we see that the constructed function $\tilde{\Psi}(\mathbf{r})$ is symmetric for antisymmetric excitons and antisymmetric for symmetric excitons with respect to the horizontal mirror plane.

We then define the electronic density for these excitons as:

$$\rho^{\text{exc}}(\mathbf{r}) = \text{sgn}(\text{Real}\{\tilde{\Psi}(\mathbf{r})\}) \cdot |\tilde{\Psi}(\mathbf{r})|^2, \tag{4.33}$$

where sgn denotes the sign function. The sign function is included to capture the phase information of the wavefunction $\tilde{\Psi}(\mathbf{r})$.

In Fig. 4.3(a,b) and Fig. 4.4(a-c), we plot the electronic density of the exciton as defined in Eq. (4.33), by fixing two holes near a nitrogen atom, indicated by two black circles. In

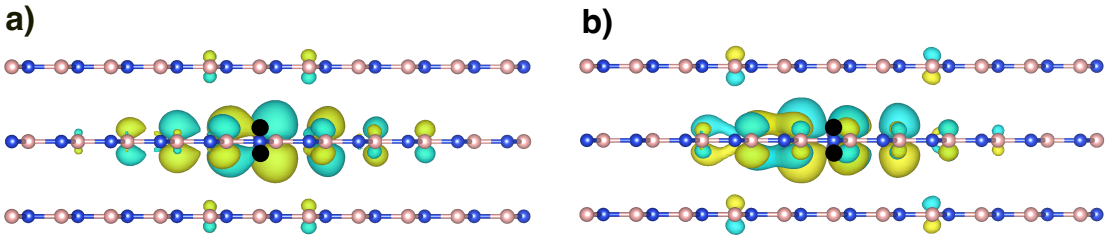


Figure 4.3: Electronic density of excitons, as given in Eq. (4.33), at the $\Gamma$ point $(0,0,0)$ for the first two in-plane bright excitons, which are degenerate and symmetric with respect to the horizontal mirror plane. The hole is fixed near a nitrogen atom.

Fig. 4.3, we present the two lowest in-plane bright excitons at the $\Gamma$ point that transform under the $E_{1u}$ irreducible representation. Additionally, in Fig. 4.4(a, b), we show the exciton wavefunctions at the $\Omega = \left(\frac{1}{6}, \frac{1}{6}, 0\right)$ point for the two lowest excitons, which transform under $B_1$ and $A_1$ representations, respectively. These excitons are symmetric with respect to the horizontal mirror plane of the hBN layer. On the other hand, in Fig. 4.4(c), we plot the lowest antisymmetric exciton at $\Omega$ with respect to the horizontal mirror plane, which transforms under the $B_2$ representation.

At the $\Gamma$ point, the bright excitons are symmetric with respect to the horizontal mirror plane, leading to antisymmetric electron densities as shown in Fig. 4.3(a,b). It is important to note that to obtain the fully symmetric excitonic wavefunction [122], one must perform an average over the degenerate states. However, for bright excitons, the representation matrix for the horizontal mirror symmetry is the identity, so the antisymmetry of the electron density for the bright excitons is preserved regardless of whether such averaging is performed.

Similarly, for the lowest excitons at the $\Omega$ point, we observe antisymmetric electron densities, consistent with symmetric exciton wavefunctions. The most intriguing case is the antisymmetric exciton shown in Fig. 4.4(c). The absence of electron density in the layer closest to the fixed holes is a consequence of symmetry: since boron $p_z$ orbitals are antisymmetric, any electron density in the nearby layer would render the overall exciton wavefunction symmetric. Thus, symmetry forbids such density near the hole, as both observed and expected

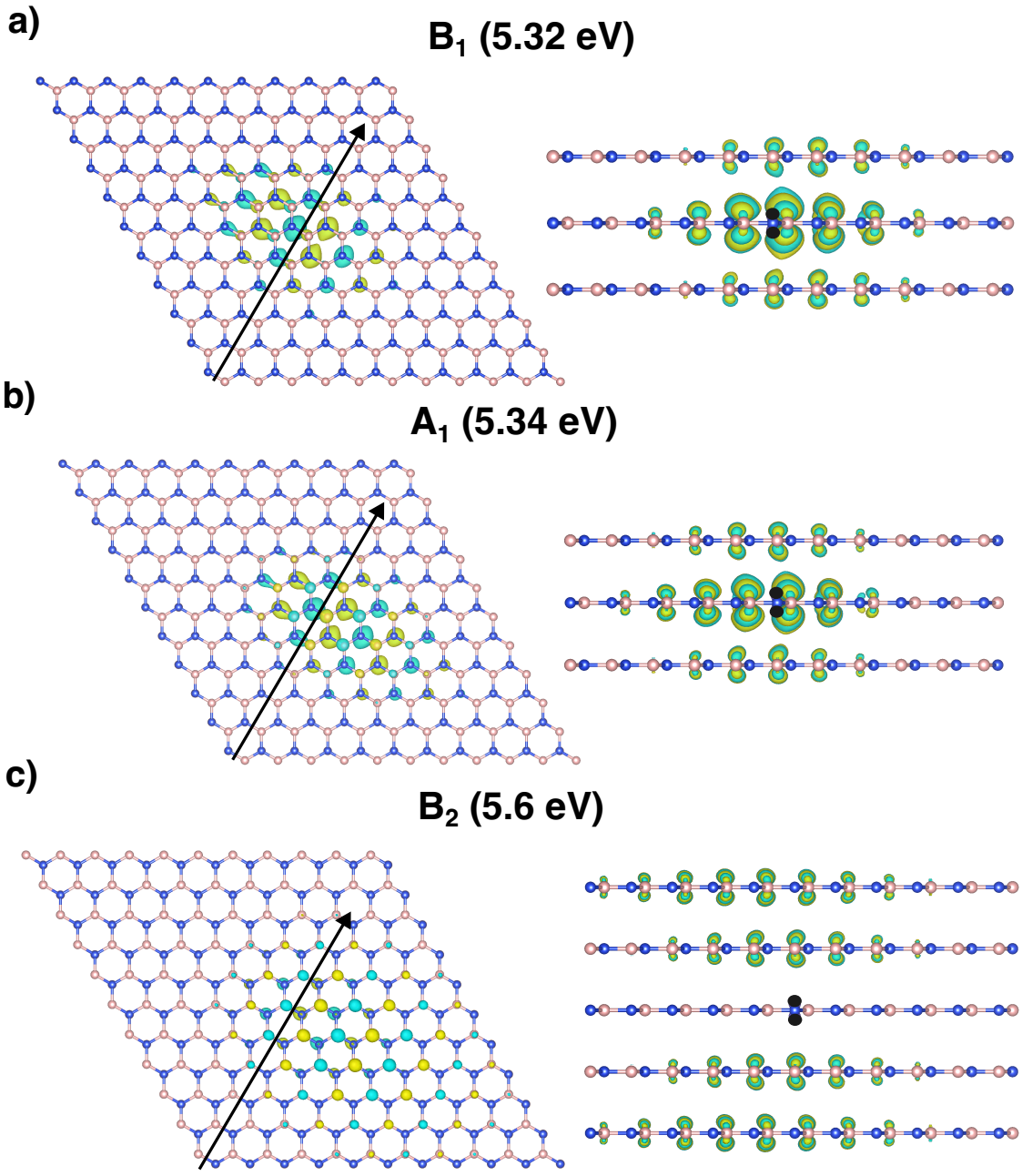


Figure 4.4: Electronic density of excitons, as given in Eq. (4.33), at $\Omega = \left(\frac{1}{6}, \frac{1}{6}, 0\right)$: panels (a) and (b) show the two lowest-energy excitons, which are symmetric with respect to the horizontal mirror plane; panel (c) shows the first antisymmetric exciton with respect to the horizontal mirror plane. The hole is fixed near a nitrogen atom, indicated by the black circle, and the arrow denotes the direction of the $\Omega$ point.

from our analysis.

The presence of horizontal mirror symmetry at the $\Omega$ point directly impacts the selection rules of the exciton-phonon matrix elements, which are evident in the phonon-assisted luminescence of $h$BN. To compute phonon-assisted luminescence, we follow the method in Ref. [124], where the intensity is expressed as

$$I \propto \sum_{S,\mathbf{Q},\lambda,\mu} \Big\{ \frac{e^{-\frac{(E_S^{\mathbf{Q}}-E_m)}{k_B T}}(1+n_{\lambda,\mathbf{Q}})\delta(\omega_L - E_S^{\mathbf{Q}} + \hbar\omega_{\lambda,\mathbf{Q}})}{(E_S^{\mathbf{Q}} - \hbar\omega_{\lambda,\mathbf{Q}})} \Big| \sum_{S'} \frac{(d^{\mu}_{S'}\mathcal{G}^{\lambda}_{SS'}(\mathbf{0},\mathbf{Q}))^*}{E_{S'} - E_S^{\mathbf{Q}} + \hbar\omega_{\lambda,\mathbf{Q}}} \Big|^2 \Big\}, \tag{4.34}$$

where $E_m$ is the lowest exciton energy, $T$ is the exciton temperature, $k_B$ is the Boltzmann constant, $E_S^{\mathbf{Q}}$ represents the exciton energy at $\mathbf{Q}$, $n_{\lambda,\mathbf{Q}}$ is the Bose factor for a phonon of mode $\lambda$ with momentum $\mathbf{Q}$, and the remaining indices are consistent with those used in Eq. (4.30). The exciton-phonon matrix elements are given in Eq. (4.7).

Eq. (4.34) captures the indirect emission process mediated by phonons, where an exciton $S$ at finite momentum $\mathbf{Q}$ scatters to the bright exciton $S'$ via emission of a phonon of mode index $\lambda$. The prefactor includes a Boltzmann factor $\exp[-(E_S^{\mathbf{Q}} - E_m)/k_B T]$ accounting for the exciton population at temperature $T$, and a Bose factor $1 + n_{\lambda,\mathbf{Q}}$ for the population of the emitted phonon. The delta function enforces energy conservation between the laser frequency $\omega_L$, the exciton energy, and the emitted phonon energy.

In Fig. 4.2d, we present the experimental and computed phonon-assisted luminescence spectrum of $h$BN. The dominant phonons contributing to the transition matrix element in Eq. (4.34) are located near the midpoint between $\Gamma$ and $K$. This is due to the presence of the Boltzmann factor in Eq. (4.34), which exponentially suppresses the matrix elements as one moves away from the minimum exciton energy $E_m$. As seen in Fig. 4.2b, the exciton minimum occurs near the midpoint of $\Gamma$ and $K$. Therefore, the majority of the phonons involved in the luminescence process of $h$BN originate from regions close to mid point of $\Gamma$ and $K$.

Furthermore, in Fig. 4.2d, we observe that only in-plane phonon modes contribute to the luminescence spectrum of $h$BN. Although some previous works have successfully reproduced the luminescence spectrum of $h$BN [85, 124], the underlying selection rules are

not well understood. Moreover, in all of these works, the symmetries were neglected during the calculations, resulting in slower computations with larger storage requirements. On the other hand, works such as Ref. [60], which attempted to use symmetries in their calculations, fail to account for the correct selection rules due to phase issues when computing the exciton-phonon matrix elements. The results presented in this thesis were obtained without breaking any symmetries, while also correctly reproducing the luminescence spectrum.

Now, with knowledge of the symmetries of the excitons, we can now understand the selection rules that govern the phonon-assisted luminescence process. Similar to the Raman case, Eq. (4.34) indicates that the outgoing excitons (denoted by the $S'$ index in Eq. (4.34)) must be bright excitons to have a finite contribution to the scattering matrix element. Due to the presence of the Boltzmann factor, only the lowest-energy states significantly participate in the luminescence process. Since both the initial and final excitonic states (we only consider the first in-plane dipole-active excitonic states, as the out-of-plane dipole is very weak) are even under horizontal mirror symmetry, the exciton-phonon matrix elements are finite only when the phonon modes are also even under this symmetry operation. As a result, out-of-plane phonon modes do not couple to the lowest-energy excitonic scattering states, leading to their absence or very low intensity in the luminescence spectrum, as shown in Fig. 4.2d. In contrast, the in-plane phonon modes are even under horizontal mirror symmetry and therefore contribute to the luminescence.

# Chapter 5

# Interlayer exciton-phonon coupling

In the previous chapter, we looked at the intralayer exciton-phonon coupling, where both the excitons and phonons originate from the same layer or material. In this chapter, we focus on interlayer exciton-phonon coupling, which occurs when an exciton in one layer couples with phonons from another layer.

The coupling between excitons and phonons across adjacent layers has been experimentally observed in various heterostructures of layered materials. However, the precise mechanism underlying this phenomenon remains elusive. Using the $WSe_2$@$h$BN heterostructure as an example, we study the origin of the interlayer exciton-phonon coupling and its signature in resonant Raman scattering through first-principles calculations. Our study emphasizes the central role of crystal symmetries in the interlayer exciton-phonon scattering processes, which are responsible for the anomalous resonant Raman intensities of the in-plane and the out-of-plane $h$BN phonon modes. We find that the deformation potential induced by the $h$BN phonon interacts with the hybridized hole density of $WSe_2$ excitons near the $h$BN interface, leading to interlayer exciton-phonon coupling. This work is taken directly from Ref. [81]

## 5.1 Introduction

In recent years, the interfacing of two-dimensional (2D) materials with different layers or substrates [34] has revealed fascinating properties that are difficult to achieve with individual layers. For example, interlayer electron-electron interactions can give rise to diverse phenomena such as moiré excitons [96], superconducting phases [13], and Mott insulating states [92]. Similarly, interlayer electron-phonon interactions can have profound effects on carrier mobilities [18] and even influence superconducting critical temperatures [114], further underscoring the importance of these interactions in tailoring the properties of 2D heterostructures.

Recent optical scattering measurements have revealed that excitons (electron-hole bound states) in one layer can couple with phonons in the adjacent layer [55, 62, 54, 28, 27, 20]. This remarkable interlayer exciton-phonon coupling was first demonstrated in monolayer $WSe_2$ encapsulated in hexagonal boron nitride ($h$BN) using Raman spectroscopy [55]. Subsequent Raman and photoluminescence [20, 54] measurements on various other heterostructures such as Black phosphorus@$SiO_2$, metal phosphorus trichalcogenides@$SiO_2$ [16], $WS_2$@$Bi_2Se_3$ [51] confirmed the existence of interlayer exciton-phonon coupling, indicating that the observed phenomenon is robust and is not limited to $WSe_2$@$h$BN heterostructure.

The interlayer exciton-phonon coupling can play a key role in exciton dynamics, their lifetimes, and decoherence times [15], and has recently been used to study phonon polaritons in neighboring layers [110, 126]. Therefore, understanding the origin of these interlayer exciton-phonon interactions is crucial to leverage these interactions for future applications. Although the signatures of interlayer exciton-phonon coupling in these measurements provided an ideal setting to study this phenomenon, the microscopic mechanism remains elusive. A speculative mechanism was proposed in Ref. [20], suggesting that two polar phonon modes, one from each layer, couple via a dipole-dipole interaction. This mechanism assumes that the bond polarity in one layer and the intralayer exciton-phonon interaction in the other layer play a fundamental role in these interactions [27]. Although this argument seemed plausible initially, it failed to explain the resonant Raman intensities of non-polar

modes in these heterostructures [27]. Furthermore, the proposed mechanism could not account for the sensitive dependence of the exciton-phonon coupling strength on the interlayer distance [62].

In this thesis, we use $WSe_2$@$h$BN as an example to unveil the microscopic mechanism of exciton-phonon coupling across layers. Using *ab initio* methods, we compute resonant Raman intensities, which provide a detailed atomistic view of the interlayer exciton-phonon scattering process. We demonstrate the selection rules in interlayer exciton-phonon scattering, which are responsible for the anomalous resonant Raman intensities: When in resonance with the A exciton of $WSe_2$, the out-of-plane $h$BN phonon mode (which is Raman forbidden in pure $h$BN) exhibits a much higher intensity in the heterostructure than the Raman-allowed in-plane mode [55]. Our main findings reveal that the deformation potential of the $h$BN phonon scatters the hybridized part of the $WSe_2$ exciton-hole in the vicinity of the $h$BN layer, giving rise to interlayer exciton-phonon coupling. We show that this coupling is extremely sensitive to the interlayer distance and that the bond polarity of the phonon layer is not required to observe this effect [54, 28, 27, 20].

## 5.2 Results and Discussion

### 5.2.1 Resonant Raman scattering

We start our discussion by looking at the resonant Raman scattering in a monolayer $WSe_2$@$h$BN heterostructure. We follow Refs. [94, 95] and calculate the differential cross section for Stokes Raman scattering mediated by one phonon:

$$\frac{\mathrm{d}\sigma}{\mathrm{d}\Omega} \propto \frac{\omega_{\mathrm{L}} - \omega_\lambda}{\omega_{\mathrm{L}}} |\mathcal{M}^\lambda_{\mu\nu}(\omega_L, \omega_\lambda)|^2. \tag{5.1}$$

Here, $\mu$ and $\nu$ denote the polarization of the incoming and outgoing light, respectively, while $\omega_{\mathrm{L}}$ and $\omega_\lambda$ denote the frequencies of the incoming light and the created phonon of branch $\lambda$, respectively. Within the Tamm-Dancoff approximation [22], the Raman scattering matrix

element $\mathcal{M}^{\lambda}_{\mu\nu}$ at zero temperature takes on the simple form

$$\begin{aligned}\mathcal{M}^{\lambda}_{\mu\nu}\left(\omega_L,\omega_\lambda\right) = &\sum_{S,S'}\frac{\left(d^{\nu}_{S'}\right)^{*}\left(\mathcal{G}^{\lambda}_{SS'}\right)^{*}d^{\mu}_{S}}{\left(\hbar\omega_{\mathrm{L}}-E_S+i\gamma\right)\left(\hbar\omega_{\mathrm{L}}-\hbar\omega_\lambda-E_{S'}+i\gamma\right)}\\ &+\sum_{S,S'}\frac{\left(d^{\mu}_{S}\right)^{*}\mathcal{G}^{\lambda}_{SS'}d^{\nu}_{S'}}{\left(\hbar\omega_{\mathrm{L}}+E_S-i\gamma\right)\left(\hbar\omega_{\mathrm{L}}-\hbar\omega_\lambda+E_{S'}-i\gamma\right)}.\end{aligned} \tag{5.2}$$

The sums run over all excitonic states $S$ and $S'$ with energies $E_{S(\prime)}$ and decay constant $\gamma$. The quantity $d^{\mu}_{S}$ is the coupling matrix element between an exciton $S$ and a photon of polarization $\mu$, while $(\mathcal{G}^{\lambda}_{SS'})^{*}$ represents the exciton-phonon coupling matrix element related to the scattering of an exciton $S$ to an exciton $S'$ *via* emission of one phonon of branch $\lambda$ [95].

The exciton-phonon matrix element $g^{\lambda}_{SS'}$ for the state $|S'\rangle$ scattering to the state $|S\rangle$ via absorption of phonon of zero momentum is given by Eq. (4.7) which can be simplified as

$$\mathcal{G}^{\lambda}_{SS'} = \sum_{\mathbf{k}cv}\{A^{S^{*}}_{\mathbf{k}cv}\big(\sum_{c'}g^{\lambda}_{\mathbf{k}cc'}A^{S'}_{\mathbf{k}c'v}-\sum_{v'}g^{\lambda}_{\mathbf{k}v'v}A^{S'}_{\mathbf{k}cv'}\big)\}, \tag{5.3}$$

where $g^{\lambda}_{\mathbf{k}mn} = \langle\mathbf{k}m|\partial_\lambda V|\mathbf{k}n\rangle$ corresponds to the electron-phonon matrix element between the single electron states $|\mathbf{k}n\rangle$ and $|\mathbf{k}m\rangle$, with $\partial_\lambda V$ representing the deformation potential due to the phonon mode $\lambda$. If an exciton is mostly composed of one valence and one conduction band at each k-point (like $1s/2s$ excitons in $WSe_2$), we can approximate the diagonal exciton-phonon matrix element in Eq. (5.3) as

$$\mathcal{G}^{\lambda}_{SS} \approx \sum_{\mathbf{k}}\{|A^{S}_{\mathbf{k}}|^2\big(g^{\lambda}_{\mathbf{k}\tilde{c}\tilde{c}}-g^{\lambda}_{\mathbf{k}\tilde{v}\tilde{v}}\big)\}, \tag{5.4}$$

where $\tilde{c}/\tilde{v}$ are the band indices of the conduction/valence band indices that contribute the most to the envelope wave function at a given k-point.

The exciton-photon (dipole) matrix elements $d^{\mu}_{S}$ are given by

$$d^{\mu}_{S} = \sum_{\mathbf{k}cv}\left(A^{S}_{\mathbf{k}cv}\right)^{*}\langle c\mathbf{k}|\hat{\mathbf{v}}|v\mathbf{k}\rangle\cdot\mathbf{e}^{\mu}, \tag{5.5}$$

where $\hat{\mathbf{v}}$ is the velocity operator, $\mathbf{e}^{\mu}$ is the polarization vector of the incoming photon, and

the sums run over all $\mathbf{k}$-points in the first Brillouin zone, over all conduction bands ($c$) and valence bands ($v$). $\langle c\mathbf{k}|\hat{\mathbf{v}}|v\mathbf{k}\rangle$ represents the dipole matrix elements, and $A^S_{\mathbf{k},cv}$ is the exciton envelope wave function for the single-electron transition $|\mathbf{k}, v\rangle \rightarrow |\mathbf{k}, c\rangle$. Detailed derivation of these expressions can be found in the supplementary information of Ref. [95].

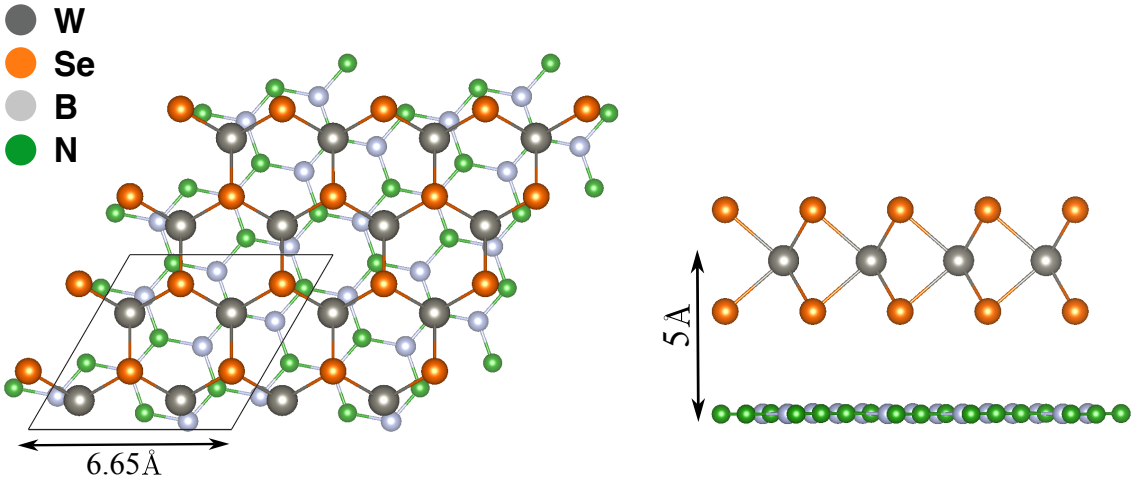


Figure 5.1: Top and side view of crystal structure of monolayer $WSe_2$ on top of single layer $h$BN used in the *ab-initio* calculations. Figures were created with the VESTA software [76]

We obtained all quantities required for the evaluation of Eq. (5.2) from first principle methods using the GW-BSE [53, 98] formalism on density functional theory (see supplementary information section 5.3 for details of the *ab initio* methods). Experimental evidence [126] shows that the interlayer exciton-phonon phenomenon persists even for a single layer of $h$BN placed on top of $WSe_2$. Therefore, we considered a heterostructure consisting of one layer of $h$BN and one layer of $WSe_2$ as shown in Fig 5.1 in this study. This is sufficient to understand the underlying mechanism. Additional calculations for different structural configurations, including a sandwiched structure, are provided in the supplementary information section 5.3.

In Fig. 5.2a, we show the calculated Raman intensities for the different phonon branches as a function of the energy of the incoming photon at normal incidence ($\omega_L$). We define the Raman intensity as the differential cross section, averaged over the polarization of the incoming light at normal incidence, and summed over the in-plane polarization of the outgoing light. The blue line denotes the Raman intensities for the out-of-plane optical (ZO)

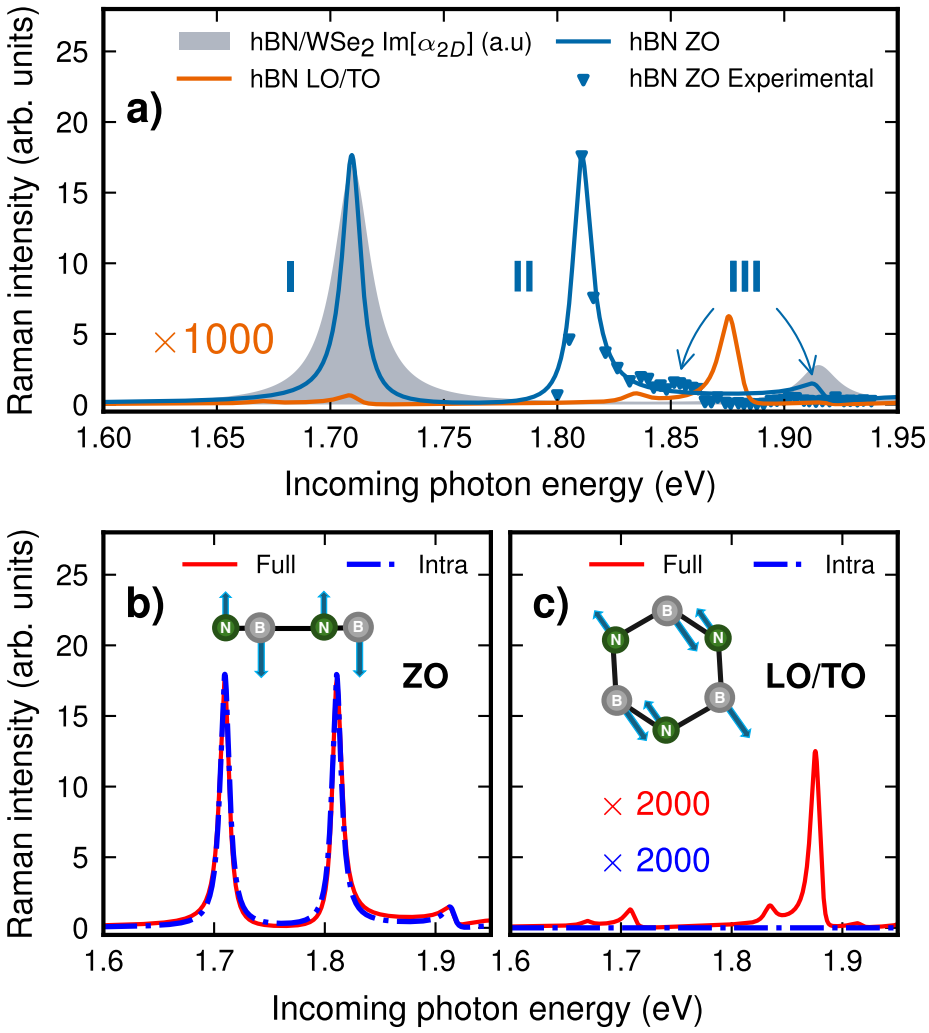


Figure 5.2: Raman intensities of the ZO and LO/TO modes of $h$BN in a heterostructure of single layers of $h$BN and $WSe_2$ as a function of energy of the incoming photon at normal incidence. ($\omega_L$). a) Computed resonant Raman intensities of the ZO mode (blue line) and LO/TO mode (orange line). The gray shaded area denotes the imaginary part of the in-plane polarizability of the heterostructure. Blue triangles represent experimental data of the ZO mode Raman intensities at 4 K, taken from Ref. [70]. (b) and (c) Computed Raman intensities for (b) the ZO mode and (c) the LO/TO mode, considering all scattering channels (red lines) or retaining only intra-exciton scattering channels (blue line).

phonon of the hBN layer. We compare the Raman intensity profiles to the imaginary part of the in-plane polarizability (absorption coefficient) of the heterostructure (shaded area) and to experimental Raman intensities from McDonnell *et al.* [70](blue triangles, see supporting information section 5.3 for further details). The most striking features of the ZO-mode intensity profile are the two strong resonances at $\omega_{\mathrm{L}} \approx 1.72$ eV and $\omega_{\mathrm{L}} \approx 1.82$ eV, labeled "I" and "II" in Fig. 5.2a. The first of these two peaks coincides with a resonance in the absorption coefficient which corresponds to the well-known $1s$ state of the "A"-exciton [5] of $WSe_2$ and can thus be interpreted as the resonant excitation of the $1s$ A-exciton in $WSe_2$, which then couples to the $h$BN ZO mode. The second peak, in contrast, does not have such a counterpart in the absorption spectrum. It is the quantum of one ZO mode away from the first resonance peak and corresponds to the resonant recombination of the $1s$ exciton under phonon emission (when $\omega_{\mathrm{L}} = E_{1s} + \omega_{\mathrm{ZO}}$), compare Eq. (5.2). Finally, Peak III coincides with the $2s$-A-exciton of the absorption coefficient and is due to the resonant excitation of the $2s$ state. The results of our calculation match the experimental data of McDonnell *et al.* [70] well in terms of the local peak intensities. We note that the $2s$ exciton is blue-shifted in our calculation with respect to experiment, as we consider a heterostructure of one layer $WSe_2$ on top of one layer of $h$BN vs. a system of monolayer $WSe_2$ sandwiched in bulk $h$BN in experiment (where screening is stronger and, thus, the energy difference between $1s$ and $2s$ excitons reduced. See Fig. 5.8 in supporting information section 5.3) [5].

Compared to the ZO mode of $h$BN, its in-plane LO/TO mode displays a Raman intensity three orders of magnitude lower, yet with a qualitatively similar resonance structure as a function of $\omega_{\mathrm{L}}$. This anomalous behavior, where the ZO and LO/TO phonon modes of the $h$BN layer couple differently when the incident light is in resonance with the $WSe_2$ layer, was reported in Ref. [55], which offered a speculative explanation for the underlying Raman scattering process. Using our atomistic first-principles approach, we can now scrutinize the Raman scattering pathways and understand them in terms of symmetry and involved scattering events.

From Eq. (5.2), it is evident that any contributing scattering pathway requires non-zero optical matrix elements $d_S^{\mu}$ and $d_{S'}^{\nu}$ as well as a non-vanishing exciton-phonon coupling ma-

trix element $g^{\lambda}_{S,S'}$. Monolayer $WSe_2$ and monolayer/bulk $h$BN individually possess $D_{3h}$ and $D_{3h}/D_{6h}$ point groups, respectively. However, when combined into a heterostructure, the symmetry is reduced to $C_3$, which is crucial for observing valley effects and preserving the isotropic properties in these systems [26].

In order to infer the corresponding selection rules, we note that the underlying $C_3$ point group symmetry of the $h$BN@$WSe_2$ heterostructure allows the classification of zero-momentum phonons and excitons with total crystal angular momentum $m = +1$, 0, or $-1$. Each value of $m$ corresponds to an irreducible representation of the $C_3$ point group, with characters given by $e^{\frac{2\pi i m}{3}}$ for the 3-fold rotation symmetry. A finite optical strength $d^{\mu}_{S}$ for light polarized parallel to the heterostructure is only possible for excitons $S$ with $m_S = \pm 1$. Meanwhile, the exciton-phonon matrix elements $g^{\lambda}_{S,S'}$ are non-zero only if $m$ is conserved up to modulo 3:

$$m_S - m_{S'} - m_{\lambda} \equiv 0 \text{ (mod 3)}. \tag{5.6}$$

For the ZO-phonon ($m_{\mathrm{ZO}} = 0$), this implies that active scattering pathways necessarily have $m_S = m_{S'}$. In contrast, for the LO/TO phonon ($m_{\mathrm{LO/TO}} = \pm 1$), we need to have $m_S = m_{S'} \pm 1$ (mod 3).

The combination of the optical and phonon-specific selection rules allows us then to understand the nature of the resonance features I, II, and III in Fig. 5.2a. As the $1s$ exciton of $WSe_2$ is the dominant optically active low energy exciton available, resonance I and II are associated with the scattering process $1s \to 1s$, which gives rise to resonances for both incoming (I) and outgoing (II) light. However, while this resonance structure is seen in both the ZO and the LO/TO mode, the latter is three orders of magnitude less intense, although formally allowed by symmetry. To understand this enormous difference between the phonon modes, we first note that the $1s$ exciton of $WSe_2$ is in fact doubly degenerate due to time-reversal symmetry [50]. The two members of the doublet are located at different inequivalent corners K and K′ of the first Brillouin zone and carry the opposite $m$ value, i.e. $m_{1s,K^{(\prime)}} = +(-)1$. For the ZO mode, this implies that $1s \to 1s$ scattering is allowed *within* a valley (*intra*-valley scattering), while for the LO/TO mode with $m$ value, $1s \to 1s$ scattering is only allowed

between $1s$ states in *opposite* valleys (*inter*-valley scattering). However, due to the strong localization of the $1s$ exciton wave function in momentum space (see Fig. 5.7 of supporting information section 5.3), there is only a miniscule overlap between wave functions centered in different valleys and, as a result, the inter-valley scattering required for the LO/TO mode is strongly suppressed and, consequently, the Raman intensity.

In order to substantiate this, we recalculate the Raman intensities by considering only intra-exciton scattering channels, *, i.e.*, by restricting the double sum in Eq. (5.2) to $S = S'$. As shown in Figs. 5.2b and c, we can indeed numerically confirm that intra-exciton scattering is absent for the LO/TO mode while being the dominant scattering process for the ZO mode. In terms of the three most prominent resonances in the ZO mode Raman intensities, we can thus conclude that resonances I and II stem from $1s$-to-$1s$ intra-valley exciton scattering and III from $2s$-to-$2s$ intra-valley scattering. We note that this finding is in contrast to previous assumptions [55] that identified peaks II and III to the two resonances associated with the inter-exciton scattering process $1s \rightarrow 2s$.

However, for the LO/TO mode, we confirm that intra-valley scattering plays no role, and the suppressed but finite Raman intensity around the $1s$ exciton arises solely from weak inter-exciton scattering. Along with the $1s$ exciton, these weak inter-exciton scattering processes include finite-momentum excitonic states of pristine $WSe_2$, which are folded onto the $\Gamma$ point due to the supercell and are weakly brightened as a result of the reduced symmetry of the heterostructure. Unlike the $1s$ and $2s$ excitons, these finite-momentum excitons of pristine $WSe_2$ are not localized in the $K$ valleys due to exchange interaction, as reported in Ref. [91]. This suggests that, in addition to inter-valley scattering between degenerate $1s$ excitons, the $1s$ excitons can also scatter to these weakly brightened excitons, and vice versa. Collectively, these inter-exciton scattering channels result in the very weak Raman intensities observed for the LO/TO phonon mode between the $1s$ and $2s$ exciton energies.

### 5.2.2 Interlayer exciton-phonon coupling

While these symmetry considerations explain the difference between Raman intensities of the LO/TO- and ZO-modes, a complementary analysis is required to understand the precise

mechanism for interlayer exciton-phonon coupling. In order to elucidate the microscopic mechanism, we consider the $1s \rightarrow 1s$ scattering pathway for the ZO mode, which is the dominant Raman scattering channel in the region $\omega_{\mathrm{L}} \lesssim$1.8 eV. The $1s$ exciton is mostly composed of one conduction and one valence band state 5.3, therefore we can approximate the $1s \rightarrow 1s$ exciton-phonon matrix element as (see supplementary information section 5.3 for details)

$$\mathcal{G}^{\mathrm{ZO}}_{1s,1s} \approx \sum_{\mathbf{k}} \left|A^{1s}_{\mathbf{k}cv}\right|^2 \left(g^{ZO}_{\mathbf{k}c} - g^{ZO}_{\mathbf{k}v}\right), \tag{5.7}$$

where $A^{1s}_{\mathbf{k}cv}$ is the exciton envelope wave function for the single-electron transition $|\mathbf{k}, v\rangle \rightarrow |\mathbf{k}, c\rangle$. The diagonal *electron*-phonon matrix elements $g^{\mathrm{ZO}}_{\mathbf{k}n}$ for a single-electron state $|\mathbf{k}n\rangle$ within the framework of DFT are given by [38]

$$g^{\mathrm{ZO}}_{\mathbf{k}n} = \int \mathrm{d}^3\mathbf{r}\, |\psi_{\mathbf{k}n}(\mathbf{r})|^2 \partial_{\mathrm{ZO}} V_{\mathrm{KS}}(\mathbf{r}). \tag{5.8}$$

Here, $\psi_{\mathbf{k}n}(\mathbf{r})$ denotes the one-electron wave function for state $|\mathbf{k}n\rangle$, $V_{\mathrm{KS}}(\mathbf{r})$ corresponds to the total self-consistent Kohn-Sham (KS) potential, and $\partial_{\mathrm{ZO}}$ represents the directional derivative along the ZO phonon mode displacement vector [38]. Combining Eqs. (5.7) and (5.8), we obtain

$$\mathcal{G}^{\mathrm{ZO}}_{1s,1s} \approx \int \mathrm{d}^3\mathbf{r}\, \left[n^{1s}_c(\mathbf{r}) - n^{1s}_v(\mathbf{r})\right] \partial_{\mathrm{ZO}} V_{\mathrm{KS}}(\mathbf{r}), \tag{5.9}$$

where $n^{1s}_{c(v)}(\mathbf{r}) = \sum_{\mathbf{k},v(c)} |A^{1s}_{\mathbf{k}cv}|^2 |\psi_{\mathbf{k}c(v)}(\mathbf{r})|^2$ denotes an "exciton-averaged" electron ($c$) or hole ($v$) density for the $1s$ exciton.

Previous studies [54, 28, 27, 20] have suggested that the polar nature of the ZO phonon is responsible for the origin of the interlayer exciton-phonon coupling. To verify this claim, we decompose the total perturbed potential in Eq. (5.9) into macroscopic and microscopic components [109]: $\partial_{\mathrm{ZO}} V_{\mathrm{KS}}(\mathbf{r}) = \partial_{\mathrm{ZO}} V_{\mathrm{micro}}(\mathbf{r}) + \partial_{\mathrm{ZO}} V_{\mathrm{macro}}(\mathbf{r})$. These macroscopic and microscopic fields are also referred to as the long-range and short-range components of the deformation field, respectively, in the literature [38, 104, 109]. In polar materials, the macroscopic component predominantly arises from a macroscopic dipole field generated by the presence of Born effective charges and is often termed the *Fröhlich* field [109]. It also includes mi-

nor contributions from fields generated by quadrupole moments[11] and other higher-order multipole terms for both polar and non-polar materials [42]. The microscopic component of the perturbed potential is obtained by subtracting the macroscopic component from the total perturbed potential. In this work, we only considered dipole terms in the macroscopic part, as higher-order multipole terms are negligible.

In Figure 5.3, we illustrate the different components of the $1s \rightarrow 1s$ exciton-phonon matrix element, as described by Eq. (5.9). We plot the in-plane average of the change in KS potential (divided into microscopic and macroscopic part) and the integrated electron and hole densities as a function of the out-of-plane spatial coordinate ($z$). We distinguish between the region close to the $h$BN layer, the *near field* (grey shading), and the remaining area, the *far field*. Figure 5.3a shows the in-plane average of the microscopic (magenta line) and macroscopic (blue line) components of the total field (see supplementary information section 5.3 for computational details). The macroscopic component attains a constant value on both sides of the $h$BN layer and extends entirely along the out-of-plane direction, resembling the field generated by a uniformly charged plate. Conversely, the microscopic component vanishes asymptotically due to the charge neutrality of the system. Interestingly, the microscopic part exhibits two prominent features: (i) a large and rapidly varying part in the near field, and (ii) a tiny part in the far field that is localized within the $WSe_2$ layer, as depicted in the inset of Fig. 5.3b. The former arises from the change in lattice potential due to the displacement of nuclei and the induced field of the $h$BN electron density; the latter is due to the induced field generated by the $WSe_2$ electron density [38].

The different components of the total field are felt by the $1s$ exciton charge density of the $WSe_2$ layer. In Fig. 5.3b, we depict the in-plane integrated electron and hole densities ($n^{1s}_{c/v}(\mathbf{r})$) of the $1s$ exciton (see supplementary information section 5.3 for similar plots corresponding to different stackings and encapsulated heterostructures). Both the electron and hole densities of the $1s$ exciton are mostly made up of tungsten $d$ orbitals [112]. However, while the electron density of the $1s$ exciton is completely localized within the $WSe_2$ layer, the hole density also has a small, but finite component in the $h$BN layer (see inset of Fig. 5.3b). This component corresponds to the hybridization of the $p_z$ orbitals of the $h$BN layer with

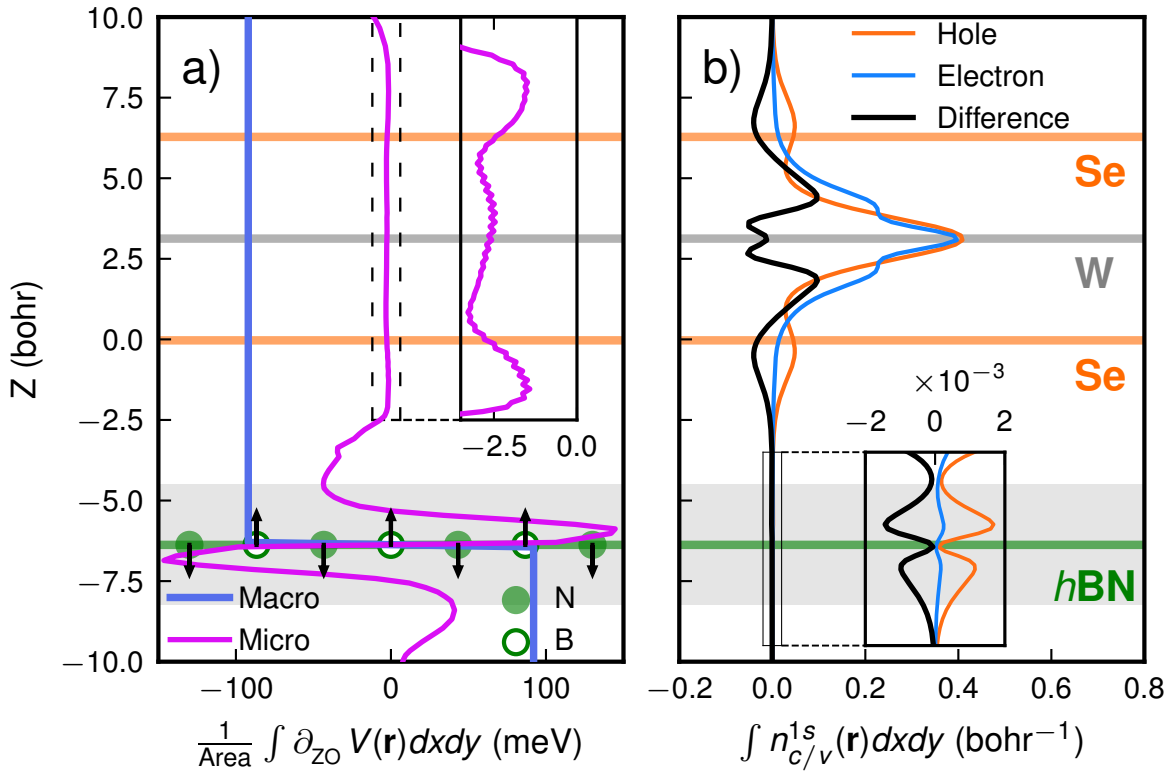


Figure 5.3: Illustration of the different components of $1s \rightarrow 1s$ exciton-phonon matrix element as given in Eq. (5.9), plotted against the out-of-plane spatial coordinate. The horizontal orange, grey, and green lines correspond to the spatial positions of the Se, W, and $h$BN atomic layers, respectively. The grey/white shading represents the near-field/far-field regime of the $h$BN layer. (a) In-plane averaged microscopic (magenta) and macroscopic components (blue) of the total field. The arrows on the B and N atoms represent the ZO phonon mode displacement pattern. (b) In-plane integrated electron and hole densities of the $1s$ exciton.

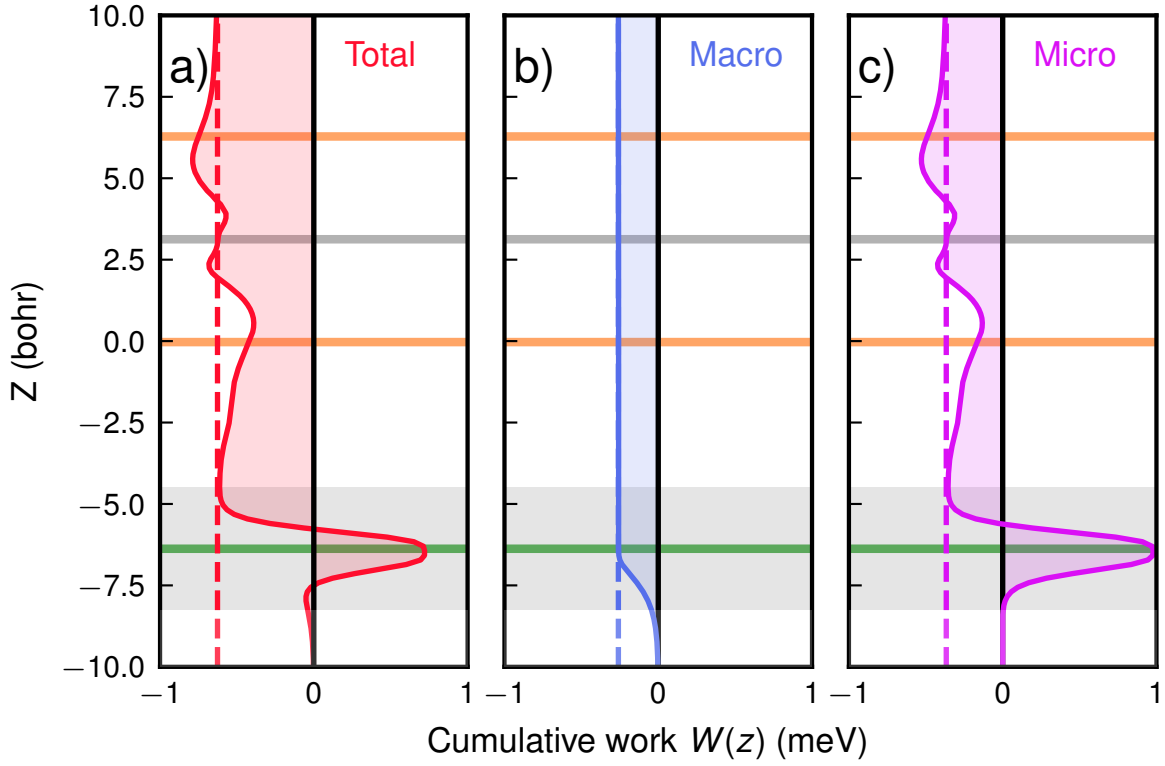


Figure 5.4: Cumulative work done by (a) the total field, (b) its macroscopic component, and (c) its microscopic component as defined in Eq. (5.10). The vertical dashed lines indicate the asymptotic values.

the $d$ orbitals of the $WSe_2$ layer, *i.e.*, to the weak chemical bond between the two layers. It is noteworthy that the hybridization only occurs for the valence, *i.e.*, bonding orbitals, and not for the conduction band orbitals, owing to the favourable or unfavorable band alignment between the $h$BN and $WSe_2$ valence and conduction bands, respectively. This hybridization has been experimentally observed and reported in Ref. [63].

Finally, we consider the interaction of the electron and hole densities of the $1s$ exciton with the total field to gain atomistic insight on the exciton-phonon interaction across layers. The $1s \rightarrow 1s$ exciton-phonon matrix element can *a priori* receive contributions from three different channels: (i) the constant, macroscopic part interacting with the electron and hole densities over all space (ii) the large near field interacting with the small hybridized hole density in the near-field, and (iii) The small far field in the $WSe_2$ layer interacting with the

large electron and hole densities.

To quantify the contribution of each channel to the overall exciton-phonon interaction, we define the cumulative work $W(z)$ along the z axis for a field $\partial V(\mathbf{r})$ as

$$W(z) = \int_{-\infty}^{z} \mathrm{d}^3\mathbf{r} \left(n_c^{1s}(\mathbf{r}) - n_v^{1s}(\mathbf{r})\right)(\partial V(\mathbf{r}) - \partial V(\mathbf{r} \to \infty)). \tag{5.10}$$

The cumulative work for the total field asymptotically reaches the diagonal exciton-phonon matrix of the $1s$ exciton as given in Eq. 5.9 (see cumulative work section in supplementary information section 5.3 for more details).

In Fig. 5.4, we depict the cumulative work done by the total field and its constituents, denoting their asymptotic values with dashed, vertical lines. The cumulative work for the total field starts from zero and reaches its asymptotic value by the end of the near-field region as shown in Fig. 5.4a. This implies that the coupling of the $1s$ exciton to the ZO phonon arises almost entirely from the electric fields in the near-field region and their interaction with the hybridized part of the charge density of the $1s$ exciton. Given that only the hole of the $1s$ exciton hybridizes with the $h$BN orbitals, the $1s \to 1s$ exciton-phonon scattering can be interpreted as being primarily due to the scattering of the hybridized-hole by the ZO phonon, thereby making it a near-field effect.

To better understand the nature of this near-field effect, we further examine the contributions of each individual field to the total exciton-phonon coupling by considering the cumulative work of the macroscopic and microscopic components separately. Since the ZO phonon is antisymmetric about the $h$BN plane, both the macroscopic and microscopic fields flip their sign at the $h$BN layer (see Fig. 5.3a). At the same time, due to lowering of symmetry in the heterostructure, the hybridized-hole density around the $h$BN layer is *not* mirror symmetric with respect to the $h$BN plane. In combination with the large microscopic and macroscopic fields, this asymmetry leads to a finite amount of work in the near-field region (see Fig. 5.4b and c). By contrast, in the far-field regime, the electron and hole distribution are mirror symmetric with respect to the W-layer and in consequence, the net work done by the ZO mode to the exciton cancels out.

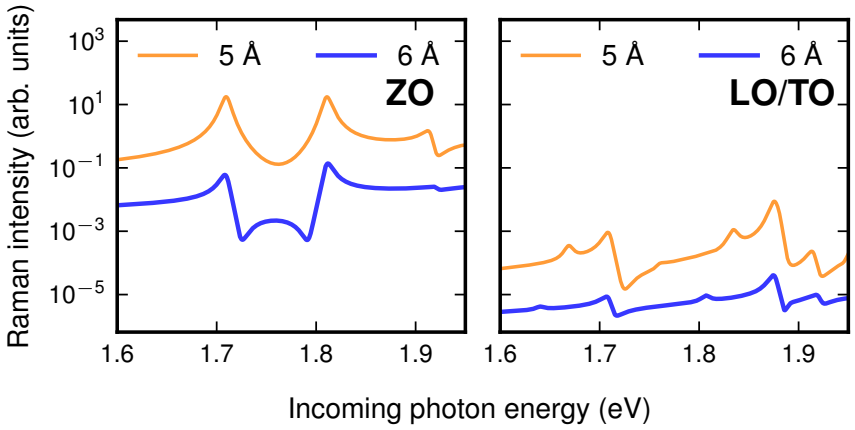


Figure 5.5: Resonant Raman intensities of ZO (left) and LO/TO (right) phonons of $h$BN at an interlayer spacing (between tungsten and $h$BN layer) of 5 Å (orange) and 6 Å (blue)

Further insights can be drawn from the behavior of the macroscopic component. While the macroscopic part interacts with the entire electron and hole densities, the cumulative work reaches its asymptotic value already at the interface of the $h$BN layer and the region around the $WSe_2$ layer does not yield a net contribution. Given that the macroscopic component is nearly constant, the work done by the electron and by the hole compensate each other almost perfectly in the far-field, as a consequence of the exciton being a charge-neutral excitation. However, the macroscopic part does contribute a finite amount of work to the exciton-phonon coupling through its interaction with the hybridized part of the hole density (Fig. 5.4c). This implies that, similar to the microscopic contribution, the macroscopic contribution also depends heavily on the hybridized density, thereby making it a near-field effect (see cumulative work section in supplementary information section 5.3 for more details).

Given the near-field nature of interlayer exciton-phonon coupling, it is highly sensitive to interlayer distance, as increasing the separation between layers exponentially decreases the interfacial hybridization and, consequently, the coupling strength. To qualitatively validate this, we computed the resonant Raman intensities for the same heterostructure with two different interlayer distances of 5 Å and 6 Å. As shown in Fig. 5.5, the Raman intensities decrease by two orders of magnitude when the interlayer spacing is increased by 20%. This

qualitatively agrees with the experimental observations in Ref. [62] and confirms the near-field effect of this phenomenon.

Finally, it is important to emphasize the fundamental distinction between interlayer *electron*-phonon and *exciton*-phonon couplings. Unlike the interlayer *electron*-phonon coupling, which is very strong and is predominantly caused by the macroscopic component in the far-field region [104], the interlayer *exciton*-phonon coupling is much weaker and originates in the near-field region, with nearly equal contributions coming from both macroscopic and microscopic components. Remarkably, exciton-phonon scattering takes place even in the absence of the macroscopic component. This implies that bond polarity is not a prerequisite for the occurrence of the interlayer exciton-phonon scattering, contrary to current speculations [54, 28, 27, 20], which hypothesized a macroscopic dipole-dipole coupling mechanism.

## 5.3 Supporting information

### 5.3.1 Computational details

All the ground state properties presented in the paper are obtained from density functional theory calculations (DFT) within the generalized gradient approximation [86] as implemented in the `QUANTUM ESPRESSO` Code [37]. We use the Perdew-Burke-Ernzerhof (PBE) functional [86] and fully relativistic norm-conserving pseudo-potentials (SG15 database) to perform all the DFT calculations [46, 100]. A plane-wave energy cutoff of 120 Ry is used to expand the wave functions. The heterostructure used for all the *ab-initio* calculations is shown in Fig. 5.1. This heterostructure is generated using the `CELLMATCH` software [58], with the same parameters as mentioned in Ref.[35]. We then relax the structure with a convergence threshold of $10^{-5}$ Ry and $10^{-5}$ Ry/Bohr for total energy and forces, respectively. After the relaxation, the obtained interlayer distance between the Tungsten and hBN layers is 5 Å which is in good agreement with Ref. [35]. In order to avoid spurious effects of out-of-plane periodicity, we set the vacuum separation to 20 Å and employ a Coulomb cutoff in all our *ab-initio* calculations [103]. We then obtain phonons and electron-phonon coupling matrix elements within density functional perturbation theory as implemented in the `PH.x`

code of QUANTUM ESPRESSO. A $\Gamma$ centered $9\times9\times1$ uniform k point grid is used to converge the ground state density, and we employ the same k-grid for the phonon calculations.

To obtain the total change in the Kohn-Sham potential, $\partial_{\mathrm{ZO}}V_{\mathrm{KS}}(\mathbf{r})$, for plotting purposes, we construct the change in the local part of the total ionic potential from the pseudopotentials as described in Ref. [103]. This is then added to the perturbed Hartree and exchange-correlation potentials obtained from DFPT calculations.

The macroscopic part is computed using an analytical expression from Ref. [23], given in atomic units as

$$\partial_{\mathrm{ZO}}V_{\mathrm{macro}}(\mathbf{r}_{\parallel},z)=\frac{2\pi i}{A}\sum_{\kappa}\sum_{\mathbf{Q}=\mathbf{G}_{\parallel}}e^{-|\mathbf{Q}||z-z_{\kappa}|}e^{i\mathbf{Q}\cdot(\mathbf{r}-\boldsymbol{\tau}_{\kappa})}\frac{\left[\hat{\mathbf{Q}}+i\hat{\mathbf{z}}\,\mathrm{sgn}(z-z_{\kappa})\right]\cdot\mathbf{Z}^{*}_{\kappa}\cdot\mathbf{u}^{ZO}_{\kappa}}{1+2\pi\hat{\mathbf{Q}}\cdot\boldsymbol{\alpha}^{\mathsf{2D}}\cdot\hat{\mathbf{Q}}|\mathbf{Q}|}. \tag{5.11}$$

Here, $A$ is the unit cell area, $\mathbf{G}_{\parallel}$ is the in-plane reciprocal vector, $\hat{\mathbf{Q}}$ and $\hat{\mathbf{z}}$ are unit vectors along $\mathbf{Q}$ and $\mathbf{z}$, respectively, sgn is the sign function, and $\boldsymbol{\alpha}^{\mathsf{2D}}$ is the polarizability tensor which is given by

$$\boldsymbol{\alpha}^{\mathsf{2D}}=\frac{c}{4\pi}(\epsilon^{\infty}-1), \tag{5.12}$$

where $\epsilon^{\infty}$ is the static dielectric tensor, and $c$ is the out-of-plane lattice constant. The quantity $\mathbf{Z}^{*}_{\kappa}$ is the Born effective charge tensor of atom $\kappa$. The displacement vector for the ZO phonon mode, $\mathbf{u}^{ZO}_{\kappa}$, is

$$\mathbf{u}^{ZO}_{\kappa}=\frac{1}{\sqrt{2M_{\kappa}\omega_{ZO}}}\mathbf{e}^{\kappa}_{ZO}, \tag{5.13}$$

where $\mathbf{e}^{\kappa}_{ZO}$ is the phonon eigenvector, $\omega_{ZO}$ is the frequency of the ZO phonon mode, and $M_{\kappa}$ is the atomic mass of atom $\kappa$.

All the many-body perturbation theory calculations are performed on top of DFT calculations with the YAMBO code [65, 99]. In order to correct the Kohn-Sham band structure, we perform a $G_0W_0$ calculation on a uniform $\Gamma$ centred $12\times12\times1$ grid with a total of 2600 Kohn-Sham states. A plane wave cutoff of 2 Ry is used for the dielectric tensor to obtain the converged band gap. The frequency dependence of the dielectric tensor is calculated with the plasmon-pole approximation [40]. We also use a G-terminator [10] and RIM-W technique [44] to accelerate the convergence of the bandgap with respect to bands and k

points respectively. We interpolate the quasiparticle corrections to a finer k-point grid with the `Wannier90` code [89].

We solve the Bethe–Salpeter equation (BSE) within the Tamm-Dancoff approximation [22] starting from our previous mean field calculations with the `YAMBO` code. In order to obtain the converged absorption spectrum, we use a uniform $\Gamma$ centered $48 \times 48 \times 1$ grid with a total of 600 bands. We include the top eight valence and bottom eight conduction bands in constructing the kernel matrix. A plane wave cutoff of 25 Ry and 2 Ry is used for the exchange and the screened Coulomb part of the kernel. We use the `Elemental` library [90] to diagonalize the entire BSE Hamiltonian.

Finally, we employ Eqs. (2), (5.5) and (5.3) to compute the Raman scattering matrix elements from the dipoles, electron-phonon matrix elements and BSE envelope wave-functions. The summation in the Raman scattering matrix element is performed over the first 48000 excitonic states and the decay constant ($\gamma$) is set to 5 meV. We define the Raman intensity as the differential cross-section, averaged over the polarization of the incoming light at normal incidence and summed over the in-plane polarization of the outgoing light.

### 5.3.2 GW Band structure and exciton wave functions

In Fig. 5.6, we show the GW band structure for monolayer $WSe_2$ placed over a single layer of $h$BN. We interpolated the GW corrections on the high symmetry path using the `Wannier90` code

In Fig. 5.7, we plot the excitonic wave functions in reciprocal space ("envelope wave function") defined as

$$\Psi^S(\mathbf{k}) := \sum_{cv} \left| A^S_{\mathbf{k}cv} \right|^2 . \tag{5.14}$$

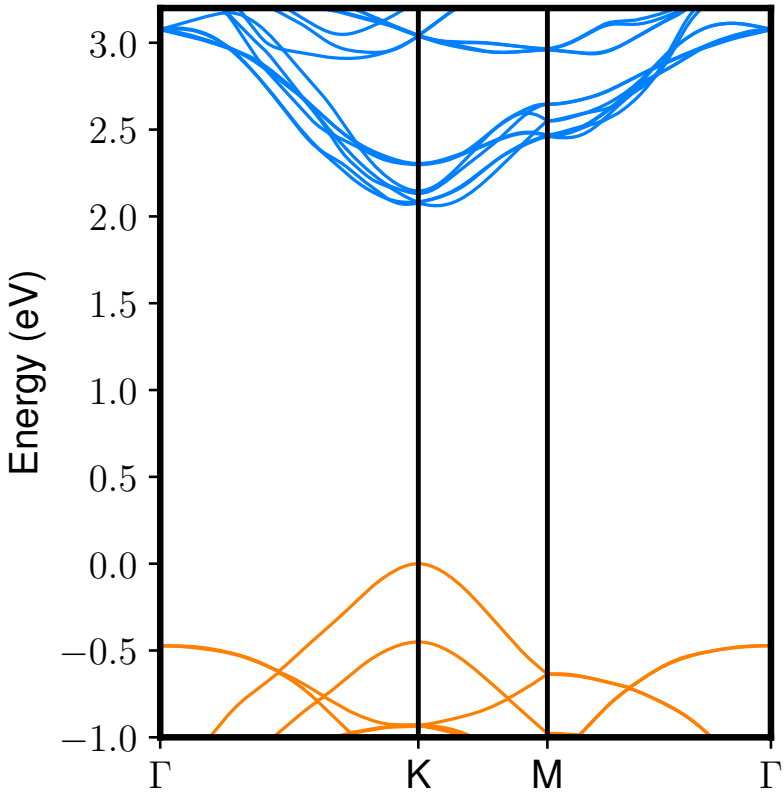


Figure 5.6: GW band structure of $WSe_2/h$BN heterostructure used in the main paper

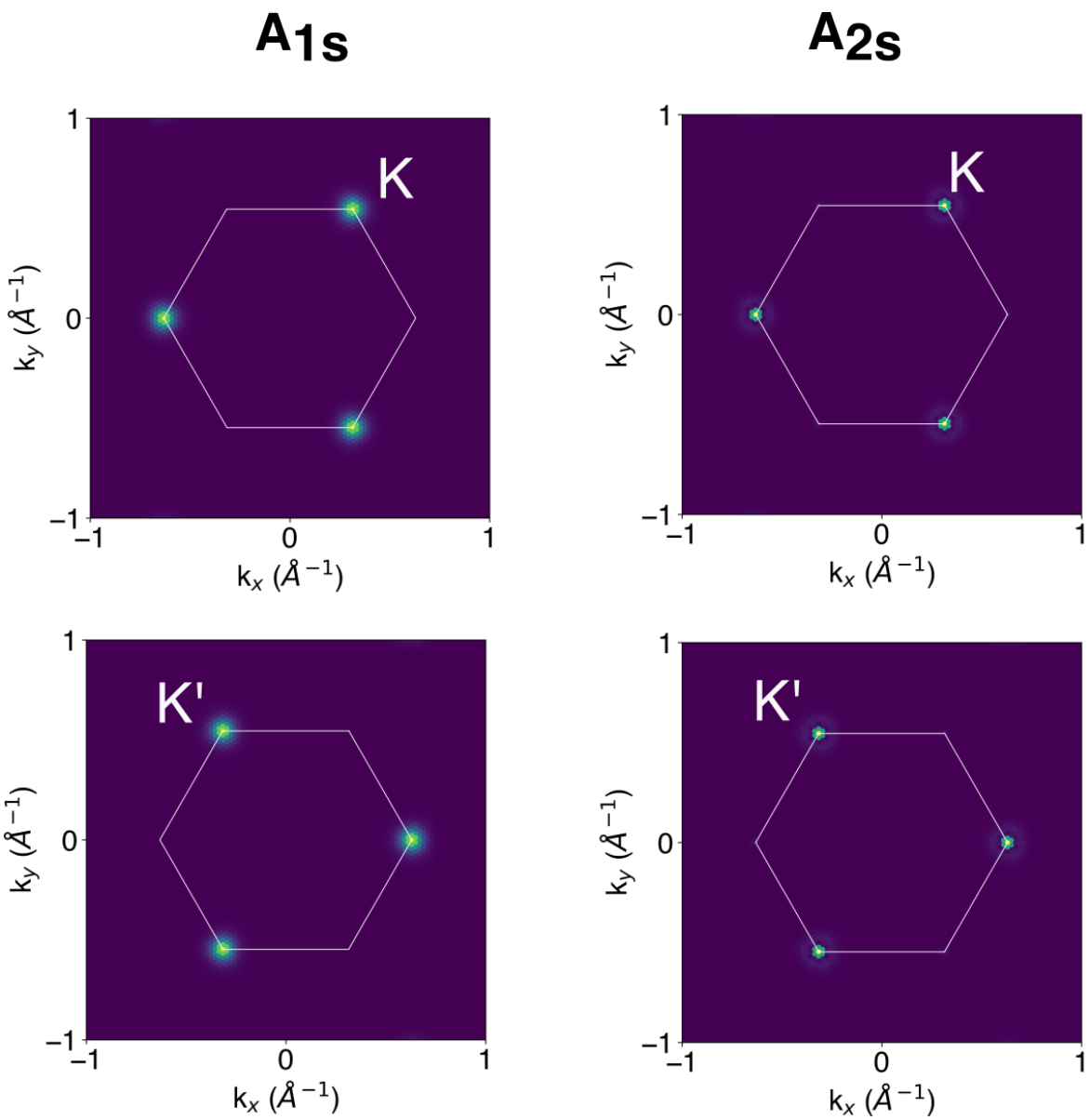


Figure 5.7: Envelope wavefunctions for the 1s and the 2s excitons located at two inequivalent K valleys

### 5.3.3 Cumulative work

In the main text, we introduced the term cumulative work. The cumulative work, $W(z)$, does not have a direct physical interpretation, although its asymptotic value for the total field corresponds to the diagonal exciton-phonon matrix element. This quantity is introduced to serve two purposes:

- To quantify the contributions of microscopic and macroscopic fields to the exciton-phonon strength.
- To identify the contributions from different spatial regimes to the interlayer exciton-phonon interaction, providing insight into whether the interlayer exciton-phonon coupling is microscopic or macroscopic.

To this end, $W(z)$ is defined by replacing the upper bound of the integral in Eq. (6) of the main text with the out-of-plane coordinate $z$. Since it represents an integrated charge density multiplied by the change in potential, we label it as "cumulative work".

Furthermore, according to Eq. (6) of the main text, the exciton-phonon matrix element remains unchanged when a constant field $E_0$ is added to the total field due to the charge neutrality of an exciton:

$$\int \mathrm{d}^3\mathbf{r}\ \left[n_c^{1s}(\mathbf{r}) - n_v^{1s}(\mathbf{r})\right](\partial_{\mathrm{ZO}} V_{\mathrm{KS}}(\mathbf{r}) + E_0) = \mathcal{G}^{\mathrm{ZO}}_{1s,1s} + \int \mathrm{d}^3\mathbf{r}\ \left[n_c^{1s}(\mathbf{r}) - n_v^{1s}(\mathbf{r})\right] E_0$$

$$= \mathcal{G}^{\mathrm{ZO}}_{1s,1s} + E_0 \times \left[\int \mathrm{d}^3\mathbf{r}\, n_c^{1s}(\mathbf{r}) - \int \mathrm{d}^3\mathbf{r}\, n_v^{1s}(\mathbf{r})\right] = \mathcal{G}^{\mathrm{ZO}}_{1s,1s}.$$

This implies that we have the freedom to add or subtract a constant field in Eq. (6). Based on this, we subtract the constant asymptotic field ($\partial V(\mathbf{r} \to \infty)$) on the right-hand side of Eq. (7) to isolate and discard its interaction with the electron and hole densities, as it does not contribute to exciton-phonon coupling.

By discarding the constant asymptotic field, the cumulative work of the macroscopic field reaches its asymptotic value when approaching the $h$BN interface, as shown in Fig. 3b. This

indicates that the macroscopic contribution arises from the interaction of the macroscopic field with *only* the interfacial hybridization. Therefore, the macroscopic contribution is directly related to the extent of interfacial hybridization.

Alternatively, this can be shown from Eq. (6):

$$\mathcal{G}^{\mathrm{ZO}}_{1s,1s} \approx \int \mathrm{d}^3\mathbf{r}\ \left[n_c^{1s}(\mathbf{r}) - n_v^{1s}(\mathbf{r})\right] \partial_{\mathrm{ZO}} V_{\mathrm{KS}}(\mathbf{r}) = \int \mathrm{d}^3\mathbf{r}\ \left[n_c^{1s}(\mathbf{r}) - n_v^{1s}(\mathbf{r})\right] \left(\partial_{\mathrm{ZO}} V_{\mathrm{macro}}(\mathbf{r}) + \partial_{\mathrm{ZO}} V_{\mathrm{micro}}(\mathbf{r})\right)$$

$$\mathcal{G}^{\mathrm{ZO}}_{1s,1s} \approx \mathcal{G}^{\mathrm{ZO,micro}}_{1s,1s} + \int \mathrm{d}^3\mathbf{r}\ \left[n_c^{1s}(\mathbf{r}) - n_v^{1s}(\mathbf{r})\right] \partial_{\mathrm{ZO}} V_{\mathrm{macro}}(\mathbf{r})$$

Due to the ZO phonon mode being approximately anti-symmetric with respect to the horizontal mirror plane of $h$BN (i.e., it changes sign about the $h$BN plane), we can express the macroscopic field as $\partial_{\mathrm{ZO}} V_{\mathrm{macro}}(\mathbf{r}) \approx E_0\, \mathrm{sgn}(z - z_{hBN})$ (see Fig. 2a of the main text), where $z_{hBN}$ is the out-of-plane coordinate of the $h$BN layer, and sgn is the signum function.

$$\mathcal{G}^{\mathrm{ZO}}_{1s,1s} \approx \mathcal{G}^{\mathrm{ZO,micro}}_{1s,1s} - \int_{-\infty}^{z_{\mathrm{hBN}}} \mathrm{d}^3\mathbf{r}\ \left[n_c^{1s}(\mathbf{r}) - n_v^{1s}(\mathbf{r})\right] E_0 + \int_{z_{\mathrm{hBN}}}^{\infty} \mathrm{d}^3\mathbf{r}\ \left[n_c^{1s}(\mathbf{r}) - n_v^{1s}(\mathbf{r})\right] E_0$$

$$\mathcal{G}^{\mathrm{ZO}}_{1s,1s} \approx \mathcal{G}^{\mathrm{ZO,micro}}_{1s,1s} + \int_{-\infty}^{\infty} \mathrm{d}^3\mathbf{r}\ \left[n_c^{1s}(\mathbf{r}) - n_v^{1s}(\mathbf{r})\right] E_0 - 2\int_{-\infty}^{z_{\mathrm{hBN}}} \mathrm{d}^3\mathbf{r}\ \left[n_c^{1s}(\mathbf{r}) - n_v^{1s}(\mathbf{r})\right] E_0$$

$$\mathcal{G}^{\mathrm{ZO}}_{1s,1s} \approx \mathcal{G}^{\mathrm{ZO,micro}}_{1s,1s} - 2\int_{-\infty}^{z_{\mathrm{hBN}}} \mathrm{d}^3\mathbf{r}\ \left[n_c^{1s}(\mathbf{r}) - n_v^{1s}(\mathbf{r})\right] E_0$$

which implies that the macroscopic component only arises from the macroscopic field interacting with the interfacial hybridization density. We would like to highlight that this holds even for an encapsulated heterostructure.

### 5.3.4 Resonant Raman spectra of other possible heterostructures

In this section, we show the resonant Raman spectra and the averaged electron and hole densities of the $1s$ exciton for different stacking configurations. To reduce computational costs, we omit the computation of $GW$ corrections to the band structure and instead apply a scissor operator to match the experimental optical gap. Applying a scissor operator instead of the $GW$ corrections induces an asymmetry in peaks I and II; nevertheless, the

only purpose of this section is to show that our conclusions remain valid when choosing different heterostructures. Unless explicitly stated, all calculations use the same convergence parameters as mentioned in the computational details. All Raman intensities are scaled by the same factor; therefore, Raman intensities from different plots are comparable.

**Encapsulated monolayer $WSe_2$**

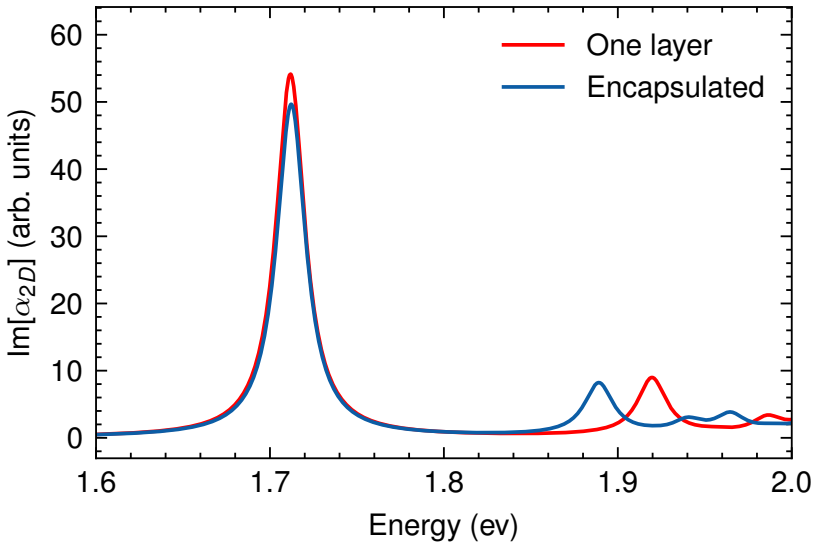


Figure 5.8: Absorption spectra of the single-layer $h$BN heterostructure (red) and the encapsulated heterostructure (blue). The $2s$ exciton energy is red-shifted by an energy of $\sim$ 30 meV when encapsulated with two layer of $h$BN on both sides.

Firstly, we compare the absorption spectrum of the encapsulated heterostructure with that of the single $h$BN heterostructure. Experimentally, the energy difference between the $1s$ and $2s$ excitons is approximately 150 meV for the sandwiched structure, while our calculations indicate that this energy difference is approximately 200 meV for monolayer $WSe_2$ on a single layer of $h$BN. However, as shown in Fig. 2a of Ref. [5], the $1s - 2s$ energy difference for a suspended monolayer of $WSe_2$ (which closely resembles our structure) is approximately 200 meV, while on a substrate the difference is reduced to approximately 160 meV. This confirms that the difference $\sim$ 50 meV between peaks II and III is probably due to insufficient dielectric screening. We further confirm this by computing and comparing

the absorption spectra of the single-layer $h$BN heterostructure with that of the encapsulated heterostructure (with two layers of $h$BN on both sides), as shown in Fig. 5.8.

Next, in Fig. 5.9a, we show the resonant Raman intensities for different out-of-plane modes in monolayer $WSe_2$ encapsulated with two layers of $h$BN on both sides. The $ZO_1$ and $ZO_2$ modes exhibit higher intensities than the others, as both microscopic and macroscopic fields interact with the higher hole density near the closest $h$BN layers, as shown in the inset of Fig. 5.9c. We note that the (small) difference in coupling to the $1s$ exciton between the $ZO_1$ and $ZO_2$ modes arises from the difference in stacking with respect to the $WSe_2$ layer. The $ZO_4$ mode gains Raman intensity through the interaction of its finite macroscopic field (generated by the out-of-phase motion of atoms) with the hybridized density at the nearest layers. In contrast, the macroscopic field generated by the $ZO_3$ mode is antisymmetric with respect to the tungsten layer within the outermost $h$BN layers. This symmetry causes contributions from both sides to nearly cancel out, resulting in vanishing Raman intensity.

**Dependence on twist angle**

In the main text, we present the calculations on a heterostructure with a rotation angle of approximately 100° between the $h$BN and $WSe_2$ layers. In Fig. 5.10, we show the resonant Raman spectrum and the electron and hole densities for the $1s$ exciton of the $WSe_2$ monolayer in heterostructures with different stacking angles. Differences between the spectra as well as between the electron and hole densities are minor. This confirms our assumption in the main text that the physical mechanism of interlayer exciton phonon coupling is rather insensitive to the twist angle of the interface.

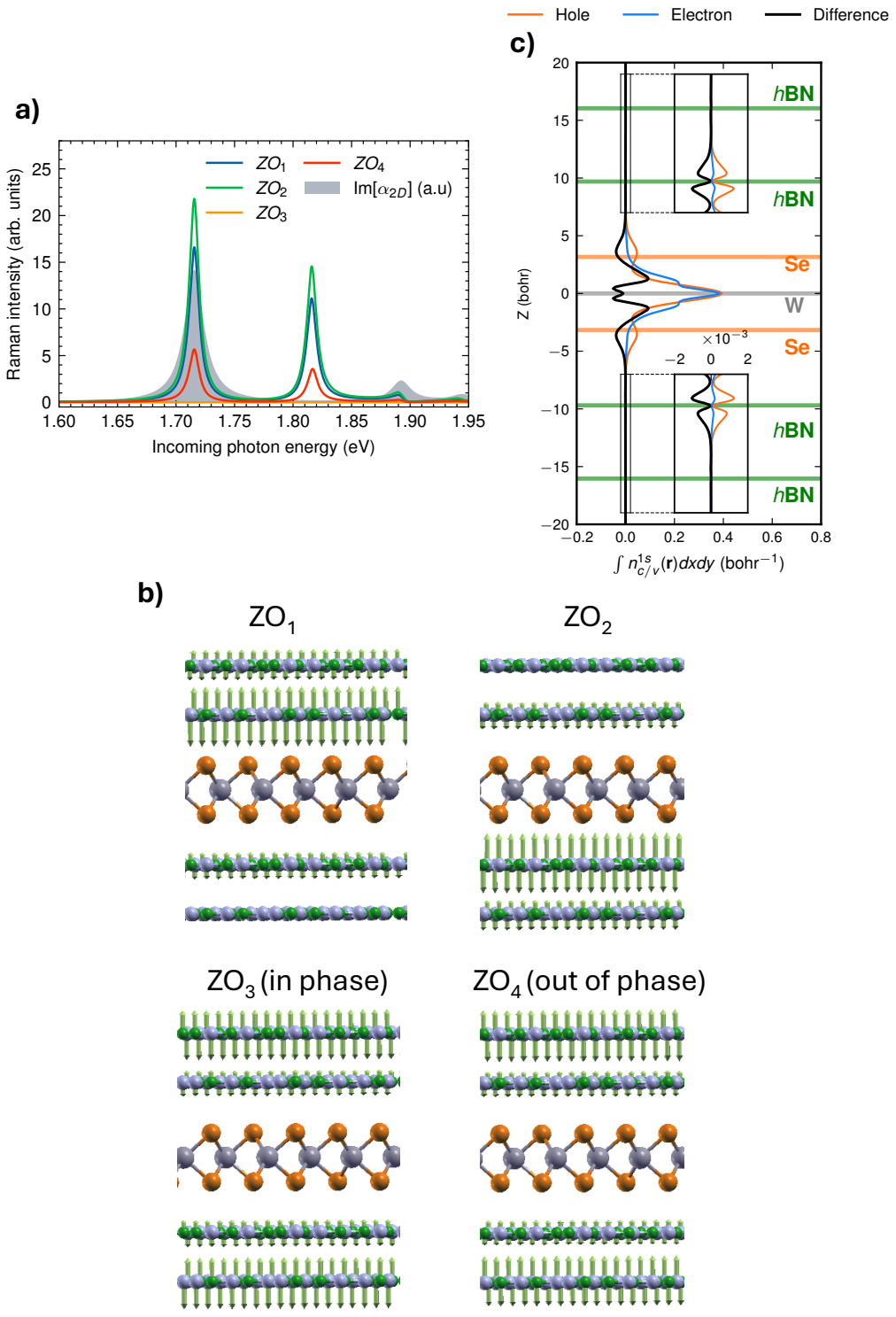


Figure 5.9: a) Resonant Raman intensities as a function of incoming light energy for the ZO modes in encapsulated monolayer $WSe_2$. b) Displacement vectors for different ZO phonon modes. The illustrations were created using Xcrysden [57] software, with a square-root scaling applied to represent the displacement vectors. c) Electron and hole densities of the $1s$ exciton.

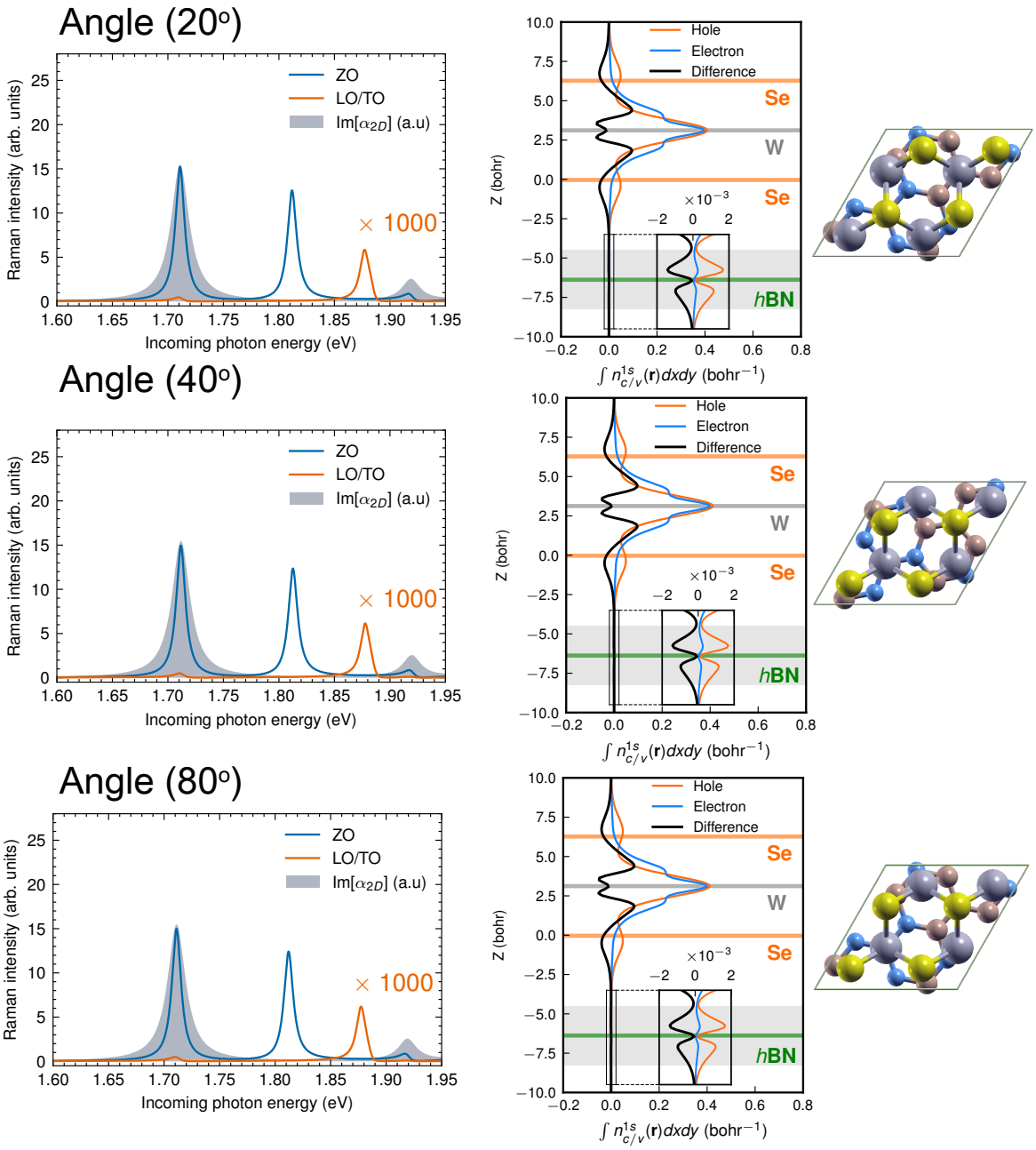


Figure 5.10: (Left) Resonant Raman intensities for the LO/TO and ZO modes of the $h$BN layer as a function of incoming light energy for heterostructures with different stacking angles. (Right) Averaged electron and hole densities of the $1s$ exciton.

**Resonant Raman spectra and averaged electron-hole densities of $1s$ exciton for complex heterostructures**

In Appendix Ref C, we present the resonant Raman spectrum and the averaged electron-hole densities for several heterostructures obtained by laterally shifting the $h$BN layer in the structure shown in Fig. 5.1 (the same structure as used in the main text).

### 5.3.5 Experimental Data

The experimental Raman intensities for the $h$BN ZO mode were obtained by analyzing the raw data recorded for a $h$BN-encapsulated monolayer $WSe_2$ heterostructure, which was provided in the supplementary information of Ref. [70, 69]. While the experimental Raman spectrum features multiple Raman peaks between 750-820 $cm^{-1}$, we take the intensities of the peak near 815 $cm^{-1}$ as the ZO mode intensities.

# Chapter 6

# Conclusions and Outlook

## 6.1 Conclusions

In conclusion, we show how crystal symmetries act on excitonic states and demonstrate that the induced representation is linear, similar to that of phonons. Moreover, we develop a robust *ab-initio* method to compute representations of the excitonic state. Unlike previously existing methods, which require a manual analysis of each state, the method introduced in this thesis to compute excitonic representations can be applied to a wide range of materials, even when they deviate from the conventional Wannier or Frenkel exciton picture.

We then apply our developed formalism to understand the symmetries in exciton-photon and exciton-phonon interactions. In particular, we study the underlying selection rules that govern the coupling of light with excitons and the scattering pathways of excitons by phonons. In order to demonstrate these selection rules, we apply our method to a wide range of materials such as LiF, transition metal dichalcogenides (TMDCs), and $h$BN.

Beyond fundamental insights, our work introduces practical computational advances. While symmetries are widely used in density functional theory (DFT), their role in exciton-phonon calculations has been largely ignored due to phase mismatch issues. We have developed a methodology to systematically restore symmetry considerations in state-of-the-art exciton-phonon calculations, leading to substantial reductions in computational cost while preserving accuracy. These improvements enable efficient calculations of exciton-phonon

coupling in complex systems.

In the final part of this thesis, we theoretically and computationally investigat the coupling of excitons and phonons across layers and its signature in resonant Raman scattering. Using symmetries, we identify the main exciton-phonon scattering channel in the Raman process of a prototypical $WSe_2$@$h$BN heterostructure. We find that the *exciton*-phonon coupling is due to the scattering of the hybridized hole part of the $WSe_2$ exciton with the deformation potential of the $h$BN phonon. This finding sheds light on the nature of the exciton-phonon coupling, which previously was hypothesized to be due to a macroscopic, polar dipole-dipole interaction, but which we actually find to be a near-field effect. We provide the first microscopic explanation for this phenomenon, resolving a long-standing question in the field. This understanding of the interlayer exciton-phonon coupling in two-dimensional heterostructures can be a valuable guide for tailoring inter-layer interactions in such systems.

Finally, I present three newly developed computational tools that have made it possible to perform the calculations presented in this thesis:

- **Lëtzebuerg Electron-Phonon Code (LetzElPhC)**: A software developed to compute electron-phonon matrix elements. LetzElPhC is written in C with multiple levels of parallelization, enabling efficient execution on large-scale high-performance computing (HPC) systems. This code fully exploits all symmetry operations in a crystal, significantly reducing both computational time and storage requirements. Moreover, it computes the representations of electronic states, which are a central ingredient for constructing the excitonic representation matrix. By leveraging symmetry operations, LetzElPhC enables exciton-phonon calculations without symmetry breaking, making it possible to study much larger systems than previously feasible. Additionally, it fixes the longstanding issue with phases when computing exciton-phonon matrix elements using symmetries, a problem that has plagued computations over the last few years.

- **Ydiago**: A library developed for efficient diagonalization of large Bethe-Salpeter equation (BSE) matrices, which is essential for excitonic calculations. Before this work, diagonalizing these matrices in Yambo was a major computational bottleneck. Ydiago

provides an efficient and scalable solution to this problem, allowing the treatment of significantly larger systems and enhancing the overall performance of BSE calculations.

- **PhdScripts**: Set of Python scripts that allow us to compute the irreducible representation labels for the excitonic states, exciton-phonon matrix elements with full crystal symmetries, as well as resonant Raman intensities and phonon-assisted luminescence intensities. Due to the use of symmetries, these scripts enable a more efficient computation of exciton-phonon properties compared to existing implementations.

## 6.2 Outlook

The findings of this thesis offer valuable insight into the symmetry properties of excitons and their implications for optical processes across various material systems. The methodologies developed herein establish a robust framework for understanding selection rules in resonant Raman scattering and phonon-assisted luminescence, which can also be easily extended to other processes. Moreover, the computational tools developed to compute resonant Raman scattering, phonon-assisted luminescence, irreducible representations of excitons, and exciton-phonon lifetimes, which exclusively employ symmetries to reduce computational costs, makes it now possible to apply these methods to much larger systems and allows for high-throughput calculations. One could use these methods and tools on a wide range of materials, such as magnetic insulators (e.g., $CrI_3$, $BiFeO_3$) and $h$BN defect systems, thereby deepening our understanding of their optical responses.

A key direction for future research involves the leveraging of the symmetry properties of excitons described in this thesis to reduce computational costs. Currently, the use of symmetry operations in exciton calculations within publicly available many-body codes remains limited. By incorporating the expressions developed here, computations of excitons and exciton-phonon interactions could be significantly accelerated, thereby enhancing existing computational frameworks, particularly for high-throughput exciton calculations. Moreover, an important application of the proposed methodology is to block diagonalize the BSE

Hamiltonian, where each block corresponds to an irreducible representation. In order to block digonalize, we need to construct the symmetry adapted basis which can be done using projection operators. This greatly reduces the time for BSE kernel construction, time for diagonalization of BSE Hamiltonian, local storage, and RAM memory requirements when performing BSE calculations.

Additionally, while this thesis has focused primarily on excitons and their interactions with phonons, the study of magnons in magnetic insulators represents another important direction for future research. Magnons are known to appear in optical spectroscopic measurements, such as in Raman spectra of magnetic materials which are important when studying magnetic properties of materials. Recently, a new method was developed to compute magnons with the BSE formalism [82]. A logical extension of this work would be to understand their symmetries and their coupling with other quasiparticles, such as phonons [59].

Finally, it is important to highlight that although symmetries drastically reduce the computational cost of exciton-phonon calculations, there remains a need for interpolation methods for excitons and exciton-phonon interactions, such as Wannier interpolation [68]. Wannier interpolation of electrons [68], phonons, and electron-phonon matrix elements [39] has significantly reduced the computational time required to compute properties such as carrier mobilities [61]. Similarly to the electron-phonon case, fine $\mathbf{Q}$-point grids are required to compute exciton-phonon lifetimes and phonon-assisted luminescence or absorption spectra accurately, because of their high sensitivity to the location of the exciton minima. A promising direction for future work is to utilize the recently developed Wannier functions for excitons [45] and extend them to interpolate exciton-phonon matrix elements. This would enable for more efficient and converged exciton-phonon calculations, making large-scale simulations feasible.

# Appendix A

# Lëtzebuerg Electron-Phonon Code (LetzElPhC)

This appendix is taken from the documentation of the LetzElPhC code [78] that was written by me.

## A.1 About the Code

LetzElPhC is a C code designed to compute electron-phonon coupling matrix elements from the outputs of standard Density Functional Theory (DFT) and Density Functional Perturbation Theory (DFPT) calculations. Currently, it only supports the Quantum Espresso code, but we have long plans to support the Abinit code as well. The main objective of this coding project is to facilitate electron-phonon related calculations within the YAMBO code (version 5.2 and above), and it works only with norm-conserving pseudo-potentials. The code is released under the MIT license and hosted on GitHub [link].

### A.1.1 Main Features

- Utilizes full crystal symmetries, ensuring compatibility with the YAMBO code, without encountering phase issues.

- Implements multiple levels of parallelization, including OpenMP, plane-wave, k-point, and q-point parallelization.
- Utilizes fully parallel IO via parallel NetCDF-4/HDF5 libraries.
- Highly portable. The code can be compiled on various CPU architectures and operating systems with minimal to no changes in the source code.

## A.2 Installing the Code

### A.2.1 Mandatory Requirements

- GNU Make
- C99 compiler with complex number support, such as GCC, Clang, ICC, AMD C-Compiler, MinGW (for Windows), PGI, or Arm C compilers.
- MPI implementation supporting at least MPI-standard 2.1 standard, such as Open-MPI, MPICH and its variants, Intel MPI compiler, or Microsoft MPI (for Windows).
- FFTW-3 or Intel-MKL.
- HDF5 and NETCDF-4 libraries with Parallel IO support (compiled with MPI).
- A BLAS library, such as OpenBLAS, BLIS, Intel-MKL, or Atlas.

### A.2.2 Installation Process

LetzElPhC employs a standard make build system. Sample make files are available in the *sample_config* directory. Copy one to the *src* directory and rename it as *make.inc*. Navigate to the *src* directory and edit *make.inc* according to your requirements. Then, in the same directory, execute the following commands:

```
$ make
#### To compile the code in parallel, use the -j option
$ make -j n
```

```
#### where n is the number of processes.
```

Upon successful compilation, you should find the ***lelphc*** executable located in the *src* directory. If you encounter difficulties in locating the required libraries, go to the YAMBO code installation directory and open the *report* file in the *config* directory, which lists all necessary libraries and include paths.

Below are the list of variables in the *make.inc* file with explanations.

```
CC                  :=  mpicc
#### MPI C compiler mpicc/mpiicc (for intel),
CFLAGS              := -O3
#### -O3 is to activate compiler optimizations
LD_FLAGS            :=
#### use this to pass any flags to linker

#### **** OPENMP BUILD ***
#### If you wish to build the code with openmp support
#### uncomment the below line
# OPENMP_FLAGS      := -DELPH_OMP_PARALLEL_BUILD
#### Aditionally, you need to add openmp compiler flag to
#### CFLAGS and LD_FLAGS.
#### Also uncomment the below two lines
# CFLAGS            += -fopenmp ## use -qopenmp for intel
# LD_FLAGS          += -fopenmp ## use -qopenmp for intel

#### FFTW3 include and libs (see FFT flag in yambo config/report)
FFTW_INC            :=  -I/opt/homebrew/include
FFTW3_LIB           :=  -L/opt/homebrew/lib -lfftw3_threads -lfftw3f -lfftw3f_omp
    -lfftw3_omp -lfftw3
#### Note if using FFTW
#### Yambo uses double precision FFTW regardless of the precision with which
   Yambo is built. In contrast, you need to link single (double) precision FFTW
   for single (double) precision LetzElPhC. please refer to https://www.fftw.org
   /fftw3_doc/Precision.html . Also you refer to https://www.fftw.org/fftw3_doc/
   Multi_002dthreaded-FFTW.html  if compiling with openmp support.

```

```
#### If you want to compile the code in double precession, uncomment the below
#CFLAGS              += -DCOMPILE_ELPH_DOUBLE

#### Blas and lapack libs (see BLAS and LAPACK flag in yambo config/report)
BLAS_LIB            :=  -L/opt/homebrew/opt/openblas/lib -lopenblas
#### you need to add both blas and lapack libs for ex : -lblas -llapack

#### netcdf libs and include
#### (see NETCDF flag in yambo config/report)
NETCDF_INC          :=  -I/Users/murali/softwares/core/include
NETCDF_LIB          :=  -L/Users/murali/softwares/core/lib -lnetcdf

#### hdf5 lib (see HDF5 flag in yambo config/report)
HDF5_LIB            :=  -L/opt/homebrew/lib  -lhdf5

#### incase if you want to add additional include dir and libs
INC_DIRS            :=
LIBS                :=


#### Notes Extra CFLAGS
### add -DCOMPILE_ELPH_DOUBLE if you want to compile the code in double
    precession
### if you are using yambo <= 5.1.2, you need to add "-DYAMBO_LT_5_1" to cflags
### for openmp use -DELPH_OMP_PARALLEL_BUILD in CFLAGS and set -fopenmp in
    LD_FLAGS and CFLAGS
```

## A.3 Running the Code

### A.3.1 Running DFT and DFPT (Step 0)

Before using LetzElPhC, ensure you have obtained the following quantities:

- Kohn-Sham wavefunctions (obtained from a non-self-consistent calculation after obtaining the ground state density of the system).

- Phonon eigenvectors and perturbed Hatree and Exchange potentials due to phonon modes (obtained from a DFPT run after finding the ground state).

With the Quantum Espresso code, follow these steps (an example is provided in **examples/qe/silicon**):

- Perform a self-consistent field (SCF) calculation to obtain the ground state.
- Perform a DFPT calculation using the **ph.x** executable to obtain dynamical matrices and changes in potentials on a uniform q-point grid.
- Perform a non-self-consistent field (NSCF) calculation to obtain the wavefunctions on a uniform k-point grid. The k-grid and q-grid of phonons must be commensurate.

**Note**: Set the *dvscf* flag in the **ph.x** input to save the change in potentials. If you forget to set this varaible, you have to rerun the entire calculation. Additionally, make sure that the q-grid is commensurate with the k-grid used in the NSCF calculation (Although, the choice of kgrid to converge the SCF calculation is irrelevant). Once these steps are completed successfully, go to the NSCF folder and enter the *prefix.save* directory, where the wavefunctions are stored. Then, execute *p2y* followed by *yambo* to generate the **SAVE** folder:

```
$ p2y
#### Generates the YAMBO SAVE directory
$ yambo
#### Further processing creates additional files
```

Upon successful completion of these steps, we are ready to use LetzElPhC.

### A.3.2 Running the Preprocessor (Step 1)

Once the **SAVE** directory is obtained, we need to create the **ph_save** folder. Navigate to the phonon calculation directory and run the preprocessor with the *-pp* flag:

```
$ cd /path/to/phonon calculation directory
#### Run the preprocessor
$ lelphc -pp --code=qe -F PH.X_input_file
```

```
#### Where PH.X_input_file is the input file of ph.x code used for computing
    phonons
```

Upon successful execution, the **ph_save** directory will be created, containing all necessary files. If you wish to change the name of the **ph_save** directory, you can set the following environment variable:

```
$ export ELPH_PH_SAVE_DIR=ph_save_name_you_want
```

**Remarks**:

- The new format XML dynamical matrix files are currently not supported.

### A.3.3 Performing the ELPH Calculation (Final Step)

Once both the **SAVE** and **ph_save** folders are created, the ELPH calculation can be executed. Run the following command with the LetzElPhC input file in any directory where you wish to perform the calculation:

```
$ mpirun -n 4 lelphc -F LetzElPhC_input_file
## Here, we are using 4 MPI processes.
```

A detailed description of the input file is provided below:

```
    nkpool          = 1
    # k point parallelization (number of kpools)

    nqpool          = 1
    # q point parallelization (number of qpools)

    ## note (nkpool*nqpool) must divide total number of cpus.

    ## For example, if you run the code on 12 processess,
    ## and set nkpool = 3 and nqpool = 2
    ## then, we have 2 sets of cpus working subset of qpoints
    ## with each group having 3 sub groups which that work on
    ## subset of kpoints. So in total, we have 6 subgroups, each
    ## having 2 cpus that distribute plane waves
```

```
15
16    ##  {1,2,3,4,5,6,7,8,9,10,11,12} (total cpus)
17    ##   _____________|_________________
18    ##  |    divided in to 2 qpools    |
19    ## (qpool 1) {1,2,3,4,5,6}    (qpool 2) {7,8,9,10,11,12}
20    ## _________|_________    _________|__________
21    ## |         |       |   |       |         |
22    ## kp1      kp2     kp3  kp1     kp2       kp3
23    ## where kp1 are kpools each containg 2
24    ## cpus work on subset of plane waves
25
26    start_bnd       = 1
27    # starting band to consider in elph calculation
28
29    end_bnd         = 40
30    # last band to consider in elph calculation
31
32    save_dir        = SAVE
33    # SAVE dir you created with yambo
34
35    ph_save_dir     = ph_save
36    # ph_save directory that was created with preprocessor
37
38    kernel          = dfpt
39
40    ## 1) dfpt (default):     Uses the total change in the Kohn-Sham potential (
      DFPT screening).
41    ## 2) dfpt_local    :     Excludes the contribution from the non-local part
      of the pseudopotentials (p.p.).
42    ## 3) bare          :     No screening; includes only contributions from the
      local and non-local parts of the pseudopotentials.
43    ## 4) bare_local    :     Includes only the contribution from the local part
      of the pseudopotential.
44
45    convention      = standard
46    # standard/yambo, If standard (default)
```

```
47    # <k+q|dV|k> is computed. if yambo, <k|dV|k-q> is outputed
48
49    ###  ##, !, ; are considered as comments
```

# Appendix B

# Ydiago

In this appendix, we discuss the Ydiago library code that was written during my Ph.D. to allow efficient diagonalization in the YAMBO code. This text is taken directly from a section that I have contributed to Ref. [72]

We present a specialized algorithm for diagonalizing the BSE Hamiltonian without TDA, which is given as

$$\begin{pmatrix} R & C \\ -C^{\dagger} & -D \end{pmatrix} \begin{pmatrix} X_I \\ Y_I \end{pmatrix} = \omega_I \begin{pmatrix} X_I \\ Y_I \end{pmatrix} \tag{B.1}$$

We are particularly interested when $D = R^*$ and $C = C^T$, as outlined in Ref. [102]. Throughout this section, we assume the conditions $D = R^*$ and $C = C^T$. The first step in solving the BSE Hamiltonian with this specific structure is to construct a real symmetric matrix $M_r$ of the same dimension, which satisfies the following equation:

$$Q^{\dagger} \begin{pmatrix} R & C \\ -C^* & -R^* \end{pmatrix} Q = -iJM_r \tag{B.2}$$

where $J$ is a real skew-symmetric matrix and $Q$ is a unitary matrix, defined as:

$$Q = \frac{1}{\sqrt{2}} \begin{pmatrix} I & -iI \\ I & iI \end{pmatrix}, \quad J = \begin{pmatrix} 0 & I \\ -I & 0 \end{pmatrix}. \tag{B.3}$$

The expression for $M_r$ is:

$$M_r = \begin{pmatrix} \mathrm{Re}(A+B) & \mathrm{Im}(A-B) \\ -\mathrm{Im}(A+B) & \mathrm{Re}(A-B) \end{pmatrix}. \tag{B.4}$$

It has been shown that if $M$ is positive definite in this special case, $M_r$ will also be positive definite [102]. If $M_r$ is positive definite (which is highly probable), we can perform a Cholesky decomposition on the real symmetric matrix $M_r$, i.e.,

$$M_r = LL^T \tag{B.5}$$

where $L$ is a real lower triangular matrix. This transforms the original eigenvalue problem into the following form:

$$-iWL^T \begin{pmatrix} \bar{X}_I \\ \bar{Y}_I \end{pmatrix} = \omega_I L^T \begin{pmatrix} \bar{X}_I \\ \bar{Y}_I \end{pmatrix} \tag{B.6}$$

where $W = L^T J L$ is a real skew-symmetric matrix, and $-iW$ is Hermitian, sharing the same eigenvalues as the original BSE Hamiltonian. From Eq. (B.6), it is evident that the eigenvalues of $W$ differ from those of the BSE matrix by a factor of $-i$. Since the eigenvalues of a skew-symmetric matrix occur in pairs and are purely imaginary, this means that the eigenvalues of the BSE matrix must be real and occur in pairs, i.e., $(-\omega_I, \omega_I)$. Thus, the entire BSE problem in this special case can be interpreted as a real skew-symmetric eigenvalue problem.

The most computationally demanding step in diagonalization is often the tridiagonalization of a symmetric or Hermitian matrix. The algorithm presented here allows for the tridiagonalization of a real matrix instead of a Hermitian one, significantly reducing both floating-point operations and storage requirements. However, not all eigensolver libraries support a real skew-symmetric solver. For example, the ELPA library provides this functionality in newer versions, while the Scalapack library does not. Nonetheless, the tridiagonalization routines for symmetric matrices can be adapted slightly to handle skew-symmetric matrices, as both largely share the same computational operations. Once the tridiagonal form of the skew-symmetric matrix is obtained, multiplying the result by $-i$ enables the use of Hermitian

tridiagonal solvers to compute the eigenvectors of $W$. Solving the tridiagonal eigenvalue problem is typically not the main computational bottleneck, as efficient algorithms like the MRRR method, which scales as $\mathcal{O}(n^2)$ [24], or the divide-and-conquer approach, which scales as $\mathcal{O}(n^3)$ but uses highly optimized General Matrix-Matrix Multiplication (GEMM) operations.

After calculating the eigenvectors, a back-transformation is applied to recover those of the BSE matrix. Due to the specific structure of the $Q$ matrix in Eq. (B.3), explicit GEMM operations with it can be avoided, further optimizing the procedure. Furthermore, the left eigenvectors for positive eigenvalues and the left/right eigenvectors corresponding to their negative partners can be determined without explicit computation [102]. Consequently, we only need to compute the right eigenvectors associated with positive eigenvalues. The left and right eigenvectors of the positive and negative eigenvalues for the BSE matrix are related as follows [102]:

$$\begin{pmatrix} \text{Right eigenvector for } \omega & \text{Left eigenvector for } \omega \\ \begin{pmatrix} X_I \\ Y_I \end{pmatrix} & \begin{pmatrix} X_I \\ -Y_I \end{pmatrix} \\ \text{Right eigenvector for } -\omega & \text{Left eigenvector for } -\omega \\ \begin{pmatrix} Y_I^* \\ X_I^* \end{pmatrix} & \begin{pmatrix} -Y_I^* \\ X_I^* \end{pmatrix} \end{pmatrix} \tag{B.7}$$

where $\omega > 0$.

It is important to emphasize that, in contrast to standard generalized Hermitian eigenvalue solvers, this method reduces floating-point operations for the most computationally expensive steps. Additionally, using a direct standard generalized Hermitian eigenvalue solver on the BSE matrix may destroy the special properties of this matrix and potentially break degeneracies [102], which is undesirable in such calculations. This approach not only improves efficiency but also ensures robustness against such errors.

We now describe the implementation of the previously discussed algorithm within the Yambo code. Before delving into the diagonalization procedure, we first address the chal-

lenges encountered while optimizing the diagonalization routines in Yambo. Despite both the Yambo code and Scalapack being in existence for over two decades, effectively interfacing them posed significant challenges due to Yambo's choice not to adopt the standard block-cyclic data layout for the BSE matrix. While Scalapack provides data redistribution routines, they are primarily designed to convert between different block-cyclic layouts, offering limited flexibility for Yambo's matrix structure.

A primary reason for Yambo not adopting a block-cyclic layout is the high computational cost involved in constructing the BSE matrix. The construction of the BSE matrix generally scales as $\mathcal{O}(n^5)$, which is substantially more computationally intensive than the diagonalization routines. Each matrix element requires performing a Fast Fourier Transform (FFT) convolution followed by a GEMM operation, making data distribution a crucial factor for optimizing performance. Furthermore, in most instances, the FFT data size fits within CPU caches, which limits the parallelization of these operations across a large number of CPUs. Additionally, Yambo must store large wavefunction arrays to compute these matrix elements, leading to significant memory consumption.

To mitigate these challenges, Yambo leverages symmetries to reduce the number of operations. Most computations are performed within the same MPI rank to avoid redundant calculations and minimize memory usage as well as communication overhead due to MPI latency and synchronization. This approach results in significant improvements in computational efficiency, leading to faster execution times and better scalability. However, this comes at the cost of not being able to adopt block-cyclic layouts. Consequently, the first step in enhancing diagonalization in Yambo is optimizing the data distribution routines, which involve transforming a matrix arbitrarily distributed across MPI processes into a standard block-cyclic layout. This transformation allows the use of most standard linear algebra libraries.

In Yambo, the redistribution of data from an arbitrary distribution to a block-cyclic layout occurs in two main stages. First, the matrix elements are locally grouped along with their corresponding global indices according to their destination rank. Then, a single `AlltoAllv` operation is used to transfer the data to their appropriate destinations according to the block-cyclic layout.

Although this redistribution process may seem memory-intensive, the peak memory footprint is relatively small when compared to the memory required for constructing the BSE matrix. Moreover, the redistribution can be executed in multiple batches to further reduce peak memory usage, ensuring scalability even for large-scale calculations.

Once the matrix has been appropriately redistributed, standard functions from linear algebra libraries can be used to perform efficient computations. For the TDA case, where the BSE matrix is Hermitian, standard Hermitian eigensolvers from ELPA or Scalapack are employed. ELPA offers two types of Hermitian solvers, with type-2 being the default in Yambo. Users have the option to modify the solver selection via input parameters. In Scalapack, the `p?heevr` solver is used. Both solvers allow for the computation of the lowest part of the spectrum. Additionally, Scalapack provides functionality for extracting eigenvectors within a specified range of eigenvalues or indices. If eigenvectors for more than 5% of the spectrum are required, direct diagonalization routines are recommended. For smaller fractions of the spectrum, iterative solvers, which will be discussed in the next section, are preferred.

For the special case of the BSE matrix, the algorithm described earlier is implemented. A key difference between ELPA and Scalapack is that ELPA includes a dedicated solver for real skew-symmetric matrices, whereas Scalapack lacks this feature. As a result, when using Scalapack, we rely on its Hermitian solver, which generally results in slower diagonalization compared to ELPA.

With the new implementation of the diagonalization solver, which can be used to obtain either the full or partial eigenspectrum, we address the long-standing bottleneck associated with the diagonalization of BSE matrices in the Yambo code.

# Appendix C

# Resonant Raman spectra and averaged electron-hole densities of the 1s exciton for other possible stackings of the $h$BN@WSe$_2$ heterostructure

In this appendix, we present the resonant Raman spectrum and the averaged electron-hole densities for several heterostructures obtained by laterally shifting the $h$BN layer in the structure shown in Fig. 5.1 (the same structure as used in the main text). These calculations have been performed to demonstrate that the interlayer exciton-phonon coupling mechanism is insensitive to details of the hybridization (which depend on twist angle and translations).

To reduce computational costs for these test calculations, we used a uniform $\Gamma$-centered $k$-grid of $6 \times 6 \times 1$ and disabled spin-orbit coupling during the self-consistency cycle to obtain the ground state density, as well as to compute dynamical matrices and Hartree-exchange deformation potentials. A denser $k$-grid of $18 \times 18 \times 1$ was used for the BSE calculations. Although spin-orbit effects were neglected during the calculation of the static

dielectric function (where 300 bands were used instead of 600), they were explicitly included when constructing the BSE kernel and evaluating the electron-phonon matrix elements. All other parameters are identical to those detailed in the computational methods section. In figure C.1, we show resonant Raman spectra and averaged electron-hole densities for the $1s$ exciton. As seen in the subfigures, the structural details play a negligible role in the resonant Raman spectrum and the hybridization of the hole density. The interlayer distance was kept the same in all cases.

Figure C.1: Resonant Raman spectra (left column) and averaged electron-hole densities of $1s$ exciton(right column) for different heterostructures obtained by laterally shifting the $h$BN layer in the structure shown in Fig. 5.1. The grey shading represents the imaginary part of the 2D polarizability tensor. The coordinates on each sub-figure denote the shift in crystal units, i.e., $(l_1, l_2, l_3)$ corresponds to a shift of $l_1\vec{a} + l_2\vec{b} + l_3\vec{c}$, where $\vec{a}$, $\vec{b}$, and $\vec{c}$ are the lattice vectors of the heterostructure shown in Fig. 5.1.

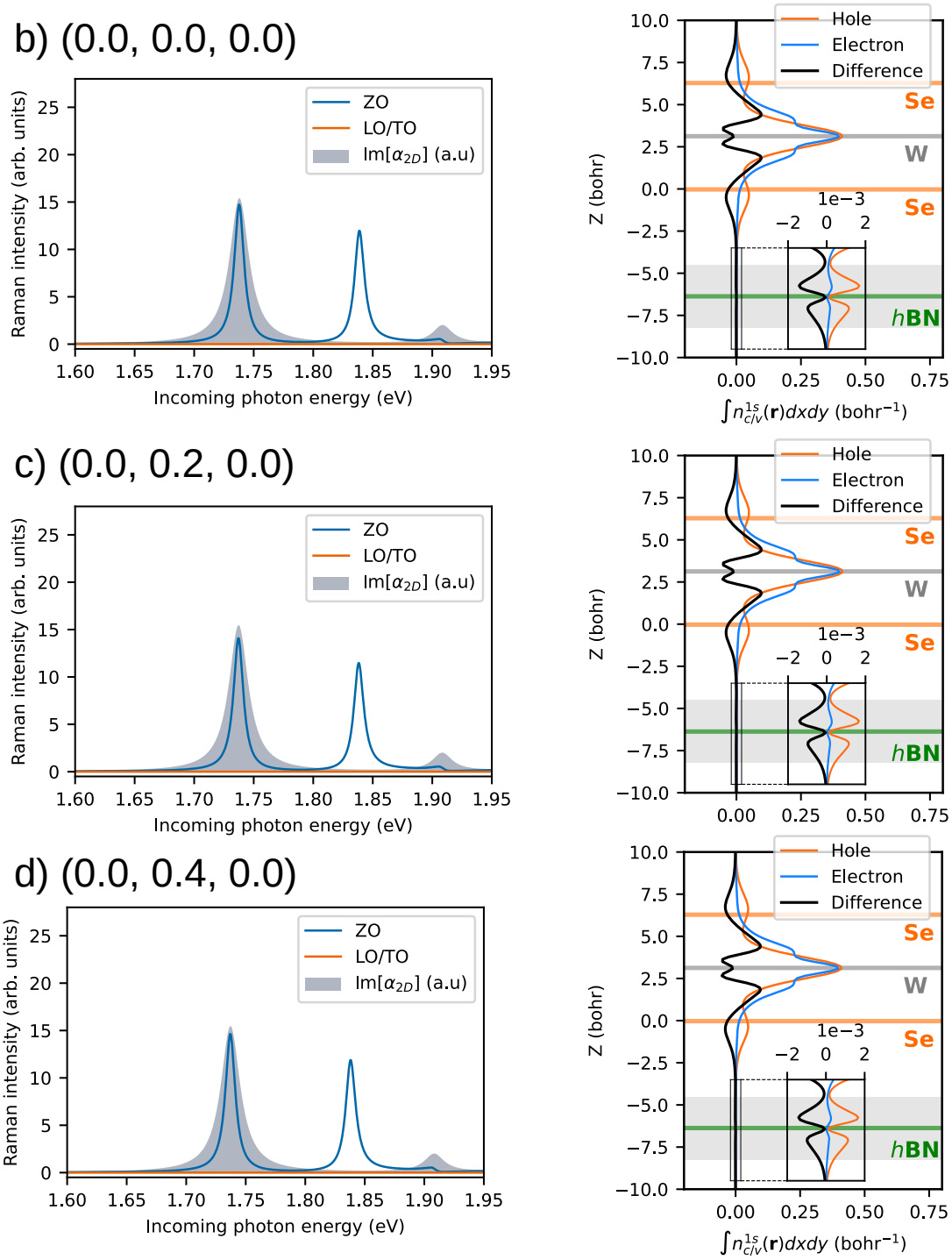
b) (0.0, 0.0, 0.0)
c) (0.0, 0.2, 0.0)
d) (0.0, 0.4, 0.0)
ZO
LO/TO
Im[$\alpha_{2D}$] (a.u)
Raman intensity (arb. units)
Incoming photon energy (eV)
Hole
Electron
Difference
Se
W
Se
hBN
1e−3
Z (bohr)
$\int n^{1s}_{c/v}(\mathbf{r})dxdy$ (bohr$^{-1}$)

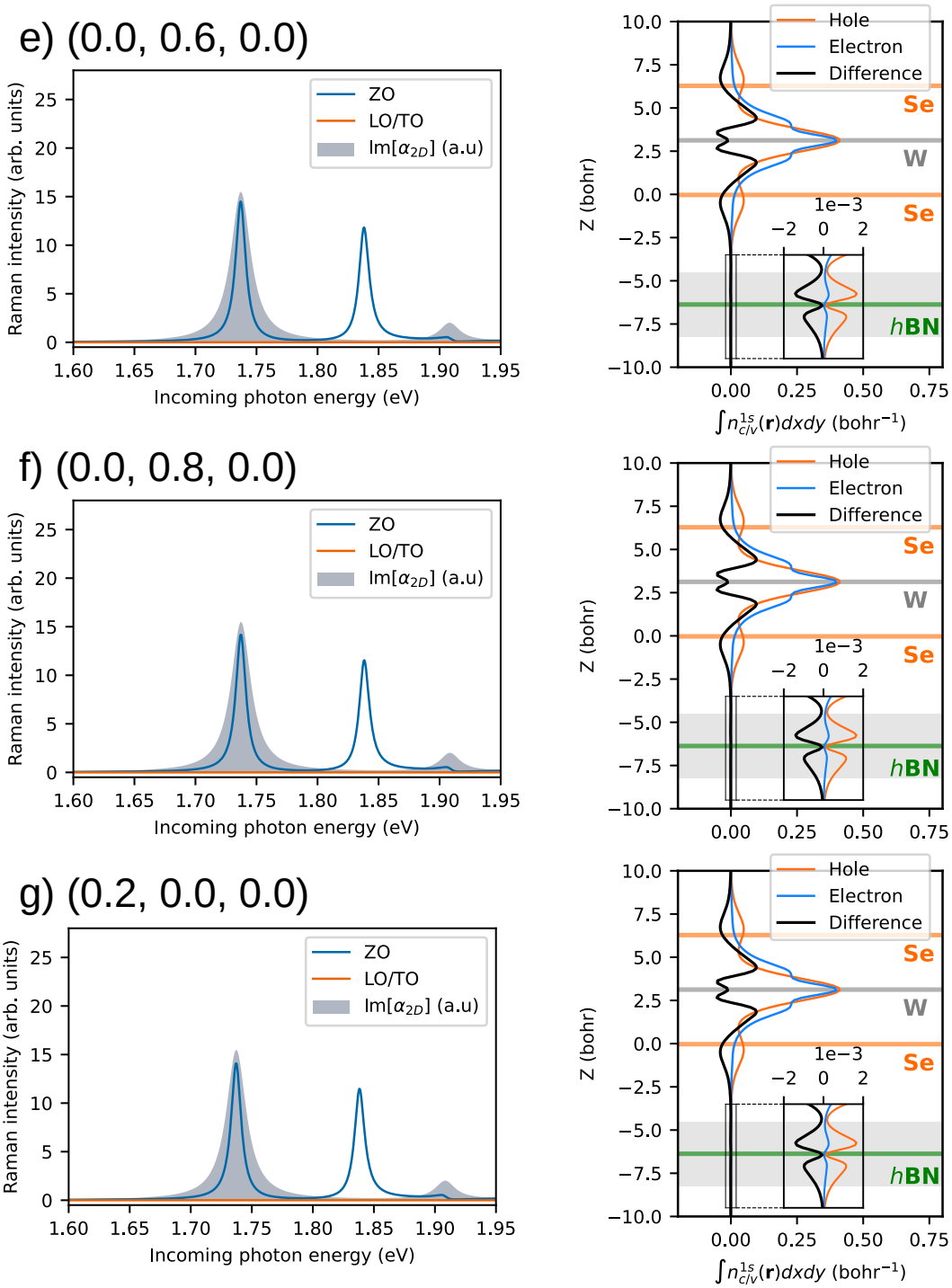
e) (0.0, 0.6, 0.0)
f) (0.0, 0.8, 0.0)
g) (0.2, 0.0, 0.0)
Raman intensity (arb. units)
Incoming photon energy (eV)
ZO
LO/TO
Im[$\alpha_{2D}$] (a.u)
Hole
Electron
Difference
Se
W
Se
hBN
Z (bohr)
1e−3
$\int n^{1s}_{c/v}(\mathbf{r})dxdy$ (bohr$^{-1}$)

h) (0.2, 0.2, 0.0)

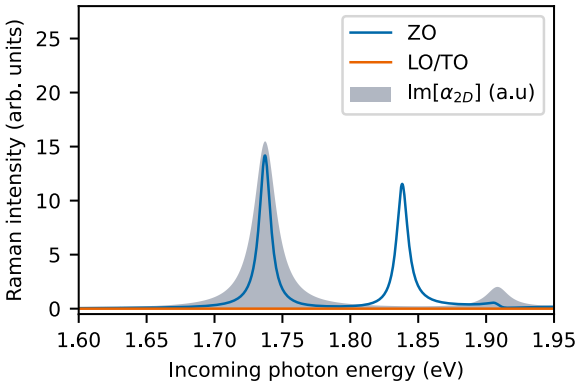


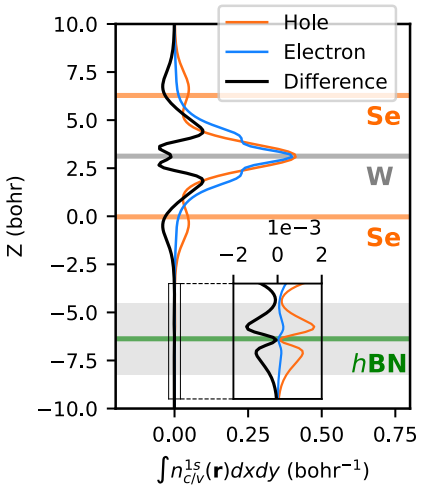


i) (0.2, 0.4, 0.0)

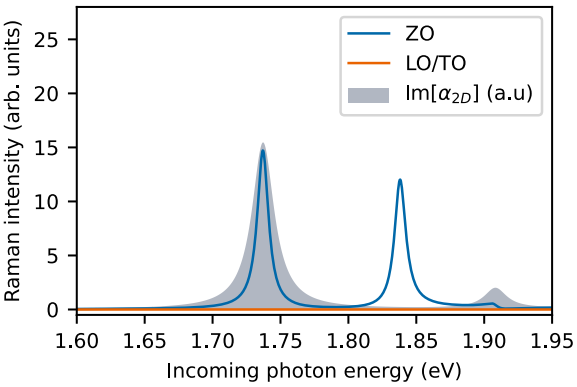


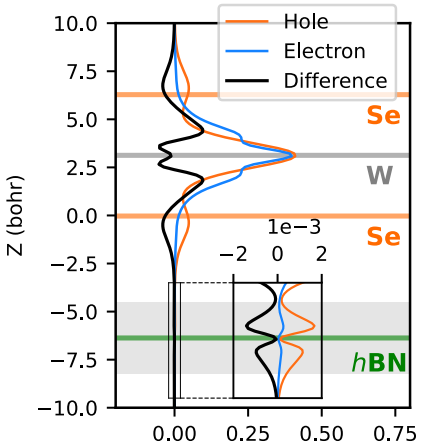


j) (0.2, 0.6, 0.0)

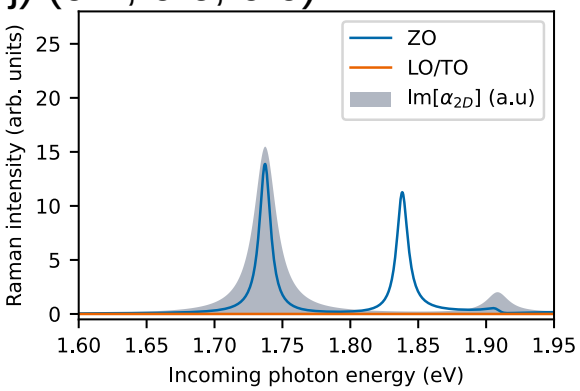


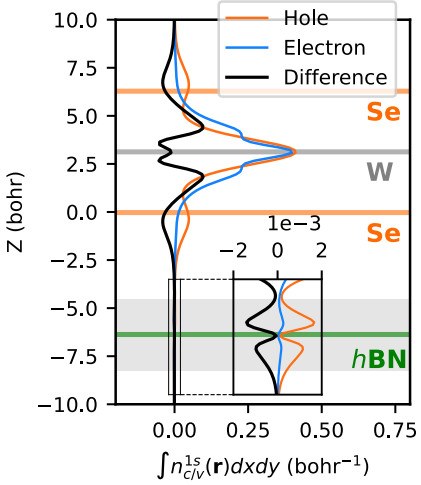

k) (0.2, 0.8, 0.0)

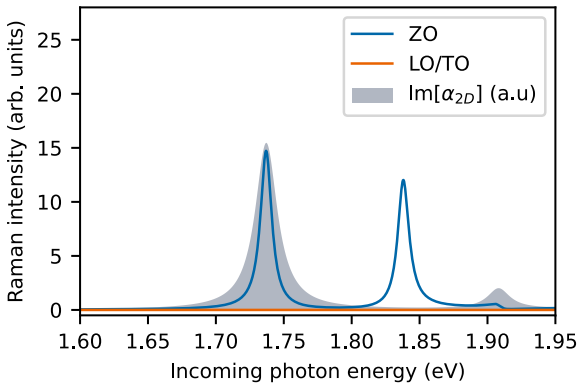


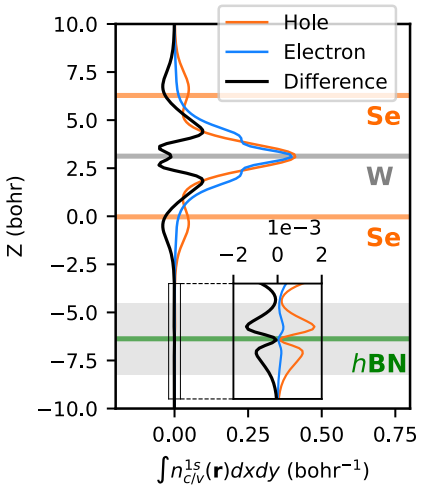


l) (0.4, 0.0, 0.0)

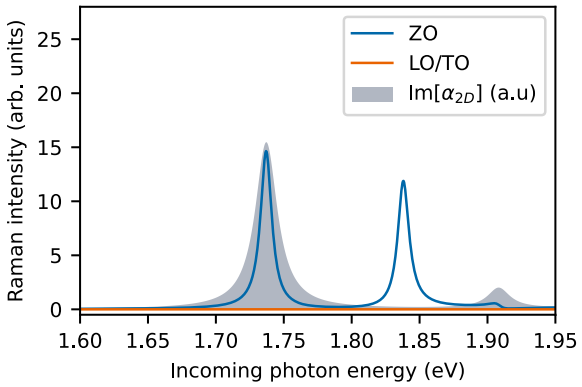


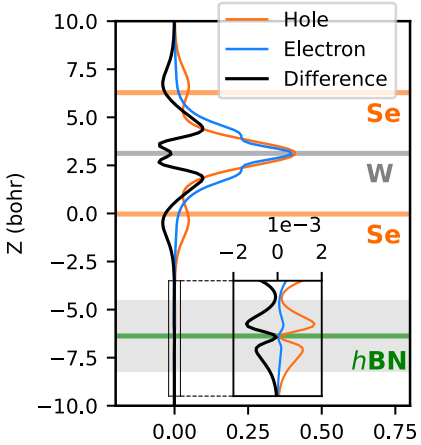


m) (0.4, 0.2, 0.0)

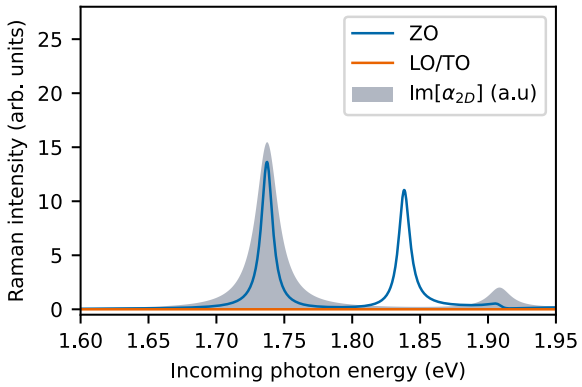


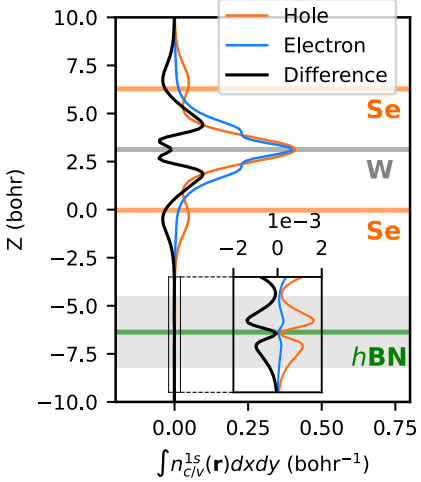

n) (0.4, 0.4, 0.0)

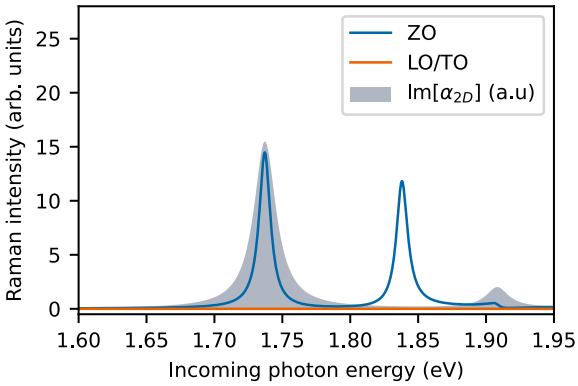


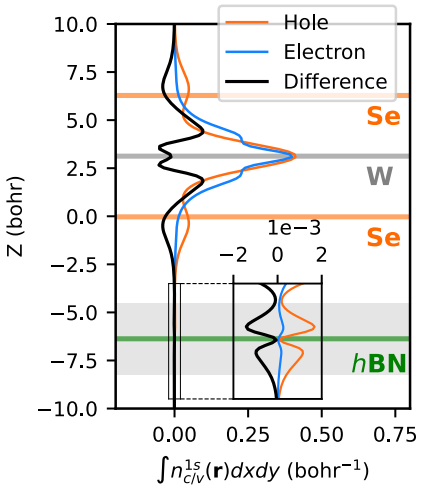


o) (0.4, 0.6, 0.0)

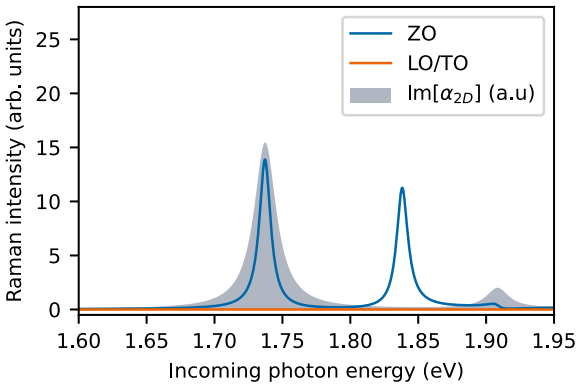


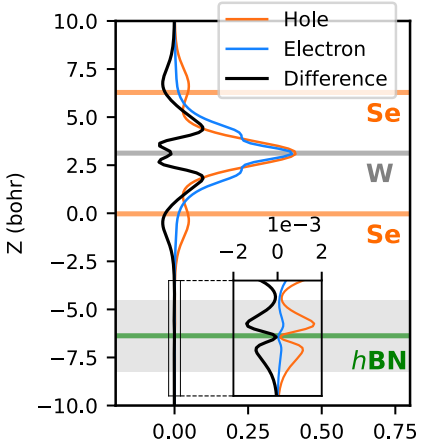


p) (0.4, 0.8, 0.0)

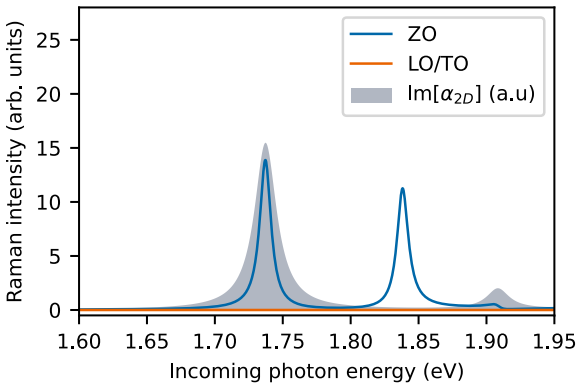


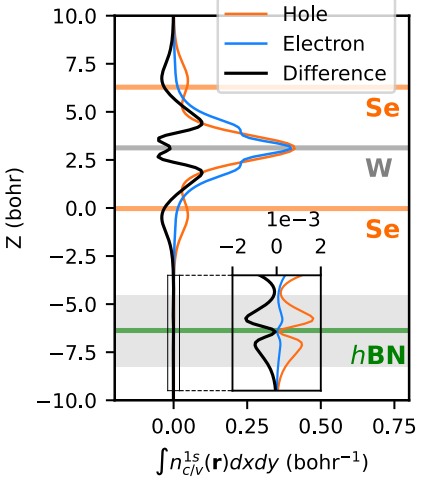

q) (0.6, 0.0, 0.0)

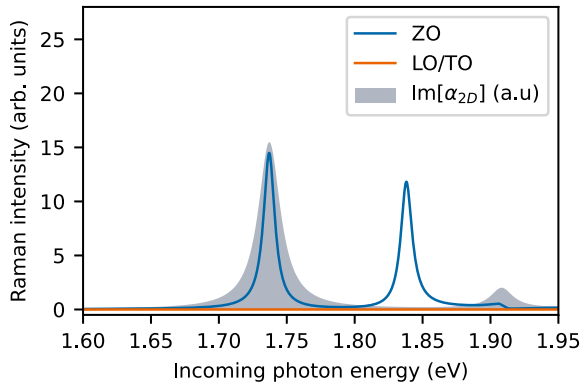


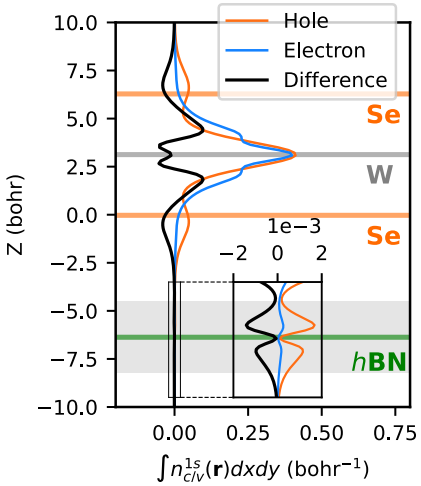


r) (0.6, 0.2, 0.0)

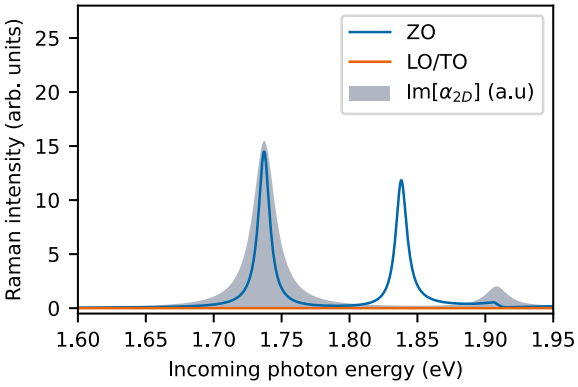


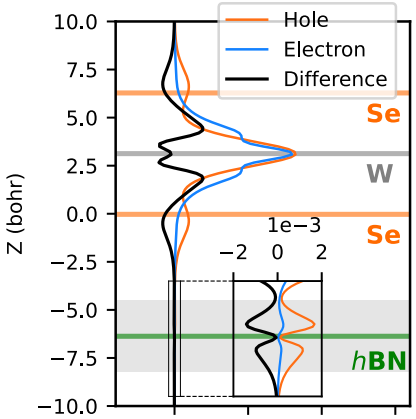


s) (0.6, 0.4, 0.0)

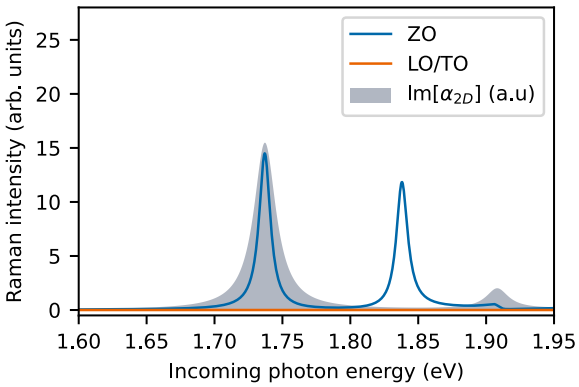


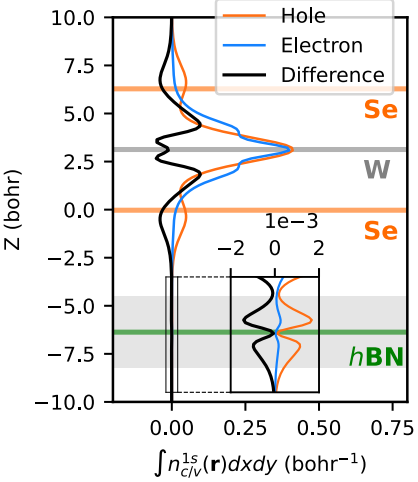

t) (0.6, 0.6, 0.0)

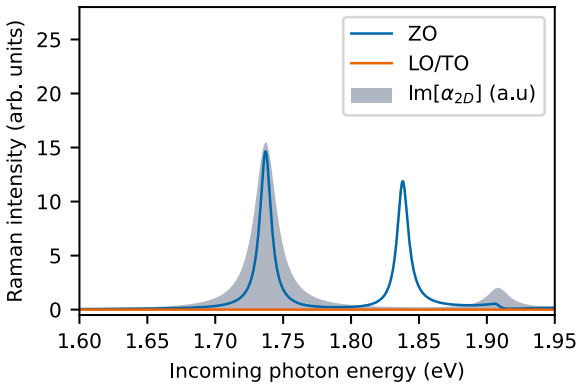


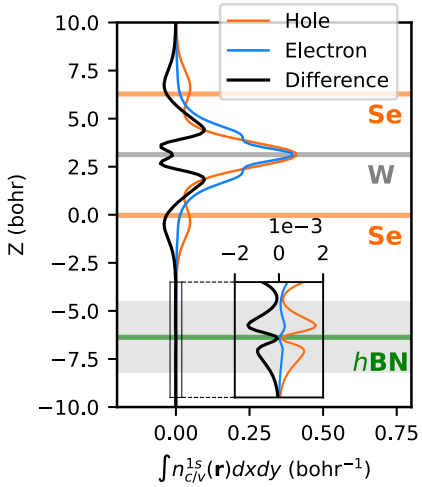


u) (0.6, 0.8, 0.0)

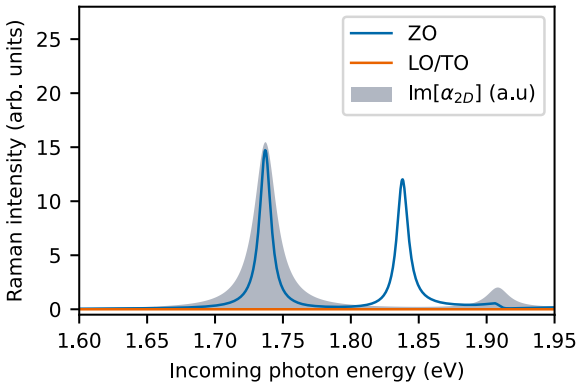


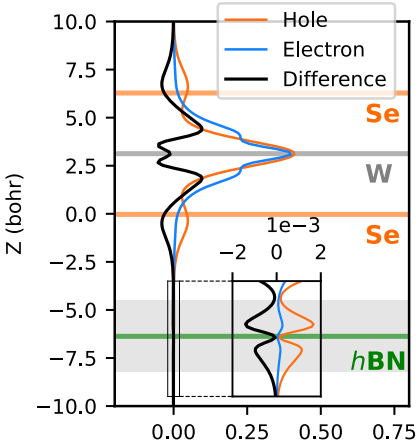


v) (0.8, 0.0, 0.0)

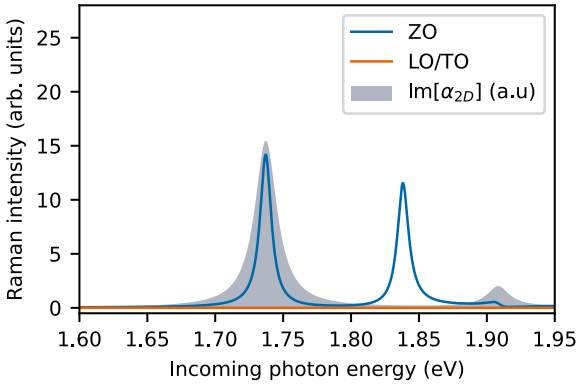


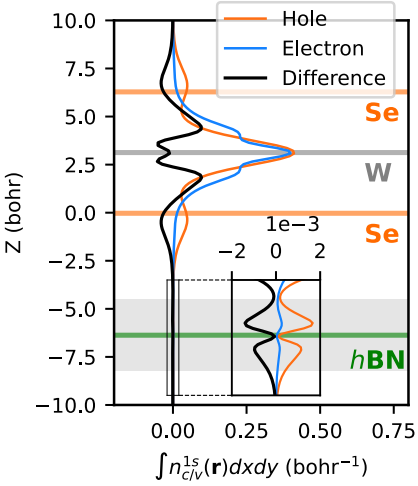

w) (0.8, 0.2, 0.0)

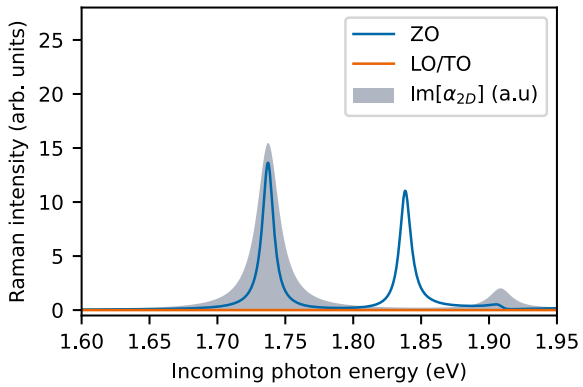


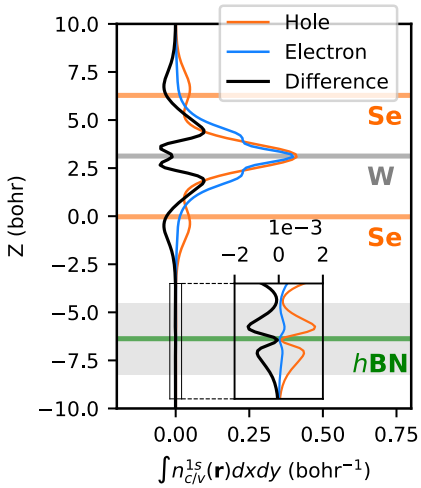


x) (0.8, 0.4, 0.0)

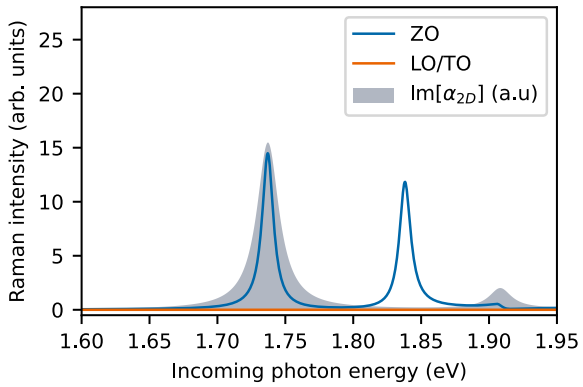


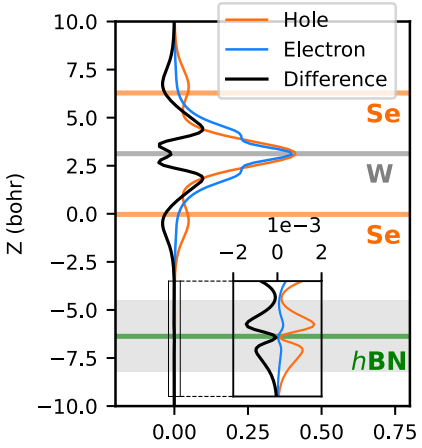


y) (0.8, 0.6, 0.0)

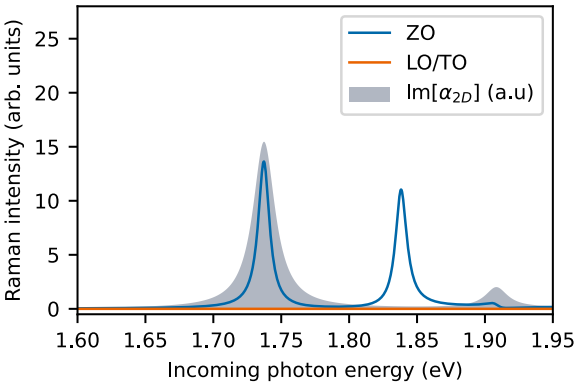


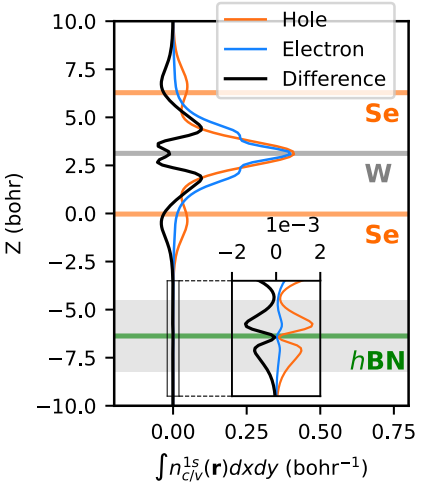

### Density of states

Since it is computationally very expensive to perform BSE calculations for other stackings, we examine the atom-projected density of states (DOS) at the valence band edge for different twist angles. As the hole wave function for the $1s$ state is composed of states near the valence edge, any presence of $h$BN states near the valence edge confirms interfacial hybridization. If the heterostructure contains $n_1 \times n_2 \times 1$ $WSe_2$ unit cells, then we choose the $k$-grid as $\{\lceil \frac{12}{n_1} \rceil \times \lceil \frac{12}{n_2} \rceil \times 1\}$.

In Fig. C.2, we show the total density of states and atom-projected density of states for tungsten and nitrogen atoms near the valence band edge. In all stackings, we observe robust hybridization between nitrogen $p_z$ orbitals and the $d$ orbitals of tungsten atoms. Therefore, we expect that, for all of these stackings, the interlayer exciton-phonon coupling mechanism remains intact.

We would like to emphasize that a relatively coarse grid was used to compute the DOS due to limitations in computational resources. This leads to some quantitative differences in the DOS across different structures. These discrepancies arise from the incomplete inclusion of same-energy states during the summation in the DOS calculation. For example, when $n_1$ and $n_2$ are factors of 12, the same states are included in the summation, resulting in nearly identical DOS for different twist angles, even though the configurations have different numbers of atoms (see plots (c) and (d) in Fig. C.2).

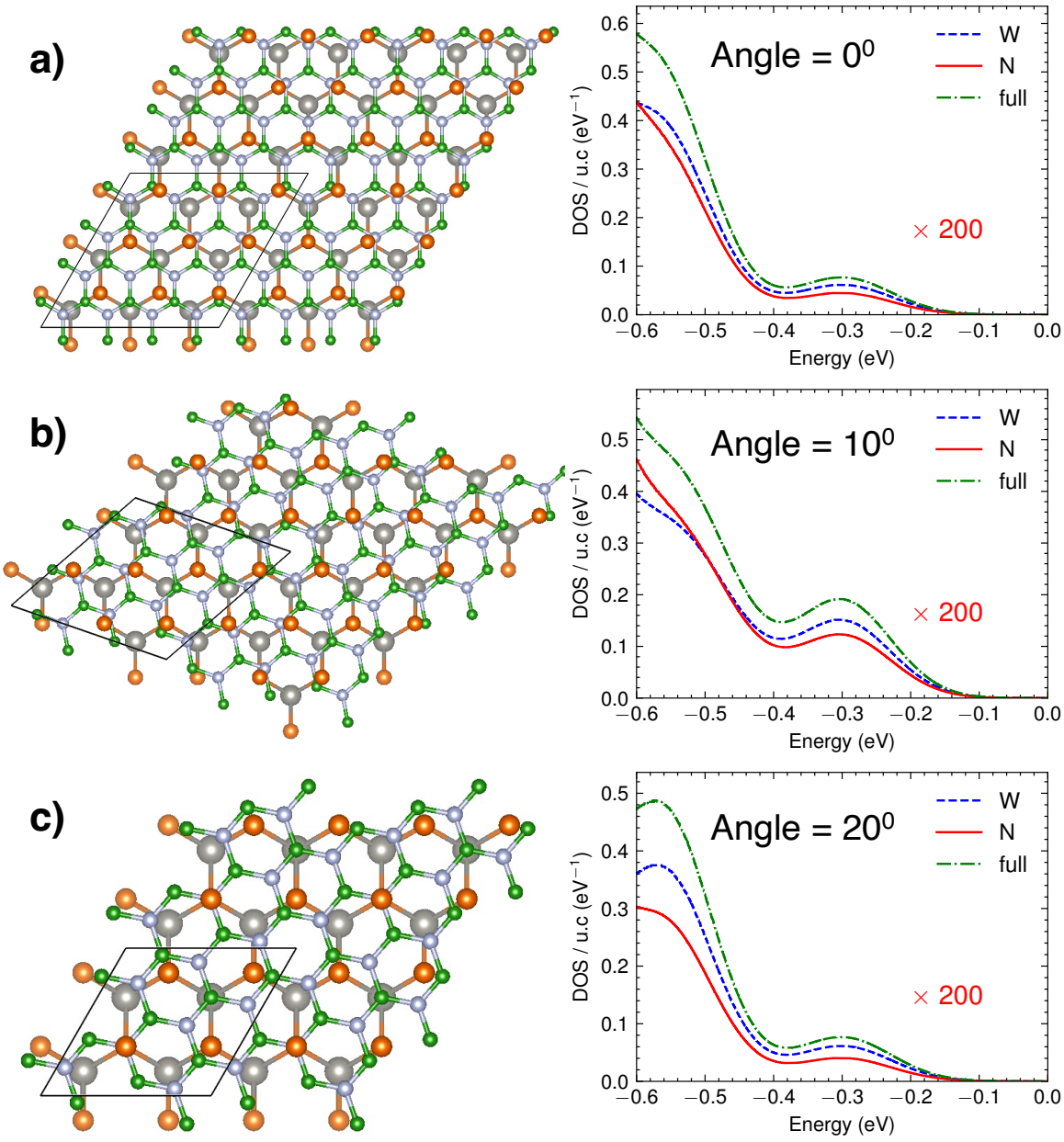
a)
Angle = 0⁰
W
N
full
× 200
DOS / u.c (eV⁻¹)
Energy (eV)
b)
Angle = 10⁰
W
N
full
× 200
DOS / u.c (eV⁻¹)
Energy (eV)
c)
Angle = 20⁰
W
N
full
× 200
DOS / u.c (eV⁻¹)
Energy (eV)

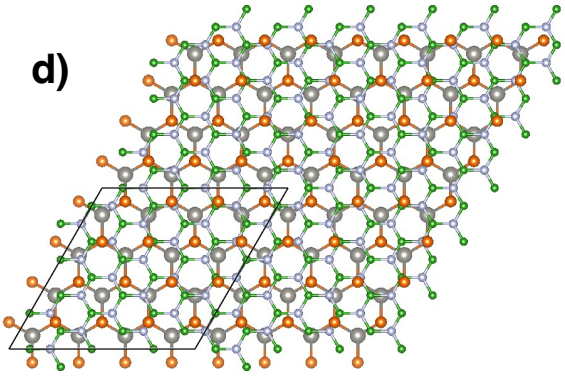
d)

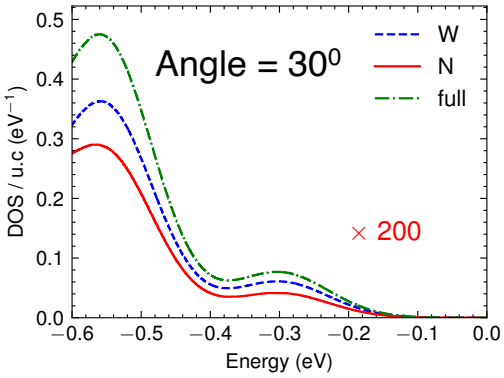
Angle = 30⁰
W
N
full
× 200
DOS / u.c (eV⁻¹)
Energy (eV)

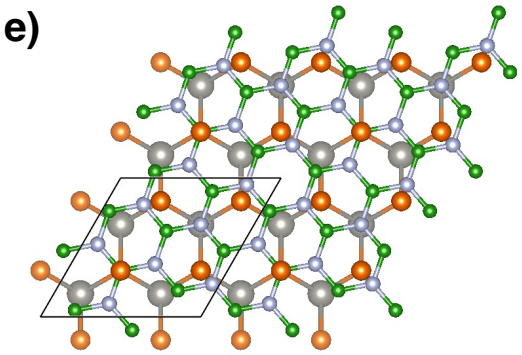
e)

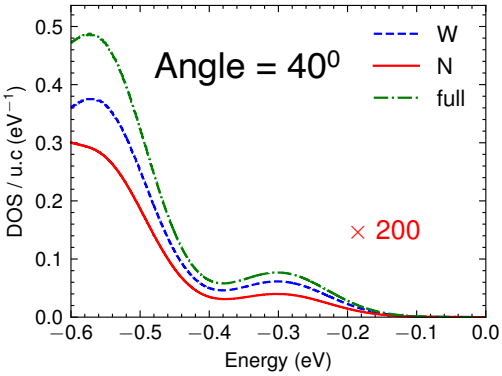
Angle = 40⁰
W
N
full
× 200
DOS / u.c (eV⁻¹)
Energy (eV)

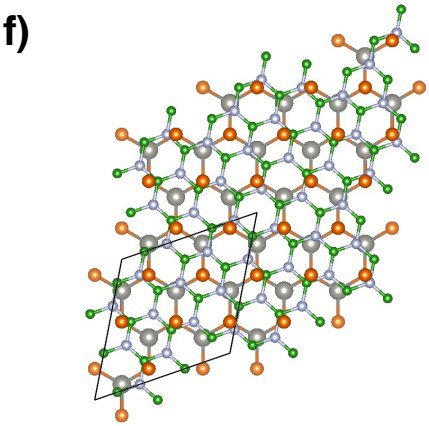
f)

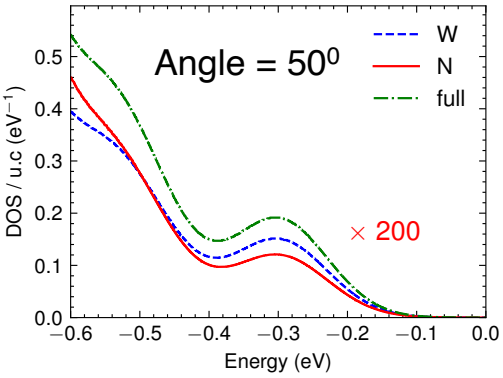
Angle = 50⁰
W
N
full
× 200
DOS / u.c (eV⁻¹)
Energy (eV)

g)

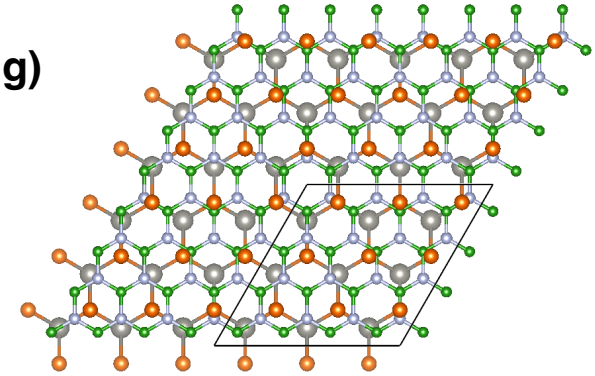

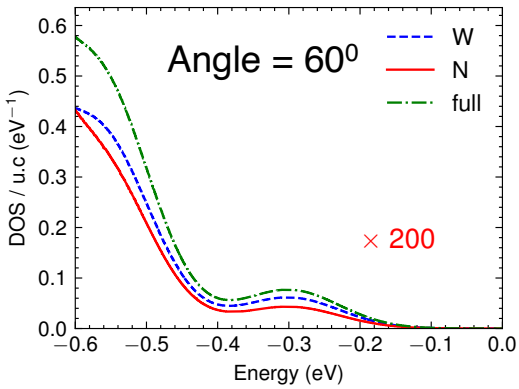
Angle = 60⁰
W
N
full
× 200
DOS / u.c (eV⁻¹)
Energy (eV)

h)

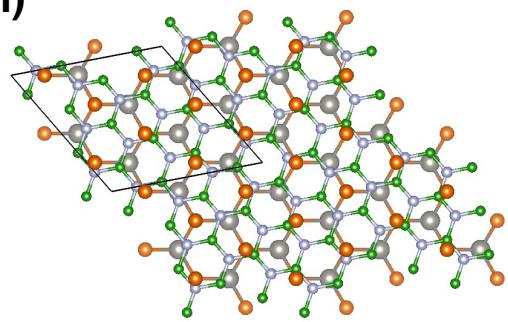

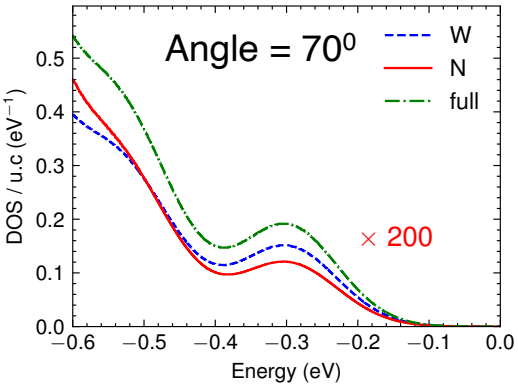
Angle = 70⁰
W
N
full
× 200
DOS / u.c (eV⁻¹)
Energy (eV)

i)

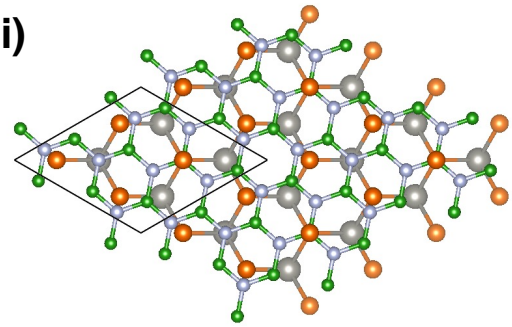

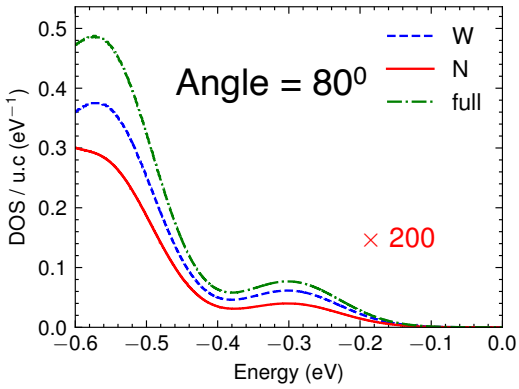
Angle = 80⁰
W
N
full
× 200
DOS / u.c (eV⁻¹)
Energy (eV)

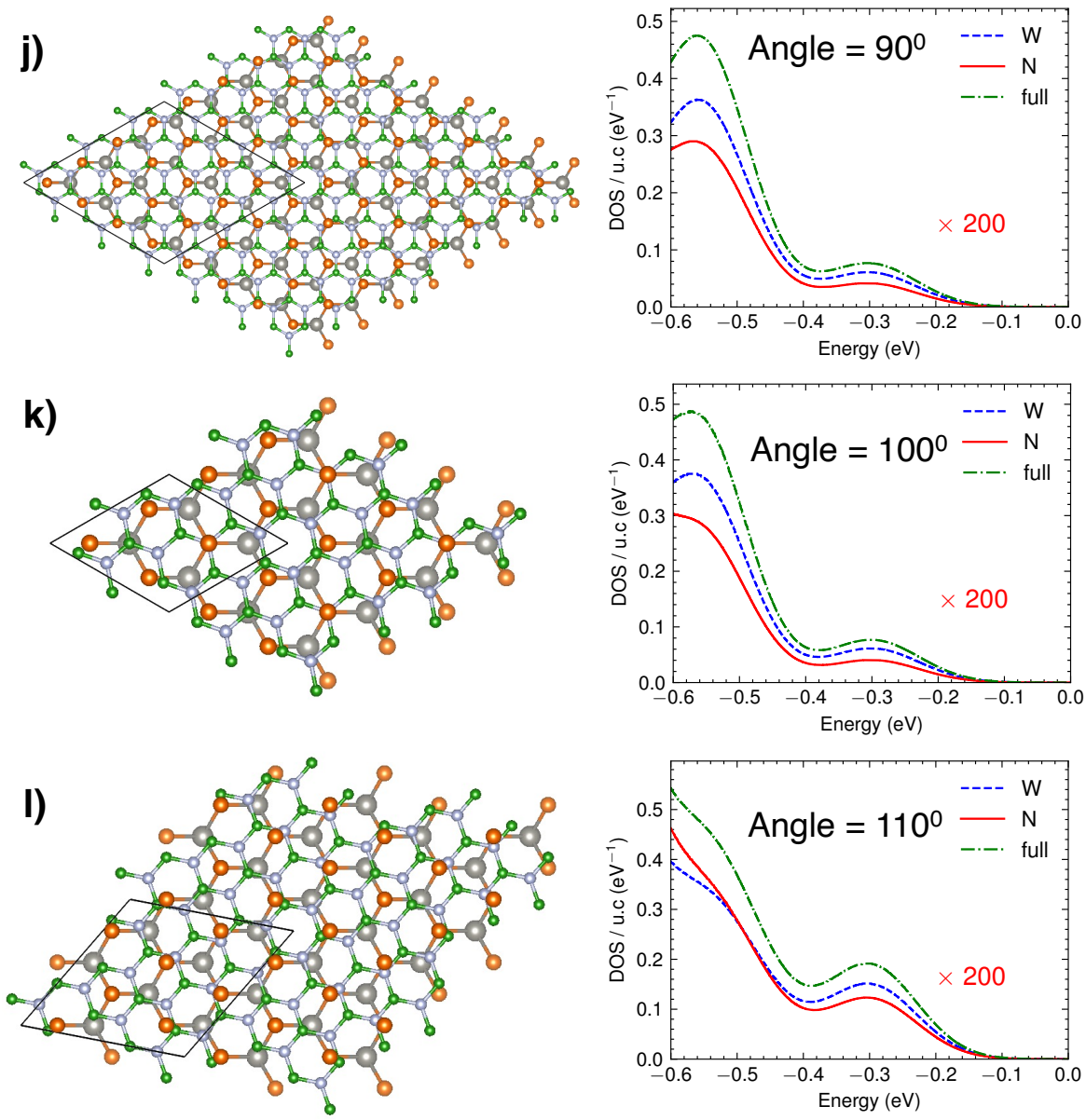


Figure C.2: Total density of states and atom projected density of states near the valance band edge for different stacking angles

# Bibliography


[1] Stefan Albrecht, Lucia Reining, Rodolfo Del Sole, and Giovanni Onida. Ab initio calculation of excitonic effects in the optical spectra of semiconductors. *Phys. Rev. Lett.*, 80:4510–4513, May 1998.

[2] S.L. Altmann. *Rotations, Quaternions, and Double Groups*. Dover Publications, 2005.

[3] Gabriel Antonius and Steven G. Louie. Theory of exciton-phonon coupling. *Phys. Rev. B*, 105:085111, Feb 2022.

[4] N.W. Ashcroft and N.D. Mermin. *Solid State Physics*. Holt, Rinehart and Winston, 1976.

[5] Burak Aslan, Colin Yule, Yifei Yu, Yan Joe Lee, Tony F Heinz, Linyou Cao, and Mark L Brongersma. Excitons in strained and suspended monolayer $WSe_2$. *2D Materials*, 9(1):015002, oct 2021.

[6] Anton Autere, Henri Jussila, Yunyun Dai, Yadong Wang, Harri Lipsanen, and Zhipei Sun. Nonlinear Optics with 2D Layered Materials. *Adv. Mater.*, 30(24):1705963, June 2018.

[7] Lorin X. Benedict, Eric L. Shirley, and Robert B. Bohn. Theory of optical absorption in diamond, si, ge, and gaas. *Phys. Rev. B*, 57:R9385–R9387, Apr 1998.

[8] M. Born and R. Oppenheimer. Zur quantentheorie der molekeln. *Annalen der Physik*, 389(20):457–484, 1927.

[9] Vincent Bouchard. MA PH 464 - Group Theory in Physics: Lecture Notes, 2020.

[10] Fabien Bruneval and Xavier Gonze. Accurate $GW$ self-energies in a plane-wave basis using only a few empty states: Towards large systems. *Phys. Rev. B*, 78:085125, Aug 2008.

[11] Guillaume Brunin, Henrique Pereira Coutada Miranda, Matteo Giantomassi, Miquel Royo, Massimiliano Stengel, Matthieu J. Verstraete, Xavier Gonze, Gian-Marco Rignanese, and Geoffroy Hautier. Electron-phonon beyond fröhlich: Dynamical quadrupoles in polar and covalent solids. *Phys. Rev. Lett.*, 125:136601, Sep 2020.

[12] Ting Cao, Meng Wu, and Steven G. Louie. Unifying optical selection rules for excitons in two dimensions: Band topology and winding numbers. *Phys. Rev. Lett.*, 120:087402, Feb 2018.

[13] Yuan Cao, Valla Fatemi, Shiang Fang, Kenji Watanabe, Takashi Taniguchi, Efthimios Kaxiras, and Pablo Jarillo-Herrero. Unconventional superconductivity in magic-angle graphene superlattices. *Nature*, 556(7699):43–50, Apr 2018.

[14] G. Cassabois, P. Valvin, and B. Gil. Hexagonal boron nitride is an indirect bandgap semiconductor. *Nature Photonics*, 10(4):262–266, Apr 2016.

[15] Yang-hao Chan, Jonah B. Haber, Mit H. Naik, Jeffrey B. Neaton, Diana Y. Qiu, Felipe H. da Jornada, and Steven G. Louie. Exciton lifetime and optical line width profile via exciton–phonon interactions: Theory and first-principles calculations for monolayer $MoS_2$. *Nano Letters*, 23(9):3971–3977, May 2023.

[16] Chen Chen, Xiaolong Chen, Hongyi Yu, Yuchuan Shao, Qiushi Guo, Bingchen Deng, Sungmin Lee, Chao Ma, Kenji Watanabe, Takashi Taniguchi, Je-Geun Park, Shengxi Huang, Wang Yao, and Fengnian Xia. Symmetry-controlled electron–phonon interactions in van der waals heterostructures. *ACS Nano*, 13(1):552–559, Jan 2019.

[17] Hsiao-Yi Chen, Davide Sangalli, and Marco Bernardi. Exciton-phonon interaction and relaxation times from first principles. *Phys. Rev. Lett.*, 125:107401, Aug 2020.

[18] Jian-Hao Chen, Chaun Jang, Shudong Xiao, Masa Ishigami, and Michael S. Fuhrer. Intrinsic and extrinsic performance limits of graphene devices on $SiO_2$. *Nature Nanotechnology*, 3(4):206–209, Apr 2008.

[19] Alexey Chernikov, Timothy C. Berkelbach, Heather M. Hill, Albert Rigosi, Yilei Li, Burak Aslan, David R. Reichman, Mark S. Hybertsen, and Tony F. Heinz. Exciton binding energy and nonhydrogenic rydberg series in monolayer $WS_2$. *Phys. Rev. Lett.*, 113:076802, Aug 2014.

[20] Colin M. Chow, Hongyi Yu, Aaron M. Jones, Jiaqiang Yan, David G. Mandrus, Takashi Taniguchi, Kenji Watanabe, Wang Yao, and Xiaodong Xu. Unusual exciton–phonon interactions at van der waals engineered interfaces. *Nano Letters*, 17(2):1194–1199, Feb 2017.

[21] Carlos Contreras-Ortega, Leonel Vera, and Eduardo Quiroz-Reyes. How great is the great orthogonality theorem? *J. Chem. Educ.*, 68(3):200, March 1991.

[22] S. M. Dancoff. Non-adiabatic meson theory of nuclear forces. *Phys. Rev.*, 78:382–385, May 1950.

[23] Tianqi Deng, Gang Wu, Wen Shi, Zicong Marvin Wong, Jian-Sheng Wang, and Shuo-Wang Yang. Ab initio dipolar electron-phonon interactions in two-dimensional materials. *Phys. Rev. B*, 103:075410, Feb 2021.

[24] Inderjit S. Dhillon, Beresford N. Parlett, and Christof Vömel. The design and implementation of the MRRR algorithm. *ACM Trans. Math. Softw.*, 32(4):533–560, December 2006.

[25] M.S. Dresselhaus, G. Dresselhaus, and A. Jorio. *Group Theory: Application to the Physics of Condensed Matter*. Springer Berlin Heidelberg, 2007.

[26] Luojun Du, Tawfique Hasan, Andres Castellanos-Gomez, Gui-Bin Liu, Yugui Yao, Chun Ning Lau, and Zhipei Sun. Engineering symmetry breaking in 2D layered materials. *Nature Reviews Physics*, 3(3):193–206, Mar 2021.

[27] Luojun Du, Mengzhou Liao, Jian Tang, Qian Zhang, Hua Yu, Rong Yang, Kenji Watanabe, Takashi Taniguchi, Dongxia Shi, Qingming Zhang, and Guangyu Zhang. Strongly enhanced exciton-phonon coupling in two-dimensional $\mathrm{WSe_2}$. *Phys. Rev. B*, 97:235145, Jun 2018.

[28] Luojun Du, Yanchong Zhao, Zhiyan Jia, Mengzhou Liao, Qinqin Wang, Xiangdong Guo, Zhiwen Shi, Rong Yang, Kenji Watanabe, Takashi Taniguchi, Jianyong Xiang, Dongxia Shi, Qing Dai, Zhipei Sun, and Guangyu Zhang. Strong and tunable interlayer coupling of infrared-active phonons to excitons in van der waals heterostructures. *Phys. Rev. B*, 99:205410, May 2019.

[29] M. El-Batanouny and F. Wooten. *Symmetry and Condensed Matter Physics: A Computational Approach*. Cambridge University Press, 2008.

[30] R. J. Elliott. Intensity of optical absorption by excitons. *Phys. Rev.*, 108:1384–1389, Dec 1957.

[31] J. Frenkel. On the transformation of light into heat in solids. i. *Phys. Rev.*, 37:17–44, Jan 1931.

[32] Thomas Galvani, Fulvio Paleari, Henrique P. C. Miranda, Alejandro Molina-Sánchez, Ludger Wirtz, Sylvain Latil, Hakim Amara, and Fran çois Ducastelle. Excitons in boron nitride single layer. *Phys. Rev. B*, 94:125303, Sep 2016.

[33] Matteo Gatti and Francesco Sottile. Exciton dispersion from first principles. *Phys. Rev. B*, 88:155113, Oct 2013.

[34] A. K. Geim and I. V. Grigorieva. Van der waals heterostructures. *Nature*, 499(7459):419–425, Jul 2013.

[35] Iann C. Gerber and Xavier Marie. Dependence of band structure and exciton properties of encapsulated $WSe_2$ monolayers on the hBN-layer thickness. *Phys. Rev. B*, 98:245126, Dec 2018.

[36] Sanjib Ghosh and Timothy C. H. Liew. Quantum computing with exciton-polariton condensates. *npj Quantum Inf.*, 6(16):1–6, February 2020.

[37] P Giannozzi, O Andreussi, T Brumme, O Bunau, M Buongiorno Nardelli, M Calandra, R Car, C Cavazzoni, D Ceresoli, M Cococcioni, N Colonna, I Carnimeo, A Dal Corso, S de Gironcoli, P Delugas, R A DiStasio, A Ferretti, A Floris, G Fratesi, G Fugallo, R Gebauer, U Gerstmann, F Giustino, T Gorni, J Jia, M Kawamura, H-Y Ko, A Kokalj, E Küçükbenli, M Lazzeri, M Marsili, N Marzari, F Mauri, N L Nguyen, H-V Nguyen, A Otero de-la Roza, L Paulatto, S Poncé, D Rocca, R Sabatini, B Santra, M Schlipf, A P Seitsonen, A Smogunov, I Timrov, T Thonhauser, P Umari, N Vast, X Wu, and S Baroni. Advanced capabilities for materials modelling with quantum espresso. *Journal of Physics: Condensed Matter*, 29(46):465901, oct 2017.

[38] Feliciano Giustino. Electron-phonon interactions from first principles. *Rev. Mod. Phys.*, 89:015003, Feb 2017.

[39] Feliciano Giustino, Marvin L. Cohen, and Steven G. Louie. Electron-phonon interaction using wannier functions. *Phys. Rev. B*, 76:165108, Oct 2007.

[40] R. W. Godby and R. J. Needs. Metal-insulator transition in kohn-sham theory and quasiparticle theory. *Phys. Rev. Lett.*, 62:1169–1172, Mar 1989.

[41] K. Gołasa, M. Grzeszczyk, R. Bożek, P. Leszczyński, A. Wysmołek, M. Potemski, and A. Babiński. Resonant raman scattering in $MoS_2$—from bulk to monolayer. *Solid State Communications*, 197:53–56, 2014.

[42] N. O. Gram and M. H. Jørgensen. Influence of quadrupole and octupole electron-phonon coupling on the low-field transport properties of $n$-type silicon. *Phys. Rev. B*, 8:3902–3907, Oct 1973.

[43] David J. Gross. The role of symmetry in fundamental physics. *Proceedings of the National Academy of Sciences*, 93(25):14256–14259, Dec 1996.

[44] Alberto Guandalini, Pino D'Amico, Andrea Ferretti, and Daniele Varsano. Efficient gw calculations in two dimensional materials through a stochastic integration of the screened potential. *npj Computational Materials*, 9(1):44, Mar 2023.

[45] Jonah B. Haber, Diana Y. Qiu, Felipe H. da Jornada, and Jeffrey B. Neaton. Maximally localized exciton wannier functions for solids. *Phys. Rev. B*, 108:125118, Sep 2023.

[46] D. R. Hamann. Optimized norm-conserving vanderbilt pseudopotentials. *Phys. Rev. B*, 88:085117, Aug 2013.

[47] Jiye Han, Keonwoo Park, Shaun Tan, Yana Vaynzof, Jingjing Xue, Eric Wei-Guang Diau, Moungi G. Bawendi, Jin-Wook Lee, and Il Jeon. Perovskite solar cells. *Nat. Rev. Methods Primers*, 5(3):1–27, January 2025.

[48] W. Hanke and L. J. Sham. Many-particle effects in the optical spectrum of a semiconductor. *Phys. Rev. B*, 21:4656–4673, May 1980.

[49] Alex Hayat, Pavel Ginzburg, and Meir Orenstein. Observation of two-photon emission from semiconductors. *Nature Photonics*, 2(4):238–241, Apr 2008.

[50] Keliang He, Nardeep Kumar, Liang Zhao, Zefang Wang, Kin Fai Mak, Hui Zhao, and Jie Shan. Tightly bound excitons in monolayer $WSe_2$. *Phys. Rev. Lett.*, 113:026803, Jul 2014.

[51] Zachariah Hennighausen, Jisoo Moon, Kathleen M. McCreary, Connie H. Li, Olaf M. J. van 't Erve, and Berend T. Jonker. Interlayer exciton–phonon bound state in bi2se3/monolayer $WS_2$ van der waals heterostructures. *ACS Nano*, 17(3):2529–2536, Feb 2023.

[52] P. Hohenberg and W. Kohn. Inhomogeneous electron gas. *Phys. Rev.*, 136:B864–B871, Nov 1964.

[53] Mark S. Hybertsen and Steven G. Louie. Electron correlation in semiconductors and insulators: Band gaps and quasiparticle energies. *Phys. Rev. B*, 34:5390–5413, Oct 1986.

[54] Joanna Jadczak, Joanna Kutrowska-Girzycka, Janina J. Schindler, Joerg Debus, Kenji Watanabe, Takashi Taniguchi, Ching-Hwa Ho, and Leszek Bryja. Investigations of electron-electron and interlayer electron-phonon coupling in van der waals hBN/$WSe_2$/hBN heterostructures by photoluminescence excitation experiments. *Materials*, 14(2), 2021.

[55] Chenhao Jin, Jonghwan Kim, Joonki Suh, Zhiwen Shi, Bin Chen, Xi Fan, Matthew Kam, Kenji Watanabe, Takashi Taniguchi, Sefaattin Tongay, Alex Zettl, Junqiao Wu, and Feng Wang. Interlayer electron–phonon coupling in $WSe_2$/hBN heterostructures. *Nature Physics*, 13(2):127–131, Feb 2017.

[56] W. Kohn and L. J. Sham. Self-consistent equations including exchange and correlation effects. *Phys. Rev.*, 140:A1133–A1138, Nov 1965.

[57] Anton Kokalj. Xcrysden—a new program for displaying crystalline structures and electron densities. *Journal of Molecular Graphics and Modelling*, 17(3):176–179, 1999.

[58] Predrag Lazić. Cellmatch: Combining two unit cells into a common supercell with minimal strain. *Computer Physics Communications*, 197:324–334, 2015.

[59] Khoa B. Le, Ali Esquembre-Kucukalic, Hsiao-Yi Chen, Ivan Maliyov, Jin-Jian Zhou, Davide Sangalli, Alejandro Molina-Sanchez, and Marco Bernardi. Magnon-phonon interactions from first principles. *arXiv*, February 2025.

[60] Pierre Lechifflart, Fulvio Paleari, Davide Sangalli, and Claudio Attaccalite. First-principles study of luminescence in hexagonal boron nitride single layer: Exciton-phonon coupling and the role of substrate. *Phys. Rev. Mater.*, 7:024006, Feb 2023.

[61] Hyungjun Lee, Samuel Poncé, Kyle Bushick, Samad Hajinazar, Jon Lafuente-Bartolome, Joshua Leveillee, Chao Lian, Jae-Mo Lihm, Francesco Macheda, Hitoshi Mori, Hari Paudyal, Weng Hong Sio, Sabyasachi Tiwari, Marios Zacharias, Xiao Zhang, Nicola Bonini, Emmanouil Kioupakis, Elena R. Margine, and Feliciano Giustino. Electron–phonon physics from first principles using the EPW code. *npj Comput. Mater.*, 9(156):1–26, August 2023.

[62] Yifei Li, Xiaowei Zhang, Jinhuan Wang, Xiaoli Ma, Jin-An Shi, Xiangdong Guo, Yonggang Zuo, Ruijie Li, Hao Hong, Ning Li, Kai Xu, Xinyu Huang, Huifeng Tian, Ying Yang, Zhixin Yao, PeiChi Liao, Xiao Li, Junjie Guo, Yuang Huang, Peng Gao, Lifen Wang, Xiaoxia Yang, Qing Dai, EnGe Wang, Kaihui Liu, Wu Zhou, Xiaohui Yu, Liangbo Liang, Ying Jiang, Xin-Zheng Li, and Lei Liu. Engineering interlayer electron–phonon coupling in $WS_2$/BN heterostructures. *Nano Letters*, 22(7):2725–2733, Apr 2022.

[63] S J Magorrian, A J Graham, N Yeung, F Ferreira, P V Nguyen, A Barinov, V I Fal'ko, N R Wilson, and N D M Hine. Band alignment and interlayer hybridisation in transition metal dichalcogenide/hexagonal boron nitride heterostructures. *2D Materials*, 9(4):045036, oct 2022.

[64] A. A. MARADUDIN and S. H. VOSKO. Symmetry properties of the normal vibrations of a crystal. *Rev. Mod. Phys.*, 40:1–37, Jan 1968.

[65] Andrea Marini, Conor Hogan, Myrta Grüning, and Daniele Varsano. Yambo: An ab initio tool for excited state calculations. *Computer Physics Communications*, 180(8):1392–1403, 2009.

[66] Richard M. Martin. *Electronic Structure: Basic Theory and Practical Methods*. Cambridge University Press, Cambridge, England, UK, April 2004.

[67] Richard M. Martin, Lucia Reining, and David M. Ceperley. *Interacting Electrons: Theory and Computational Approaches*. Cambridge University Press, 2016.

[68] Nicola Marzari, Arash A. Mostofi, Jonathan R. Yates, Ivo Souza, and David Vanderbilt. Maximally localized wannier functions: Theory and applications. *Rev. Mod. Phys.*, 84:1419–1475, Oct 2012.

[69] Liam Mcdonnell, Jacob Viner, David Smith, Pasqual Rivera, and Xiaodong Xu. Data to support observation of intravalley phonon scattering of 2s excitons in $MoSe_2$ and $WSe_2$ monolayers, 2020.

[70] Liam P McDonnell, Jacob J S Viner, Pasqual Rivera, Xiaodong Xu, and David C Smith. Observation of intravalley phonon scattering of 2s excitons in $MoSe_2$ and $WSe_2$ monolayers. *2D Materials*, 7(4):045008, jul 2020.

[71] José D. Mella, Muralidhar Nalabothula, Francisco Muñoz, Karin M. Rabe, Ludger Wirtz, Sobhit Singh, and Aldo H. Romero. Prediction of $BiS_2$-type pnictogen dichalcogenide monolayers for optoelectronics. *npj 2D Materials and Applications*, 8(1):4, Jan 2024.

[72] Petru Milev, Blanca Mellado-Pinto, Muralidhar Nalabothula, Ali Esquembre Kucukalic, Fernando Alvarruiz, Enrique Ramos, Ludger Wirtz, Jose E. Roman, and Davide Sangalli. Performances in solving the Bethe-Salpeter equation with the Yambo code. *arXiv*, April 2025.

[73] Henrique P. C. Miranda, Sven Reichardt, Guillaume Froehlicher, Alejandro Molina-Sánchez, Stéphane Berciaud, and Ludger Wirtz. Quantum Interference Effects in Resonant Raman Spectroscopy of Single- and Triple-Layer MoTe2 from First-Principles. *Nano Lett.*, 17(4):2381–2388, April 2017.

[74] Alejandro Molina-Sánchez, Davide Sangalli, Kerstin Hummer, Andrea Marini, and Ludger Wirtz. Effect of spin-orbit interaction on the optical spectra of single-layer, double-layer, and bulk $mos_2$. *Phys. Rev. B*, 88:045412, Jul 2013.

[75] Alejandro Molina-Sánchez, Kerstin Hummer, and Ludger Wirtz. Vibrational and optical properties of $MoS_2$: From monolayer to bulk. *Surface Science Reports*, 70(4):554–586, 2015.

[76] Koichi Momma and Fujio Izumi. Vesta: a three-dimensional visualization system for electronic and structural analysis. *Journal of Applied Crystallography*, 41(3):653–658, 2008.

[77] Shuji Nakamura, Takashi Mukai, and Masayuki Senoh. Candela-class high-brightness ingan/algan double-heterostructure blue-light-emitting diodes. *Applied Physics Letters*, 64(13):1687–1689, 03 1994.

[78] Muralidhar Nalabothula. LetzElPhC, https://github.com/yambo-code/LetzElPhC, 2025.

[79] Muralidhar Nalabothula, Davide Sangalli, Fulvio Paleari, Sven Reichardt, and Ludger Wirtz. Selection rules for exciton-phonon coupling in crystals. *In preparation*, 2025.

[80] Muralidhar Nalabothula, Davide Sangalli, Fulvio Paleari, Sven Reichardt, and Ludger Wirtz. Symmetries of excitons. *In preparation*, 2025.

[81] Muralidhar Nalabothula, Ludger Wirtz, and Sven Reichardt. Origin of Interlayer Exciton–Phonon Coupling in 2D Heterostructures. *Nano Lett.*, 25(15):6160–6167, April 2025.

[82] Thomas Olsen. Unified treatment of magnons and excitons in monolayer $\mathrm{CrI_3}$ from many-body perturbation theory. *Phys. Rev. Lett.*, 127:166402, Oct 2021.

[83] Giovanni Onida, Lucia Reining, and Angel Rubio. Electronic excitations: density-functional versus many-body green's-function approaches. *Rev. Mod. Phys.*, 74:601–659, Jun 2002.

[84] Fulvio Paleari, Thomas Galvani, Hakim Amara, François Ducastelle, Alejandro Molina-Sánchez, and Ludger Wirtz. Excitons in few-layer hexagonal boron nitride: Davydov splitting and surface localization. *2D Materials*, 5(4):045017, aug 2018.

[85] Fulvio Paleari, Henrique P. C. Miranda, Alejandro Molina-Sánchez, and Ludger Wirtz. Exciton-phonon coupling in the ultraviolet absorption and emission spectra of bulk hexagonal boron nitride. *Phys. Rev. Lett.*, 122:187401, May 2019.

[86] John P. Perdew, Kieron Burke, and Matthias Ernzerhof. Generalized gradient approximation made simple. *Phys. Rev. Lett.*, 77:3865–3868, Oct 1996.

[87] John P. Perdew, Kieron Burke, and Matthias Ernzerhof. Generalized gradient approximation made simple. *Phys. Rev. Lett.*, 77:3865–3868, Oct 1996.

[88] John P. Perdew and Mel Levy. Physical content of the exact kohn-sham orbital energies: Band gaps and derivative discontinuities. *Phys. Rev. Lett.*, 51:1884–1887, Nov 1983.

[89] Giovanni Pizzi, Valerio Vitale, Ryotaro Arita, Stefan Blügel, Frank Freimuth, Guillaume Géranton, Marco Gibertini, Dominik Gresch, Charles Johnson, Takashi Koretsune, Julen Ibañez-Azpiroz, Hyungjun Lee, Jae-Mo Lihm, Daniel Marchand, Antimo Marrazzo, Yuriy Mokrousov, Jamal I Mustafa, Yoshiro Nohara, Yusuke Nomura, Lorenzo Paulatto, Samuel Poncé, Thomas Ponweiser, Junfeng Qiao, Florian Thöle, Stepan S Tsirkin, Małgorzata Wierzbowska, Nicola Marzari, David Vanderbilt, Ivo Souza, Arash A Mostofi, and Jonathan R Yates. Wannier90 as a community code: new features and applications. *Journal of Physics: Condensed Matter*, 32(16):165902, jan 2020.

[90] Jack Poulson, Bryan Marker, Robert A. van de Geijn, Jeff R. Hammond, and Nichols A. Romero. Elemental: A new framework for distributed memory dense matrix computations. *ACM Trans. Math. Softw.*, 39(2), feb 2013.

[91] Diana Y. Qiu, Ting Cao, and Steven G. Louie. Nonanalyticity, valley quantum phases, and lightlike exciton dispersion in monolayer transition metal dichalcogenides: Theory and first-principles calculations. *Phys. Rev. Lett.*, 115:176801, Oct 2015.

[92] Emma C. Regan, Danqing Wang, Chenhao Jin, M. Iqbal Bakti Utama, Beini Gao, Xin Wei, Sihan Zhao, Wenyu Zhao, Zuocheng Zhang, Kentaro Yumigeta, Mark Blei, Johan D. Carlström, Kenji Watanabe, Takashi Taniguchi, Sefaattin Tongay, Michael Crommie, Alex Zettl, and Feng Wang. Mott and generalized wigner crystal states in $WSe_2/WS_2$ moiré superlattices. *Nature*, 579(7799):359–363, Mar 2020.

[93] Sven REICHARDT. *Many-Body Perturbation Theory Approach to Raman Spectroscopy and Its Application to 2D Materials*. PhD thesis, RWTH Aachen University, Germany ; ORBilu-University of Luxembourg, 20 April 2018.

[94] Sven Reichardt and Ludger Wirtz. Theory of resonant raman scattering: Towards a comprehensive ab initio description. *Phys. Rev. B*, 99:174312, May 2019.

[95] Sven Reichardt and Ludger Wirtz. Nonadiabatic exciton-phonon coupling in raman spectroscopy of layered materials. *Science Advances*, 6(32):eabb5915, 2020.

[96] Pasqual Rivera, Kyle L. Seyler, Hongyi Yu, John R. Schaibley, Jiaqiang Yan, David G. Mandrus, Wang Yao, and Xiaodong Xu. Valley-polarized exciton dynamics in a 2d semiconductor heterostructure. *Science*, 351(6274):688–691, 2016.

[97] Michael Rohlfing and Steven G. Louie. Electron-hole excitations in semiconductors and insulators. *Phys. Rev. Lett.*, 81:2312–2315, Sep 1998.

[98] Michael Rohlfing and Steven G. Louie. Electron-hole excitations and optical spectra from first principles. *Phys. Rev. B*, 62:4927–4944, Aug 2000.

[99] D Sangalli, A Ferretti, H Miranda, C Attaccalite, I Marri, E Cannuccia, P Melo, M Marsili, F Paleari, A Marrazzo, G Prandini, P Bonfà, M O Atambo, F Affinito, M Palummo, A Molina-Sánchez, C Hogan, M Grüning, D Varsano, and A Marini. Many-body perturbation theory calculations using the YAMBO code. *Journal of Physics: Condensed Matter*, 31(32):325902, may 2019.

[100] Peter Scherpelz, Marco Govoni, Ikutaro Hamada, and Giulia Galli. Implementation and validation of fully relativistic GW calculations: Spin–orbit coupling in molecules, nanocrystals, and solids. *Journal of Chemical Theory and Computation*, 12(8):3523–3544, Aug 2016.

[101] M.D. Schwartz. *Quantum Field Theory and the Standard Model*. Quantum Field Theory and the Standard Model. Cambridge University Press, 2014.

[102] Meiyue Shao, Felipe H. da Jornada, Chao Yang, Jack Deslippe, and Steven G. Louie. Structure preserving parallel algorithms for solving the Bethe–Salpeter eigenvalue problem. *Linear Algebra and its Applications*, 488:148–167, 2016.

[103] Thibault Sohier, Matteo Calandra, and Francesco Mauri. Density functional perturbation theory for gated two-dimensional heterostructures: Theoretical developments and application to flexural phonons in graphene. *Phys. Rev. B*, 96:075448, Aug 2017.

[104] Thibault Sohier, Marco Gibertini, and Matthieu J. Verstraete. Remote free-carrier screening to boost the mobility of Fröhlich-limited two-dimensional semiconductors. *Phys. Rev. Mater.*, 5:024004, Feb 2021.

[105] Gianluca Stefanucci and Robert van Leeuwen. *Nonequilibrium Many-Body Theory of Quantum Systems: A Modern Introduction*. Cambridge University Press, Cambridge, 2013.

[106] Simon Streib. Difference between angular momentum and pseudoangular momentum. *Phys. Rev. B*, 103:L100409, Mar 2021.

[107] Wu-Ki Tung. *Group Theory in Physics: An Introduction to Symmetry Principles, Group Representations, and Special Functions in Classical and Quantum Physics*. World Scientific, 1985.

[108] M.J. van Setten, M. Giantomassi, E. Bousquet, M.J. Verstraete, D.R. Hamann, X. Gonze, and G.-M. Rignanese. The pseudodojo: Training and grading a 85 element optimized norm-conserving pseudopotential table. *Computer Physics Communications*, 226:39–54, 2018.

[109] Carla Verdi and Feliciano Giustino. Fröhlich electron-phonon vertex from first principles. *Phys. Rev. Lett.*, 115:176401, Oct 2015.

[110] Jacob J. S. Viner, Liam P. McDonnell, Pasqual Rivera, Xiaodong Xu, and David C. Smith. Insights into hyperbolic phonon polaritons in $h-\mathrm{BN}$ using raman scattering from encapsulated transition metal dichalcogenide layers. *Phys. Rev. B*, 104:165404, Oct 2021.

[111] T. Q. P. Vuong, G. Cassabois, P. Valvin, S. Liu, J. H. Edgar, and B. Gil. Exciton-phonon interaction in the strong-coupling regime in hexagonal boron nitride. *Phys. Rev. B*, 95:201202, May 2017.

[112] Gang Wang, Alexey Chernikov, Mikhail M. Glazov, Tony F. Heinz, Xavier Marie, Thierry Amand, and Bernhard Urbaszek. Colloquium: Excitons in atomically thin transition metal dichalcogenides. *Rev. Mod. Phys.*, 90(2):021001, Apr 2018.

[113] Gang Wang, Alexey Chernikov, Mikhail M. Glazov, Tony F. Heinz, Xavier Marie, Thierry Amand, and Bernhard Urbaszek. Colloquium: Excitons in atomically thin transition metal dichalcogenides. *Rev. Mod. Phys.*, 90(2):021001, apr 2018.

[114] Qing-Yan Wang, Zhi Li, Wen-Hao Zhang, Zuo-Cheng Zhang, Jin-Song Zhang, Wei Li, Hao Ding, Yun-Bo Ou, Peng Deng, Kai Chang, et al. Interface-induced high-temperature superconductivity in single unit-cell FeSe films on $SrTiO_3$. *Chinese Physics Letters*, 29(3):037402, 2012.

[115] Tingting Wang, Hong Sun, Xiaozhe Li, and Lifa Zhang. Chiral Phonons: Prediction, Verification, and Application. *Nano Lett.*, 24(15):4311–4318, April 2024.

[116] Gregory H. Wannier. The structure of electronic excitation levels in insulating crystals. *Phys. Rev.*, 52:191–197, Aug 1937.

[117] Kenji Watanabe, Takashi Taniguchi, and Hisao Kanda. Direct-bandgap properties and evidence for ultraviolet lasing of hexagonal boron nitride single crystal. *Nature Materials*, 3(6):404–409, Jun 2004.

[118] Steven Weinberg. *The Quantum Theory of Fields, Volume 1: Foundations*. Cambridge University Press, 2005.

[119] Steven Weinberg. *Lectures on Quantum Mechanics*. Cambridge University Press, Cambridge, England, UK, September 2015.

[120] E. P. Wigner. *Group Theory and Its Application to the Quantum Mechanics of Atomic Spectra*. Academic Press, New York, 1959.

[121] E. P. Wigner and U. Fano. Group theory and its application to the quantum mechanics of atomic spectra. *American Journal of Physics*, 28(4):408–409, 04 1960.

[122] Ludger Wirtz, Andrea Marini, Myrta Grüning, Claudio Attaccalite, Georg Kresse, and Angel Rubio. Comment on “huge excitonic effects in layered hexagonal boron nitride”. *Phys. Rev. Lett.*, 100:189701, May 2008.

[123] Ludger Wirtz, Andrea Marini, and Angel Rubio. Excitons in boron nitride nanotubes: Dimensionality effects. *Phys. Rev. Lett.*, 96:126104, Mar 2006.

[124] Matteo Zanfrognini, Alexandre Plaud, Ingrid Stenger, Frédéric Fossard, Lorenzo Sponza, Léonard Schué, Fulvio Paleari, Elisa Molinari, Daniele Varsano, Ludger Wirtz, Fran çois Ducastelle, Annick Loiseau, and Julien Barjon. Distinguishing different stackings in layered materials via luminescence spectroscopy. *Phys. Rev. Lett.*, 131:206902, Nov 2023.

[125] Lifa Zhang and Qian Niu. Chiral phonons at high-symmetry points in monolayer hexagonal lattices. *Phys. Rev. Lett.*, 115:115502, Sep 2015.

[126] Lanqing Zhou, Konstantin Wirth, Minh N. Bui, Renu Rani, Detlev Grützmacher, Thomas Taubner, and Beata E. Kardynał. Resonant raman scattering of surface phonon polaritons mediated by excitons in $WSe_2$ films. *ACS Photonics*, 11(8):3079–3086, Aug 2024.